

DOKUZ EYLÜL UNIVERSITY
GRADUATE SCHOOL OF NATURAL AND APPLIED SCIENCES

**DEVELOPMENT OF NANO-MATERIAL BASED
OPTICAL CHEMICAL SENSORS INDICATING
OXYGEN LEVELS IN PETROCHEMISTRY
RELATED WORKPLACES**

by
Zeynep AY

July, 2015
İZMİR

**DEVELOPMENT OF NANO-MATERIAL BASED
OPTICAL CHEMICAL SENSORS INDICATING
OXYGEN LEVELS IN PETROCHEMISTRY
RELATED WORKPLACES**

**A Thesis Submitted to the
Graduate School of Natural and Applied Sciences of Dokuz Eylül University
In Partial Fulfillment of the Requirements for the Degree of Master of Science
in Nanoscience and Nanoengineering Department.**

**by
Zeynep AY**

**July, 2015
İZMİR**


M.Sc THESIS EXAMINATION RESULT FORM

We have read the thesis entitled “**DEVELOPMENT OF NANO-MATERIAL BASED OPTICAL CHEMICAL SENSORS INDICATING OXYGEN LEVELS IN PETROCHEMISTRY RELATED WORKPLACES**” completed by **ZEYNEP AY** under supervision of **PROF. DR. KADRIYE ERTEKİN** and we certify that in our opinion it is fully adequate, in scope and in quality, as a thesis for the degree of Master of Science.



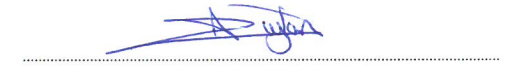
Prof. Dr. Kadriye ERTEKİN

Supervisor



Prof. Dr. Erdal Gelik

(Jury Member)



Asst. Prof. Dr. Aylin Akbayrak

(Jury Member)



Prof. Dr. Ayşe OKUR

Director

Graduate School of Natural and Applied Sciences

ACKNOWLEDGMENTS

First of all, I would like to thank my supervisor Prof. Dr. Kadriye ERTEKİN for giving me the opportunity to carry out this work and for his valuable suggestions, encouragement and supervision.

I also gratefully acknowledge that my personal funding was provided by the Scientific and Technological Research Council of Turkey (TUBITAK) (Research Fellowship Program for National Researchers, 2210-C). My research funding was provided by the Scientific Research Funds of Dokuz Eylül University (project number: 2014.KB.FEN.039).

I would like to thank to my parents and especially to my mother Vesile AY, my father Mevlüt Süreyya AY and my sister Assist. Prof. Dr. Başak AY SAYLAM for their great supports. Without their never-ending support and encouragement I would not be where I find myself today.

Finally, I thank all my friends, specialists and professors at EMUM and faculty of science for all of the invaluable help, friendship and encouragement.

Zeynep AY

**DEVELOPMENT OF NANO-MATERIAL BASED OPTICAL CHEMICAL
SENSORS INDICATING OXYGEN LEVELS IN PETROCHEMISTRY
RELATED WORKPLACES**

ABSTRACT

In workplaces, especially in refineries, volatile petroleum solvents are usually in the form of mixtures of alkanes, cyclic alkanes, alkenes and the aromatics. Such atmospheres which are deficient in oxygen may not provide adequate sensory warning of danger. Therefore correct and continuous monitoring of oxygen levels in such environments is quite important. On the other hand, ruthenium (II) derivatives are known as oxygen sensitive dyes and have intensively been used in the design of optical chemical sensors. Most of the ruthenium dyes suffer from leaching from host matrices due to the water solubilities. In order to provide the best host/dye compatibility we used the amphiphilic ruthenium derivatives in silicon based matrices. In this work, emission-based oxygen sensing properties of highly luminescent ruthenium (II) derivatives were tested in the presence and absence of some volatile organics. Newly synthesized two orange-red emitting alkyl branched ruthenium complexes were used along with silver nanoparticles (AgNPs) in two different silicon based matrices for oxygen sensing purposes. The sensing materials were fabricated in form of thin films and electrospun nanofibers. Ionic liquid and perfluorinated compounds were exploited as additives to enhance the response to oxygen. Oxygen induced spectral changes at 630 nm were followed for both gas phase and dissolved oxygen as the analytical signal. The oxygen sensitivities of the probes were also tested by lifetime based and kinetic mode measurements. Utilization of the amphiphilic Ru dyes in silicon along with AgNPs in the form of electrospun fibers resulted in many advantages such as enhanced long term stability, increased surface area, sensitivity and improvement in all sensor dynamics. Sensing characteristics of the offered design were tested and calibrated in the presence of vapors of benzene, toluene, ethylbenzene, hexane and xylene, which simulate refinery related work places.

Keywords: Oxygen, dissolved oxygen, sensor, nanofiber, silver nanoparticles, volatile organic compounds.

PETROKİMYA SEKTÖRÜNDE İŞYERİ ORTAMINDAKİ OKSİJEN SEVİYESİNİN ALGILANMASI İÇİN NANO MALZEME ESASLI OPTİK KİMYASAL SENSÖR GELİŞTİRİLMESİ

ÖZ

Rafineri gibi iş yerlerinde; uçucu ham petrol çözücüleri genellikle de alkanlar, siklik alkanlar, alkenler ve aromatiklerin karışımı bulunur. Bu tür atmosferlerde oksijen yetersizliği tehlikesine ilişkin yeterli sensör uyarımı sağlanamayabilir. Bu nedenle, bu tür ortamlarda oksijenin doğru ve devamlı kontrolü çok önemlidir. Diğer taraftan, rutenyum (II) türevleri oksijene duyarlı boyalar olarak bilinmekte olup, optik kimyasal sensörlerin dizaynında yoğun olarak kullanılmaktadır. Birçok rutenyum boyasının suda çözünür olmasından dolayı tutuklandığı matriksden akması söz konusudur. Bu problemin üstesinden gelmek için boyanın yapısı değiştirilirken oksijene karşı duyarlılığı azalmaktadır. Bu çalışmada, boya ve matriksin uyumuna çok önem verilmiş, parlak rutenyum (II) türevlerinin emisyonu dayalı oksijen algılama özellikleri bazı uçucu organiklerin varlığında ve yokluğunda test edilmiştir. Yeni sentezlenmiş iki farklı turuncu-kırmızı alkil dallanmış rutenyum komplekslerinin oksijene duyarlılıklarını test etmek amacı ile iki farklı silikon matriksde gümüş nanoparçacıkları ile kullanılmıştır. Kullanılan boyaların alkil dallanmış özelliklerinden dolayı boyalar, matriks içerisinde herhangi bir akma olmadan başarı ile enkapsüle edilmiştir. Algılayıcı materyaller ince film ve elektro eğrilmiş nanofiberler olarak üretilmiştir. Oksijene cevabını arttırmak için iyonik sıvı ve perfloro bileşikler katkı maddesi olarak kullanılmıştır. 630 nm’de oksijen etkisi ile gerçekleşen spektral değişimler gaz haldeki ve çözünmüş oksijenin analizinde analitik sinyal olarak izlenmiştir. Problemlerin oksijene duyarlılığı lifetime ve kinetik modda da test edilmiştir. Ampifilik rutenyum boyaları AgNP’ler ile birlikte silikonda elektro eğrilmiş fiberler formunda kullanıldığında uzun zamanlı kararlılık, artmış yüzey alanı, hassaslık ve bütün sensör dinamiklerinde iyileşme avantajları elde edilmiştir. Önerilen tasarımların algılama özellikleri rafineri ve benzeri iş yerlerinde bulunan benzen, toluen, etilbenzen, hegzan ve ksilen buharlarında test ve kalibre edilmiştir.

Anahtar kelimeler: Oksijen, çözünmüş oksijen, sensör, nanofiber, gümüş nanoparçacıklar, uçucu organik bileşikler.

CONTENTS

	Page
MSc. THESIS EXAMINATION RESULT FORM.....	ii
ACKNOWLEDGMENTS	iii
ABSTRACT.....	iv
ÖZ	vi
LIST OF FIGURES	xi
LIST OF TABLES	xx
CHAPTER ONE - INTRODUCTION	1
1.1 Air Quality and Oxygen Depletion in Refinery Related Workplaces	1
1.2 Exposure Limits for Volatile Organic Compounds (VOCs).....	2
1.3 Sensor Definition.....	4
1.3.1 Classification of Optical Chemical Sensors	6
1.3.2 Fiber Optic Sensors.....	6
1.3.3 Optical Sensors Based on Chromo/Fluoro- ionophores	7
1.4 Luminescence	8
1.4.1 Mechanism of Luminescence	8
1.4.1.1 Internal Conversion.....	9
1.4.1.2 Fluorescence	10
1.4.1.3 Intersystem Crossing.....	10
1.4.1.4 Phosphorescence	10
1.4.2 Fluorescence Quenching.....	12
1.4.3 Environmental Factors Effecting Fluorescence.....	13
1.4.4 Fluorescence Lifetime	14
1.4.4.1 Instrumentation for Time Correlated Single Photon Counting (TCSPC).....	16
1.4.4.2 Frequency Domain Lifetime Measurement	17
1.4.5 Quantum Yield.....	18

CHAPTER TWO - EXPERIMENTAL METHOD AND INSTRUMENTATION

..... 19

2.1 Reagents	19
2.2 Structural Specification of Ruthenium Dyes.....	20
2.3 Fabrication of Silver Nanoparticiles.....	21
2.3.1 Characterization of Silver Nanoparticles.....	22
2.3.2 Plasmon Absorption of Silver Nanoparticles	23
2.4 Fabrication of Thin Films.....	24
2.5 Fabrication of Electrospun Nanofibers.....	25
2.5.1 Electrospinning Apparatus.....	25
2.6 Instruments	26
2.6.1 Spectrophotometer and Spectrofluorometer Apparatus.....	26
2.6.2 Gas Blender	27
2.6.3 Particle Size Distribution Analyzer	28
2.6.4 X-Ray Diffractometer	28

CHAPTER THREE - OXYGEN SENSING STUDIES..... 29

3.1 Introduction	29
3.2 Spectral Characterization of Fluoroionophore	37
3.2.1 Absorption Spectra Related Characteristic	37
3.2.2 Emission Spectra Related Characteristic	39
3.2.3 Quantum Yield Calculations.....	41
3.2.4 SEM Images of Electrospun Membranes	43
3.3 Oxygen Sensing Studies.....	45
3.3.1 Oxygen Sensing Studies in Clean Air	45
3.3.2 Stern–Volmer Analysis of the Plots Recorded in Clean Air	54
3.3.3 Oxygen Sensing Studies under Volatile Organic Compounds	57
3.3.4 Stern-Volmer Analysis of the Plots Recorded Under VOCs.....	65
3.4. Lifetime Based Measurements	68
3.5 Response and Regeneration Characteristics.....	77

3.6. Results for Dissolved Oxygen	93
3.7 Selectivity Studies and Interference Effects.....	103
CHAPTER FOUR - CONCLUSION	105
REFERENCES.....	107

LIST OF FIGURES

	Page
Figure 1.1 Main aspects of fluorescent molecular sensors.	7
Figure 1.2 The Perrin–Jablonski diagram.	9
Figure 1.3 Absorption and emission spectra of Rhodamine 6G with ~25 nm Stokes shift.	12
Figure 1.4 Plots of single and multi-exponential decays.	15
Figure 1.5 Schematic representation of single and multi-exponential decay curves.	16
Figure 1.6 The main components for signal processing in TCSPC.	17
Figure 1.7 Frequency domain lifetime measurements.	17
Figure 2.1 Structures of the exploited dyes [Ru(bpy) ₂ (4-dihexylmethyl-4'-heptyl-2,2'-bipyridine)](PF ₆) ₂ (CS91) and [Ru(bpy) ₂ (4,4'-bis(3-ethylheptyl)-2,2'-bipyridine)](PF ₆) ₂ (CS93).	20
Figure 2.2 Colloidal silver in various stages of aggregation, (A) clear yellow sol, (B) dark yellow sol, (C) violet sol, and (D) grayish sol, as aggregation proceeds.	21
Figure 2.3 Size distribution analysis results of the fabricated AgNPs.	22
Figure 2.4 X-ray diffraction of synthesized silver nanoparticles.	23
Figure 2.5 Ag 3d XPS spectra of Ag nanoparticles on ITO substrates.	23
Figure 2.6 The UV–Vis absorption spectra of the different size of AgNPs during production. a: in the beginning of formation of AgNPs, b and c: particle diameter around 70 nm, d,e,f,g and h: average particle diameter at 100, 170, 240-1000 nm. B and c correspond to yellow sol and g and h correspond to grey sol.	24
Figure 2.7 The most frequently used electrospinning set-up.	26
Figure 2.8 Time resolved fluorescence spectrometer of Edinburg Instruments of FLS920.	27
Figure 2.9 Gas blender and oxygen and nitrogen gases.	27
Figure 3.1 Absorption spectrum of CS91 dye in THF.	37
Figure 3.2 Absorption spectrum of CS93 dye in THF.	38

Figure 3.3 Absorption spectrum of poly(TMSP) embedded CS91 in the absence (a) and presence (b) of AgNPs.	38
Figure 3.4 Absorption spectrum of silicon embedded CS93 in the absence (a) and presence (b) of AgNPs.	39
Figure 3.5 Excitation and emission spectrum of CS91 dye in THF.	40
Figure 3.6 Excitation and emission spectrum of CS91 dye in THF.	40
Figure 3.7 The integrated fluorescence intensities vs absorbance values of HPTS in alkaline solution, CS91 in THF and silicon matrix in the absence and presence of AgNPs.	42
Figure 3.8 The integrated fluorescence intensities vs absorbance values of HPTS in alkaline solution, CS93 in THF and silicon matrix in the absence and presence of AgNPs.	43
Figure 3.9 SEM photographs of electrospun nanofibers, micro fibers and mesoporous structures under different magnifications. (a): the CS93 embedded in Ag-free poly(TMSP), (b): Ag containing poly(TMSP), (c): Ag-free silicon, (d): Ag containing silicon.	44
Figure 3.10 Oxygen responses of the thin film of the CS91 dye in poly(TMSP) matrix. Oxygen concentrations were shown in graphic for all results respectively.	45
Figure 3.11 Oxygen responses of the AgNPs including thin film of the CS91 dye in poly(TMSP) matrix. Oxygen concentrations were shown in graphic for all results respectively.	46
Figure 3.12 Oxygen responses of the nanofibers of the CS91 dye in poly(TMSP) matrix. Oxygen concentrations were shown in graphic for all results respectively.	46
Figure 3.13 Oxygen responses of the AgNPs including nanofibers of the CS91 dye in poly(TMSP) matrix. Oxygen concentrations were shown in graphic for all results respectively.	47
Figure 3.14 Oxygen responses of the thin film of the CS91 dye in silicon matrix. Oxygen concentrations were shown in graphic for all results respectively.	47

Figure 3.15 Oxygen responses of the AgNPs including thin film of the CS91 dye in silicon matrix. Oxygen concentrations were shown in graphic for all results respectively.....	48
Figure 3.16 Oxygen responses of the nanofiber of the CS91 dye in silicon matrix. Oxygen concentrations were shown in graphic for all results respectively.	48
Figure 3.17 Oxygen responses of the AgNPs including nanofiber of the CS91 dye in silicon matrix. Oxygen concentrations were shown in graphic for all results respectively.....	49
Figure 3.18 Oxygen responses of the thin film of the CS93 dye in poly(TMSP) matrix. Oxygen concentrations were shown in graphic for all results respectively.	49
Figure 3.19 Oxygen responses of the AgNPs including thin film of the CS93 dye in poly(TMSP) matrix. Oxygen concentrations were shown in graphic for all results respectively.....	50
Figure 3.20 Oxygen responses of the nanofibers of the CS93 dye in poly(TMSP) matrix. Oxygen concentrations were shown in graphic for all results respectively.	50
Figure 3.21 Oxygen responses of the AgNPs including nanofibers of the CS93 dye in poly(TMSP) matrix. Oxygen concentrations were shown in graphic for all results respectively.....	51
Figure 3.22 Oxygen responses of the thin film of the CS93 dye in silicon matrix. Oxygen concentrations were shown in graphic for all results respectively.	51
Figure 3.23 Oxygen responses of the AgNPs thin film of the CS93 dye in silicon matrix. Oxygen concentrations were shown in graphic for all results respectively.....	52
Figure 3.24 Oxygen responses of the nanofibers of the CS93 dye in silicon matrix. Oxygen concentrations were shown in graphic for all results respectively.	52

Figure 3.25 Oxygen responses of the AgNPs including nanofibers of the CS93 dye in silicon matrix. Oxygen concentrations were shown in graphic for all results respectively.....	53
Figure 3.26 Gathered Stern-Volmer plots of nanofibers and thin films of CS91 dye in polyTMSP matrix.....	55
Figure 3.27 Gathered Stern-Volmer plots of nanofibers and thin films of CS93 dyes in silicon matrix.	56
Figure 3.28 Oxygen responses of the thin film of the CS91 dye in poly(TMSP) matrix in the presence of VOCs. Oxygen concentrations were shown in graphic for all results respectively.	58
Figure 3.29 Oxygen responses of the AgNPs including thin film of the CS91 dye in poly(TMSP) matrix in the presence of VOCs. Oxygen concentrations were shown in graphic for all results respectively.....	58
Figure 3.30 Oxygen responses of the nanofiber of the CS91 dye in poly(TMSP) matrix in the presence of VOCs. Oxygen concentrations were shown in graphic for all results respectively.	59
Figure 3.31 Oxygen responses of the AgNPs including nanofiber of the CS91 dye in poly(TMSP) matrix in the presence of VOCs. Oxygen concentrations were shown in graphic for all results respectively.....	59
Figure 3.32 Oxygen responses of the thin film of the CS91 dye in silicon matrix in the presence of VOCs. Oxygen concentrations were shown in graphic for all results respectively.	60
Figure 3.33 Oxygen responses of the AgNPs including thin film of the CS91 dye in silicon matrix in the presence of VOCs. Oxygen concentrations were shown in graphic for all results respectively.	60
Figure 3.34 Oxygen responses of the nanofiber of the CS91 dye in silicon matrix in the presence of VOCs. Oxygen concentrations were shown in graphic for all results respectively.	61
Figure 3.35 Oxygen responses of the AgNPs including nanofiber of the CS91 dye in silicon matrix in the presence of VOCs. Oxygen concentrations were shown in graphic for all results respectively.	61

Figure 3.36 Oxygen responses of the thin film of the CS93 dye in poly(TMSP) matrix in the presence of VOCs. Oxygen concentrations were shown in graphic for all results respectively.	62
Figure 3.37 Oxygen responses of the AgNPs including thin film of the CS93 dye in poly(TMSP) matrix in the presence of VOCs. Oxygen concentrations were shown in graphic for all results respectively.....	62
Figure 3.38 Oxygen responses of the nanofiber of the CS93 dye in poly(TMSP) matrix in the presence of VOCs. Oxygen concentrations were shown in graphic for all results respectively.	63
Figure 3.39 Oxygen responses of the AgNPs including nanofiber of the CS93 dye in poly(TMSP) matrix in the presence of VOCs. Oxygen concentrations were shown in graphic for all results respectively.....	63
Figure 3.40 Oxygen responses of the thin film of the CS93 dye in silicon matrix in the presence of VOCs. Oxygen concentrations were shown in graphic for all results respectively.	64
Figure 3.41 Oxygen responses of the AgNPs including thin film of the CS93 dye in silicon matrix in the presence of VOCs. Oxygen concentrations were shown in graphic for all results respectively.	64
Figure 3.42 Oxygen responses of the nanofiber of the CS93 dye in silicon matrix in the presence of VOCs. Oxygen concentrations were shown in graphic for all results respectively.	65
Figure 3.43 Oxygen responses of the AgNPs including nanofiber of the CS93 dye in silicon matrix in the presence of VOCs. Oxygen concentrations were shown in graphic for all results respectively.	65
Figure 3.44 Gathered Stern-Volmer plots of nanofibers and thin films of CS91 dye in polyTMSP matrix in the presence of VOCs	66
Figure 3.45 Gathered Stern-Volmer plots of nanofibers and thin films of CS93 dye in silicon matrix in the presence of VOCs.	66
Figure 3.46 Lifetime measurements of the poly(TMSP) embedded CS91 in the presence of AgNPs under oxygen free condition(a) and fully oxygenated (b) in clean air.....	69

Figure 3.47 Lifetime measurements of the poly(TMSP) embedded CS91 under oxygen free condition(a) and fully oxygenated (b) in clean air.....	70
Figure 3.48 Lifetime measurements of the poly(TMSP) embedded CS91 in the presence of AgNPs under oxygen free condition(a) and fully oxygenated (b) in the presence of VOCs.....	71
Figure 3.49 Lifetime measurements of the poly(TMSP) embedded CS91 under oxygen free condition(a) and fully oxygenated (b) in the presence of VOCs.	72
Figure 3.50 Lifetime measurements of the silicon embedded CS93 in the presence of AgNPs under oxygen free condition (a) and fully oxygenated (b) in clean air.....	73
Figure 3.51 Lifetime measurements of the silicon embedded CS93 under oxygen free condition (a) and fully oxygenated (b) in clean air.....	74
Figure 3.52 Lifetime measurements of the silicon embedded CS93 in the presence of AgNPs under oxygen free condition (a) and fully oxygenated (b) in the presence of VOCs.	75
Figure 3.53 Lifetime measurements of the silicon embedded CS93 under oxygen free condition (a) and fully oxygenated (b) in the presence of VOCs.....	76
Figure 3.54 Kinetic results of the thin film of the CS91 dye in poly(TMSP) matrix. ...	77
Figure 3.55 Kinetic results of the AgNPs including thin film of the CS91 dye in poly(TMSP) matrix.....	78
Figure 3.56 Kinetic results of the nanofibers of the CS91 dye in poly(TMSP) matrix.	78
Figure 3.57 Kinetic results of the AgNPs including nanofibers of the CS91 dye in poly(TMSP) matrix.....	79
Figure 3.58 Kinetic results of the thin film of the CS91 dye in silicon matrix.....	79
Figure 3.59 Kinetic results of the AgNPs including thin film of the CS91 dye in silicon matrix.	80
Figure 3.60 Kinetic results of the nanofiber of the CS91 dye in silicon matrix.	80
Figure 3.61 Kinetic results of the AgNPs including nanofiber of the CS91 dye in silicon matrix.	81

Figure 3.62 Kinetic results of the thin film of the CS93 dye in poly(TMSP) matrix. ...	81
Figure 3.63 Kinetic results of the AgNPs including thin film of the CS93 dye in poly(TMSP) matrix.....	82
Figure 3.64 Kinetic results of the nanofibers of the CS93 dye in poly(TMSP) matrix.	82
Figure 3.65 Kinetic results of the AgNPs including nanofibers of the CS93 dye in poly(TMSP) matrix.....	83
Figure 3.66 Kinetic results of the thin film of the CS93 dye in silicon matrix.....	83
Figure 3.67 Kinetic results of the AgNPs thin film of the CS93 dye in silicon matrix.	84
Figure 3.68 Kinetic results of the nanofibers of the CS93 dye in silicon matrix.....	84
Figure 3.69 Kinetic results of the AgNPs nanofiber of the CS93 dye in silicon matrix.	85
Figure 3.70 Kinetic results of the thin film of the CS91 dye in poly(TMSP) matrix in the presence of VOCs.	85
Figure 3.71 Kinetic results of the AgNPs including thin film of the CS91 dye in poly(TMSP) matrix in the presence of VOCs.	86
Figure 3.72 Kinetic results of the nanofiber of the CS91 dye in poly(TMSP) matrix in the presence of VOCs.	86
Figure 3.73 Kinetic results of the AgNPs including nanofiber of the CS91 dye in poly(TMSP) matrix in the presence of VOCs.	87
Figure 3.74 Kinetic results of the thin film of the CS91 dye in silicon matrix in the presence of VOCs.	87
Figure 3.75 Kinetic results of the AgNPs including thin film of the CS91 dye in silicon matrix in the presence of VOCs.....	88
Figure 3.76 Kinetic results of the nanofiber of the CS91 dye in silicon matrix in the presence of VOCs.....	88
Figure 3.77 Kinetic results of the AgNPs including nanofiber of the CS91 dye in silicon matrix in the presence of VOCs.....	89
Figure 3.78 Kinetic results of the thin film of the CS93 dye in poly(TMSP) matrix in the presence of VOCs.	89

Figure 3.79 Kinetic results of the AgNPs including thin film of the CS93 dye in poly(TMSP) matrix in the presence of VOCs.	90
Figure 3.80 Kinetic results of the nanofiber of the CS93 dye in poly(TMSP) matrix in the presence of VOCs.....	90
Figure 3.81 Kinetic results of the AgNPs including nanofiber of the CS93 dye in poly(TMSP) matrix in the presence of VOCs.	91
Figure 3.82 Kinetic results of the thin film of the CS93 dye in silicon matrix in the presence of VOCs.	91
Figure 3. 83 Kinetic results of the AgNPs including thin film of the CS93 dye in silicon matrix in the presence of VOCs.....	92
Figure 3.84 Kinetic results of the nanofiber of the CS93 dye in silicon matrix in the presence of VOCs.	92
Figure 3.85 Kinetic results of the AgNPs including nanofiber of the CS93 dye in silicon matrix in the presence of VOCs.....	93
Figure 3.86 Response of CS91 to dissolved oxygen. The dye is embedded in poly(TMSP) and is in thin film form.	94
Figure 3.87 Response of CS91 to dissolved oxygen. The dye is embedded in AgNPs including poly(TMSP) and is in thin film form.....	94
Figure 3.88 Response of CS91 to dissolved oxygen. The dye is embedded in poly(TMSP) and is in nanofiber form.....	95
Figure 3.89 Response of CS91 to dissolved oxygen. The dye is embedded in AgNPs including poly(TMSP) and is in nanofiber form.	95
Figure 3.90 Response of CS91 to dissolved oxygen. The dye is embedded in silicon and is in nanofiber form.	96
Figure 3.91 Response of CS91 to dissolved oxygen. The dye is embedded in AgNPs including silicon and is in nanofiber form.	96
Figure 3.92 Response of CS93 to dissolved oxygen. The dye is embedded in poly(TMSP) and is in thin film form.	97
Figure 3.93 Response of CS93 to dissolved oxygen. The dye is embedded in AgNPs including poly(TMSP) and is in thin film form.	97
Figure 3.94 Response of CS93 to dissolved oxygen. The dye is embedded in silicon and is in thin film form.....	98

Figure 3.95 Response of CS93 to dissolved oxygen. The dye is embedded in AgNPs including silicon and is in thin film form.	98
Figure 3.96 Response of CS93 to dissolved oxygen. The dye is embedded in poly(TMSP) and is in thin nanofiber form.	99
Figure 3.97 Response of CS93 to dissolved oxygen. The dye is embedded in AgNPs including poly(TMSP) and is in thin nanofiber form.	99
Figure 3.98 Response of CS93 to dissolved oxygen. The dye is embedded in silicon and is in thin nanofiber form.	100
Figure 3.99 Response of CS93 to dissolved oxygen. The dye is embedded in AgNPs including silicon and is in thin nanofiber form.	100
Figure 3.100 Gathered Stern-Volmer plots of nanofibers and thin films of CS91 dye in poly(TMSP) matrix for oxygen dissolved studies.	101
Figure 3.101 Gathered Stern-Volmer plots of nanofibers and thin films of CS91 dye in silicon matrix for oxygen dissolved studies.	101
Figure 3.102 Gathered Stern-Volmer plots of nanofibers and thin films of CS93 dye in poly(TMSP) matrix for oxygen dissolved studies.	102
Figure 3.103 Gathered Stern-Volmer plots of nanofibers and thin films of CS93 dye in silicon matrix for oxygen dissolved studies.	102
Figure 3.104 Response of CS93 dye in THF to 10^{-5} M of different metal cations in acetic acid/acetate buffer solutions at pH 4.0.	104
Figure 3.105 Response of CS91 dye in THF to 10^{-5} M of different metal cations in acetic acid/acetate buffer solutions at pH 4.0.	104

LIST OF TABLES

	Page
Table 1.1 The exposure limits of benzene, toluene, xylene, ethyl benzene, and hexane (TWA=Time-weighted average; TLV=Threshold Limit Value; STEL=Short-term Exposure Limit; MCL=Maximum Contamination Limit, PEL=Personal Exposure Limit, REL=Recommended Exposure Limit; IDHL=Immediately Dangerous to Life and Health concentration).	3
Table 2.1 Compositions of the exploited sensing agents	25
Table 3.1 A short summary of the Ru based O ₂ sensing studies. (NR: not reported, Ref.: Reference)	32
Table 3.2 The absorption spectra related characteristics of the dyes in different moieties.	39
Table 3.3 Fluorescence spectra related characteristics of the CS91 and CS93 in poly(TMSP), silicon and in THF.	41
Table 3.4 Emission spectra related characteristics.....	54
Table 3.5 The Stern Volmer plots for clean air and contaminated conditions, oxygen induced relative signal changes, related regression coefficients and K _{sv} values extracted from the slopes of the plots.....	57
Table 3.6 The Stern Volmer plots for contaminated conditions of volatile organics, oxygen induced relative signal changes, related regression coefficients and K _{sv} values extracted from the slopes of the plots.	67
Table 3.7 Studied temperatures of the water bath for dissolved oxygen studies.	94
Table 3.8 The Stern Volmer plots for dissolved oxygen studies, oxygen induced relative signal changes, related regression coefficients and K _{sv} values extracted from the slopes of the plots.....	103

CHAPTER ONE

INTRODUCTION

1.1 Air Quality and Oxygen Depletion in Refinery Related Workplaces

Oil refineries are industrial plants, which convert crude oil into variety of petroleum products. Refinery operations are associated with the emission of a wide variety of volatile organic compounds (VOCs) into the atmosphere, mainly originating from production processes in the distillation, catalytic cracking, alkylation and isomerization units, storage tanks, and distribution terminals (Kalabokas, Hatzianestis, Bartzis, & Papagiannakopoulos, 2001). The transportation, distribution and marketing of the refined products involve many distinct operations, each of which represents a potential source of evaporation, loss and occupational exposure problem for the workers (Singh, Ramteke, Juneja, & Pandya, 2013).

Refinery workers are potential risk groups for exposure to benzene, toluene, ethylbenzene, and xylenes (BTEX) and the other volatile organic compounds (VOCs) from routine sampling, operations, releases from large bulk facilities, surface spills and pipeline leaks. BTEX is released into the environment by a volatilization (evaporation) process. The most potential pathways to exposure the VOCs include inhalation, and absorption through skin. Common exposure symptoms to volatile organics include respiratory problems, skin and sensory irritation, central nervous system depression and headache. Severe or prolonged exposure may result in kidney, liver and blood system diseases. Benzene is identified as a human carcinogen that can cause myeloid leukemia. All of these volatile organics may cause oxygen depletion in the atmosphere of the refinery. In such conditions, accurate determination of oxygen levels may not be possible. Therefore, the potential interference effects of the subjective compounds should be considered.

1.2 Exposure Limits for Volatile Organic Compounds (VOCs)

The presence of VOCs is inevitable in refinery related workplaces. They are allowed to some extent to be present in the ambient air of the work place unless their concentration over the limits. There may be several values and types of limits. Here the exposure limits were given in terms of the conventions of **Occupational Safety and Health Administration (OSHA)**, **American Conference of Governmental Industrial Hygienists (ACGIH®)**, and **The National Institute for Occupational Safety and Health (NIOSH)**. The **OSHA Personal Exposure Limits (PEL)** was given as **Time-weighted average (TWA)** and **Short-term Exposure Limit (STEL)**. The **NIOSH** limits were determined as **Recommended Exposure Limit (REL)** and **Immediately Dangerous to Life and Health concentration (IDLH)** (Petrochemical VOCs analysis, 2015). Both the **PEL** and **TLV** specify the maximum amount of exposure a worker can have to a substance averaged over an 8-hour workday. The limits are usually expressed in parts per million parts of air (ppm) or milligrams of dust or vapor per cubic meter of air (mg/m^3). On the other hand, the **Short Term Exposure Limit (STEL)** is a term used by the **ACGIH** to express the maximum concentration most workers can tolerate for a 15-minute exposure period without adverse effects (with a maximum of four periods a day and at least 60 minutes between exposure periods) (University of Wisconsin - Safety Department, n.d.).

In this work, an optical chemical oxygen sensor has been developed and the interference effects of VOCs of benzene, toluene, xylene, ethyl benzene and hexane on sensing ability of the oxygen have been tested and evaluated. The exposure limits of benzene, toluene, xylene, ethyl benzene, and hexane were given in Table 1.1.

Table 1.1 The exposure limits of benzene, toluene, xylene, ethyl benzene, and hexane (TWA=Time-weighted average; TLV=Threshold Limit Value; STEL=Short-term Exposure Limit; MCL=Maximum Contamination Limit, PEL=Personal Exposure Limit, REL=Recommended Exposure Limit; IDHL=Immediately Dangerous to Life and Health concentration) (Petrochemical VOCs analysis, 2015).

Contaminant	OSHA(PEL) Exposure Limit			ACGIH (TLV) Exposure Limit	NIOSH (REL) Exposure Limit	NIOSH (IDHL) Exposure Limit	In this work (ppm)
	for General Industry	for Construction Industry	for Maritime				
Benzene	1 ppm TWA with a 5 ppm STEL; 0.5 ppm Action Level	1 ppm TWA with a 5 ppm STEL; 0.5 ppm Action Level	1 ppm TWA with a 5 ppm STEL; 0.5 ppm Action Level	0.5 ppm TWA; 2.5 ppm STEL; Skin; Confirmed human carcinogen	0.1 ppm TWA; 1 ppm STEL	800 ppm	98900
Toluene	200 ppm (750 mg/m ³) TWA; 300 ppm Ceiling	200 ppm (750 mg/m ³) TWA	200 ppm (750 mg/m ³) TWA; 100 ppm Skin TWA	50 ppm (188 mg/m ³) TWA; skin; Not a human carcinogen	100 ppm (375 mg/m ³) TWA; 150 ppm (560 mg/m ³) STEL	500 ppm	28900
Xylene (o-, p-, m-isomers)	100 ppm (435 mg/m ³) TWA	100 ppm (435 mg/m ³) TWA	: 100 ppm (435 mg/m ³) TWA	100 ppm (434 mg/m ³) TWA; 150 ppm (651 mg/m ³) STEL; Not a human carcinogen	100 ppm (435 mg/m ³) TWA; 150 ppm (655 mg/m ³) STEL	900 ppm	8110
Ethylbenzene	100 ppm (435 mg/m ³) TWA		100 ppm (435 mg/m ³) TWA	100 ppm TWA; 125 ppm STEL; Confirmed Animal Carcinogen	100 ppm (435 mg/m ³) TWA; 125 ppm (545 mg/m ³) STEL; Confirmed Animal Carcinogen	800 ppm	13200

1.3 Sensor Definition

A chemical sensor is a device that gives an analytical useful signal as a result of a chemical interaction or process between the analyte and the sensor device. Chemical sensors can be used for the qualitative or quantitative determination of the analytes of the interest (Wolfbeis, 1991).

Mainly a chemical sensor has a specific chemical or molecular target to be measured. There are a few definitions for optical sensors. According to the definition of IUPAC (International Union of Pure and Applied Chemistry) a chemical sensor has been defined as follows:

A chemical sensor is a device that transforms chemical information, ranging from the concentration of a specific sample component to total composition analysis, into an analytically useful signal. The chemical information, mentioned above, may originate from a chemical reaction of the analyte or from a physical property of the system investigated (Hulanicki, Glab, & Ingman, 1991, p.1248).

Chemical sensors contain two basic functional units: a receptor part and a transducer part. Some sensors may include a separator, which is, for example, a membrane. In the receptor part of a sensor the chemical information is transformed into a form of energy which may be measured by the transducer (Hulanicki, Glab, & Ingman, 1991).

The transducer part is a device capable of transforming the energy carrying the chemical information about the sample into a useful analytical signal. The transducer as such does not show selectivity. The receptor part of chemical sensors may be based upon various principles (Hulanicki, Glab, & Ingman, 1991, p.1248):

- Physical, where no chemical reaction takes place. Optical examples are those based upon measurement of absorbance, refractive index, conductivity, temperature or mass change.

- Chemical, in which a chemical reaction with participation of the analyte gives rise to the analytical signal.

- Biochemical in which a biochemical process is the source of the analytical signal (Hulanicki, Glab, & Ingman, 1991, p.1248).

According to the type of the transducer the chemical sensors can simply be classified as electrochemical, optical mass sensitive and heat-sensitive, considering to the type of transducer (Cattrall, 1997).

An optical chemical sensor normally consists of the following components:

1. A recognition unit, where a specific interaction between the recognition moiety and the analyte takes place and the sensor becomes selective for the analyte;
2. The transducer unit that converts the recognition process into a recordable optical signal;
3. Optical components, which mainly consists of a light source (Xenon lamp, a LED or a laser), sometimes fiber optics; lenses, and/or filters;
4. A detector (a photodiode in miniaturized devices or a photo multiplier tube in spectrophotometers), which detects the measured optical property;
5. Signal amplification, signal processing (conversion from optical to digital) and readout.

Except that of these forms and components, there may be other specific elements and designs.

1.3.1 Classification of Optical Chemical Sensors

Optical chemical sensors may be classified according to the structure of the transducer. If the fiber optics were exploited in the design of the sensor, they called as “fiber optic chemical sensors”. In another approach, they can be classified according to their usage like gas sensors (oxygen, carbon dioxide etc.), cation sensors (Ca(II), Cu(II), Zn(II), Fe(II) etc.), anion sensors, biosensors etc. In most of the optical chemical sensors, one of the following parameters was measured.

- a) **Absorbance** should be measured in a transparent medium, the absorptivity of the chromophore or chromoionophore may change after interaction with the analyte.
- b) **Fluorescence** may be measured for both transparent and opaque moieties. The fluorescence intensity or the fluorescence lifetime of a fluoroionophore or an emitting inorganic material may change after interaction with the analyte.
- c) **Reflectance** can be measured in non-transparent moieties.
- d) **Luminescence** is the intensity of light emitted after an excitation process.
- e) **Refractive index** measured as the result of a change in solution composition.
- f) **Optothermal effect**, the thermal effect observed after absorption of the light.
- g) **Light scattering**, scattering of the light by a particle in solution or in vacuum.

1.3.2 Fiber Optic Sensors

An optical fiber is mainly a flexible, transparent material made of glass or plastic. It works as a waveguide to transmit the light between the two ends of the fiber. Prior to the analysis, in the beginning, optical fibers were widely used in field of communication. Later, fibers were used for illumination, and produced in bundles so that they used to carry the light, allowing viewing in confined spaces. Today, specially designed fibers have been used for a variety of other applications, including optical chemical sensors.

An optical fiber typically consists of a transparent core surrounded by a transparent cladding material with a lower refraction index. Light is kept within the

The spectral changes are due to the perturbation (by the interaction of the analyte with ionophore) of photo induced processes such as electron transfer, charge transfer, energy transfer, excimer or exciplex formation or disappearance (Valeur, & Leray, 2000).

1.4 Luminescence

1.4.1 Mechanism of Luminescence

Luminescence means emission of light by electronically excited atoms or molecules. Electronic excitation requires the supply of energy. Various kinds of luminescence, such as electroluminescence, chemiluminescence, thermoluminescence and photoluminescence, are known and called by the source from which energy is derived (Lakowicz, 1993; Parker, 1968; Schmidt, 1994).

The Perrin–Jablonski diagram is a good way for understanding the possible processes: photon absorption, internal conversion, fluorescence, intersystem crossing, phosphorescence, and delayed fluorescence and triplet–triplet transitions (see Figure 1.2). The singlet electronic states were shown as S_0 (fundamental electronic state), S_1 ; S_2 (excited electronic states); ... and the triplet states, T_1 ; T_2 ; ... : Vibrational energy levels are associated with each electronic state. Among them absorption is the fastest process (1×10^{-15} s) with respect to all other transitions (Lakowicz, 1993; Parker, 1968; Schmidt, 1994).

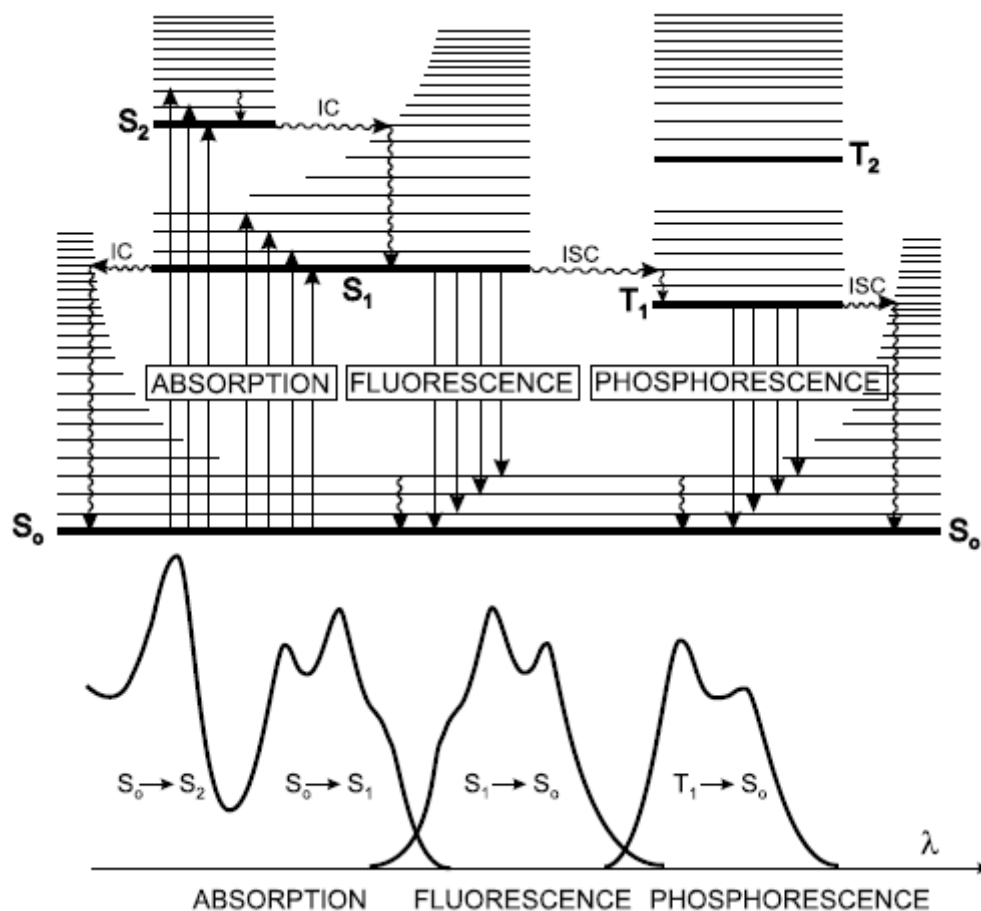


Figure 1.2 The Perrin-Jablonski diagram (Valeur, 2002).

Because the majority of molecules are in the lowest level S_0 at room temperature, the vertical arrows indicating to absorption start from the S_0 vibrational level. Absorption of a photon may cause transition of electrons to one of the upper vibrational levels of S_1 ; S_2 or S_3 (Lakowicz, 1993; Parker, 1968; Schmidt, 1994).

1.4.1.1 Internal Conversion

Internal conversion is a non-radiative transition between two electronic states in a molecule or atom. It is sometimes called "radiationless de-activation", because no photons are emitted. The energy of the electronically excited state is given off to vibrational modes of the molecule or to the solvent during collisions of the excited

molecule with the surrounding solvent molecules. The excitation energy is transformed into heat (Valeur, 2002).

1.4.1.2 Fluorescence

Once a molecule arrives at the lowest vibrational level of an excited singlet state, there are a few possible ways; one of which is to return to the ground state by photon emission. Emission of photons from the S_1 to S_0 relaxation is called fluorescence. The lifetime of an excited singlet state is approximately 10^{-9} to 10^{-7} second therefore the decay time of fluorescence is of the same order of magnitude. If fluorescence is unperturbed by competing processes, the lifetime of fluorescence is the intrinsic lifetime of the excited singlet state.

1.4.1.3 Intersystem Crossing

Intersystem crossing is a non-radiative transition between two isoenergetic vibrational levels belonging to electronic states of different multiplicities (Valeur, 2002). For example, an excited molecule in the 0 vibrational level of the S_1 state can move to the corresponding vibrational level of the T_n triplet state. Then vibrational relaxation occurs and it drops to the lowest vibrational level of T_1 . Intersystem crossing may be fast enough (10^{-7} – 10^{-9} s) to compete with other pathways of fluorescence and internal conversion.

1.4.1.4 Phosphorescence

In case of phosphorescence, the absorbed photon energy undergoes an unusual intersystem crossing into an energy state of higher spin multiplicity, usually a triplet state. As a result, the energy can become trapped in the triplet state with only classically "forbidden" transitions available to return to the lower energy state. Although forbidden and kinetically unfavored these transitions occur at significantly slower time scales. Most phosphorescent compounds exhibiting triplet lifetimes on the order of milliseconds, some compounds have triplet lifetimes up to minutes or

even hours. If the phosphorescent quantum yield is high, these substances will emit significant amounts of light over long time scales, creating so-called "glow-in-the-dark".

Molecular fluorescence is a result of an excitation process that occurs in certain molecules with long conjugated systems, joined aromatic cycles (polyaromatic hydrocarbons or heterocycles). This kind of molecules is denoted as fluorophores, fluorescent dyes.

In order to provide a fluorescent spectrum a photon energy should be supplied by an external light source such as a Xenon lamp or a laser and absorbed by the fluorophore, creating an excited electronic singlet state (S_1'). The excited state exists for a finite time (typically 1–10 nanoseconds). During this time, the fluorophore may undergo some conformational changes or may be subject to a number of possible interactions with its micro environment. The energy of S_1' may be partially dissipated from which the fluorescence emission originates. Not all the excited molecules return to the ground state (S_0) emitting fluorescence. Other processes such as collisional quenching, fluorescence resonance energy transfer (FRET) and intersystem crossing (ISC) are possible.

While the fluorophore returning to its ground state, photon energy is emitted. Due to energy lost during the excited-state lifetime, the energy of this photon is lower, and therefore of longer wavelength, than the excitation photon. The difference in energy or wavelength between excitation and emission photon is called the Stokes shift (see Figure 1.3).

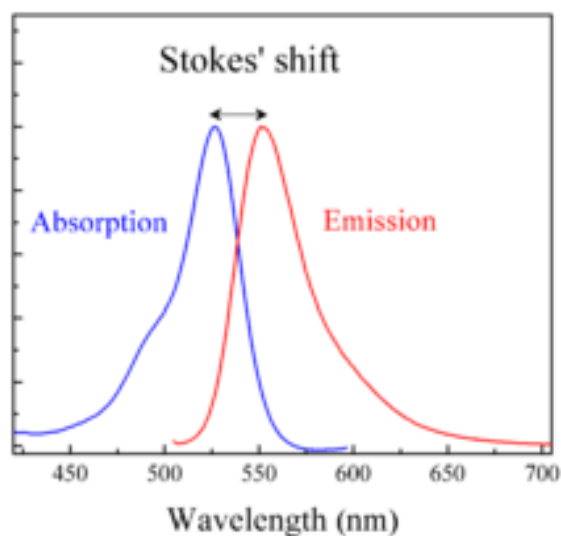


Figure 1.3 Absorption and emission spectra of Rhodamine 6G with ~25 nm Stokes shift (Wikipedia, 2015).

1.4.2 Fluorescence Quenching

Fluorescence quenching is a bimolecular process and causes a decrease in intensity of a fluorophore. Quenching can occur by different mechanisms like; excited-state reactions, molecular rearrangements, energy transfer, ground-state complex formation, and collisional quenching. Collisional quenching occurs when the excited-state fluorophore is deactivated upon contact with some other molecule in solution, which is called the quencher. In case of the collisional quenching the excited fluorophore is returned to the ground state during a diffusive encounter with the quencher. The molecules are not chemically altered in the process. For collisional quenching the decrease in intensity is described by the well-known Stern-Volmer equation (Lakowicz, 1983) : The Stern-Volmer equation can be written both in terms of fluorescence intensities (I) and fluorescence lifetimes (τ).

$$\frac{I_0}{I} = \frac{\tau_0}{\tau} = 1 + K_{sv}[Q] \quad (1.1)$$

$$K_{sv} = \tau_0 k \quad (1.2)$$

where $[Q]$ is the quencher concentration, I and τ are the fluorescence intensity and lifetime, respectively, I_0 and τ_0 are the unquenched intensity and lifetime, and k is the bimolecular quenching constant. The quantity K_{sv} is referred to as the Stern-Volmer constant. In case of collisional quenching, as the quencher concentration increases, the emission intensity and lifetime of the fluorophore decreases. Collisional quenching is also known as dynamic quenching. In the case of static quenching a complex forms between the fluorophore and the quencher, and this complex is non-fluorescent. The formation of this complex does not rely upon population of the excited state (Lakowicz, 1999).

Self-quenching is the quenching of one fluorophore by another; it appears when high concentrations of fluorophore are used. Fluorescence resonance energy transfer (FRET) is a strongly distance-dependent excited-state interaction in which emission integral of one fluorophore is coupled to the excitation integral of another.

1.4.3 Environmental Factors Effecting Fluorescence

Some environmental factors influence on fluorescence dynamics. The most important ones are:

- Solvent polarity,
- Proximity and concentrations of species, and
- In aqueous solutions pH of the medium.

Fluorescence spectra of a molecule may be strongly dependent on solvent. This characteristic is most often observed with fluorophores that have large excited-state dipole moments. Interaction of such kind of molecules with polar solvents results with spectral shifts in fluorescence spectra to longer wavelengths (Fluorescence fundamentals, 2015).

1.4.4 Fluorescence Lifetime

The fluorescence lifetime can be defined as the average time for a molecule to remain in the excited state before emitting a photon. Each individual molecule emits randomly after excitation. While some of the excited molecules fluorescing before the average lifetime, others fluoresce long after the average lifetime. Fluorescence lifetimes are generally on the order of 1-10 nanoseconds. However they can range from hundreds of nanoseconds to the sub nanosecond time scale.

The decay of the excited state of a molecule to the ground state can be expressed as;

$$I(t) = I_0 \exp\left(\frac{-t}{\tau}\right) \quad (1.3)$$

where, I_0 is the intensity at the beginning of excitation and τ is the lifetime. The decay time is defined as the time for the intensity to drop by $1/e$ or to 37% of τ . Figure 1.4 shows a typical decay curve. The lifetime equation can be written in terms of rate constants (k_r -radiative rate, k_{nr} - non radiative rate) as well as in terms of the fluorescence quantum yield (ϕ).

Each of the processes occurs with a certain probability, characterized by decay rate constants (k). It can be shown that the average length of time τ for the set of molecules to decay from one state to another is reciprocally proportional to the rate of decay: $\tau = 1/k$. This average length of time is called the mean lifetime, or simply lifetime.

$$\tau = \frac{1}{k_r + k_{nr}} \quad \phi = \frac{k_r}{k_r + k_{nr}} \quad (1.4)$$

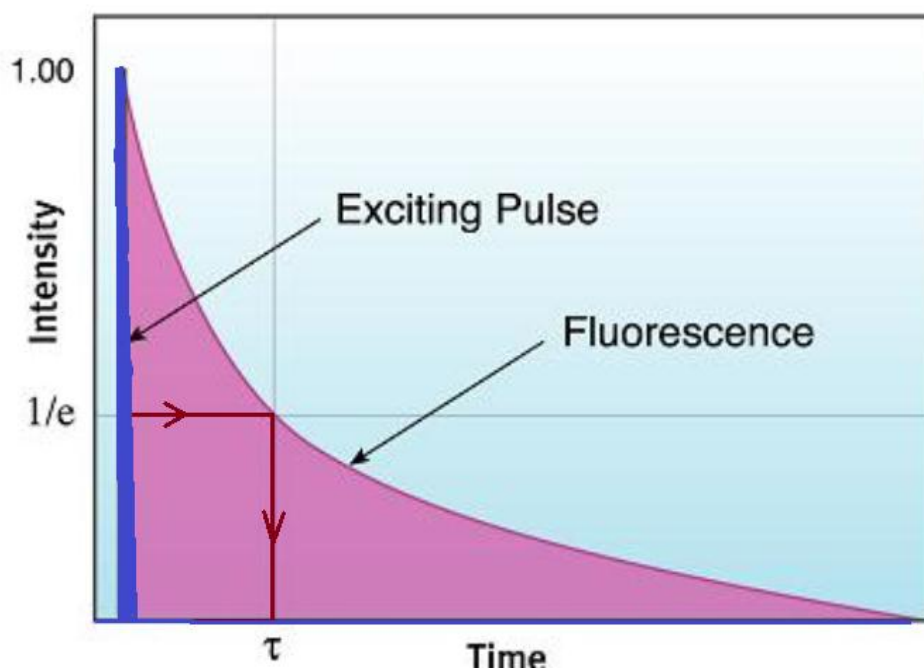


Figure 1.4 Plots of single and multi-exponential decays (Terpetschnig, & Jameson, n.d.) .

Although the decay law is based on first order kinetics, in application, many fluorescence decays may be more complex. Sometimes populations of excited molecules are in inhomogeneous environments and quenching processes and other environmental factors can lead to multi- or non-exponential decays. Plots of single and multi-exponential decays are shown in Figure 1.4. In the case of multi-exponential decays analogous analysis maybe necessary to find out the lifetimes and their fractions. An increase in the number of fitted parameters (more than 3 lifetimes) is an undesirable situation and is not recommended. In such cases average lifetime (mean lifetime) can be calculated considering percentage distribution of each component.

The fluorescence lifetime is an intrinsic molecular property and, within certain constraints, independent of concentration. This means that changes in concentration, whether caused by photo bleaching or diluting/concentrating the sample, would not affect the lifetime value. This is in contrast to a steady state measurement, where a change in intensity of the recorded emission would be observed (Time resolved fluorescence lifetime measurements, 2014).

Fluorescence lifetimes can be measurement in two different modes; time domain and frequency domain.

In the time domain mode, molecules are excited by a very short pulse of light at $t=0$ and immediately after the excitation, the decay of florescence intensity is measured. This can be performed by Time Correlated Single Photon Counting (TCSPC) approach.

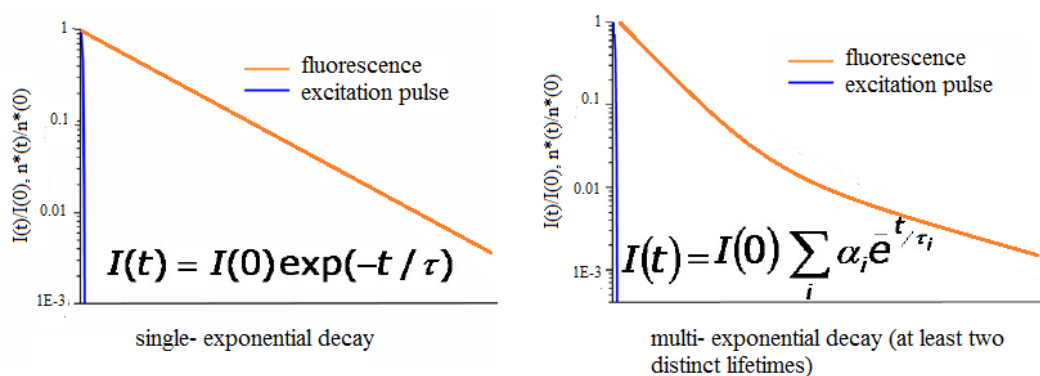


Figure 1.5 Schematic representation of single and multi-exponential decay curves.

1.4.4.1 Instrumentation for Time Correlated Single Photon Counting (TCSPC)

Time Correlated Single Photon Counting is a digital counting technique, counting photons that are time correlated in relation to an excitation “light pulse”. The main components for signal processing in TCSPC are constant fraction discriminators (CFD), electrical delays (DEL), the Time-to-Amplitude Converter (TAC), Amplifier (between the TAC and ADC), Analogue to Digital Converter (ADC) and digital memory (Mem) (see Figure 1.6).

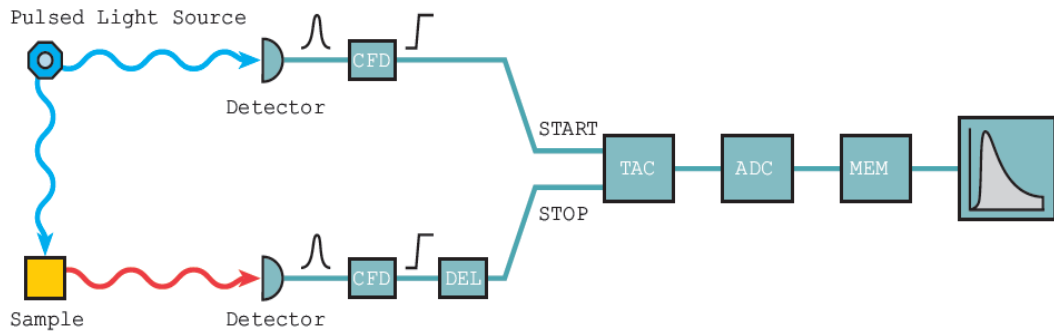


Figure 1.6 The main components for signal processing in TCSPC (FLS920 Series, 2011)

In TCSPC the sample is repetitively excited using a pulsed light source and the measurement builds a probability histogram relating the time between an excitation pulse (START) and the observation of the first fluorescence photon (STOP) (FLS920 Series, 2011).

1.4.4.2 Frequency Domain Lifetime Measurement

In frequency domain measurement excitation light is harmonically modulated with angular frequency f and then the phase angle was recorded. Fluorescence lifetimes can be calculated from the phase shift Φ (see Figure 1.7) (Wolfbeis, 1991).

$$\tan \Phi = 2\pi f \tau \quad \tau = \frac{\tan \Phi}{2\pi f} \quad (1.5)$$

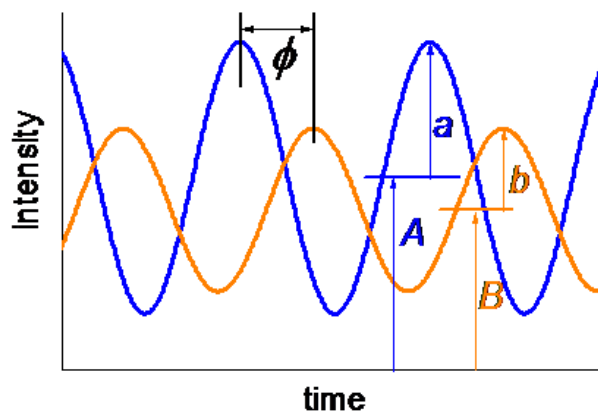


Figure 1.7 Frequency domain lifetime measurement (Thorlabs, n.d.).

1.4.5 Quantum Yield

The fluorescence quantum yield is a feature of fluorophore and it is important for characterization of newly introduced fluorescent probes. The fluorescence quantum yield is the ratio of photons emitted to photons absorbed through the fluorescence (Lakowicz, 1999; Parker, 1968; Schmidt, 1994).

$$\varphi = \frac{\text{photons}_{\text{em}}}{\text{photons}_{\text{abs}}} \quad (1.6)$$

The quantum yield φ can also be described by the relative rates of the radiative k_r and non-radiative k_{nr} relaxation pathways, which deactivate the excited state (Lakowicz, 1999; Parker, 1968; Schmidt, 1994).

$$\varphi = \frac{k_r}{k_r + \sum k_{nr}} \quad (1.7)$$

While the calculation of the absolute quantum yield requires sophisticated operations, the relative quantum yield of the fluorophore by comparison with a reference fluorophore quantum yield is determined more easily. There are two approaches for measurement of relative quantum yield: single-point method and comparative method.

In single-point method, the quantum yield is calculated using the integrated emission intensity of the same concentration of pair of a single sample and the reference. Although this method is fast and easy, due to incorrect measurement of the fluorophore's absorbance at a single concentration value may not always be reliable. The second is the comparative method of Williams *et al.*, which involves the use of multiple concentrations of well characterized references with known fluorescence quantum yields. It is more time consuming, but provides a much higher precision by calculating the slope of the line generated by plotting the absorption against the fluorescence intensity for multiple concentrations of the fluorophore (Lakowicz, 1999).

CHAPTER TWO

EXPERIMENTAL METHOD AND INSTRUMENTATION

2.1 Reagents

Oxygen sensitive fluorescent dyes utilized in this thesis were synthesized and provided by Dr. Canan Varlikli. The dyes of $[\text{Ru}(\text{bpy})_2(4\text{-dihexylmethyl-4}'\text{-heptyl-2,2}'\text{-bipyridine})](\text{PF}_6)_2$ and $[\text{Ru}(\text{bpy})_2(4,4'\text{-bis(3-ethylheptyl)-2,2}'\text{-bipyridine})](\text{PF}_6)_2$ were encoded as CS91 and CS93, respectively. Synthetic route of the dyes was published earlier (Oner, Sahin, & Varlikli, 2012).

Poly-1-trimethylsilyl-1-propyne (poly(TMSP)) was purchased from ABCR Company. Silicon was purchased from Alkim. The plasticizer, dioctyl phthalate (DOP) was supplied from Aldrich. 1-butyl-3-methylimidazolium tetrafluoroborate ($[\text{BMI}^+][\text{BF}_4^-]$) was from Fluka. The perfluorinated compounds (PFC); nonadecafluorodecanoic acid was purchased from Alfa Aesar. Silver nitrate (99% AgNO_3) and sodium borohydride (99% NaBH_4) were purchased from Merck and Aldrich Chemical Companies, respectively. Millipore ultra-pure water was used throughout the studies. Glassware was cleaned by soaking in alcoholic KOH. Oxygen and nitrogen gas cylinders were of 99.99% purity and obtained from Linde Gas Company, Izmir, Turkey.

The calibration and metal sensing studies were performed by using atomic absorption spectroscopy (AAS) certified reference standard solutions of Ag^+ , Al^{3+} , Ba^{2+} , Ca^{2+} , Co^{2+} , Cr^{3+} , Cu^{2+} , Fe^{3+} , Fe^{2+} , Hg_2^{2+} , Hg^{2+} , Li^+ , K^+ , Mn^{2+} , Mg^{2+} , Na^+ , NH_4^+ , Ni^{2+} , Pb^{2+} , Sn^{2+} and Zn^{2+} . All standards were diluted with 0.01 M acetic acid/acetate buffer of pH 5.0 and were prepared in polyethylene measuring flask to avoid adsorption of metal ions. All of the experiments were carried out at room temperature; 25 ± 1 °C. The pH of the solutions were monitored by use of a digital pH-meter (ORION) calibrated with standard buffers of pH 12.00, 7.00 and 4.00 at 25 ± 1 °C. All of the experiments were carried out at room temperature; 25 °C.

2.2 Structural Specification of Ruthenium Dyes

Ru (II) derivatives; [Ru(bpy)₂(4-dihexylmethyl-4'-heptyl-2,2'-bipyridine)](PF₆)₂ (CS91) and [Ru(bpy)₂(4,4'-bis(3-ethylheptyl)-2,2'-bipyridine)](PF₆)₂ (CS93) were shown in Figure 2.1.

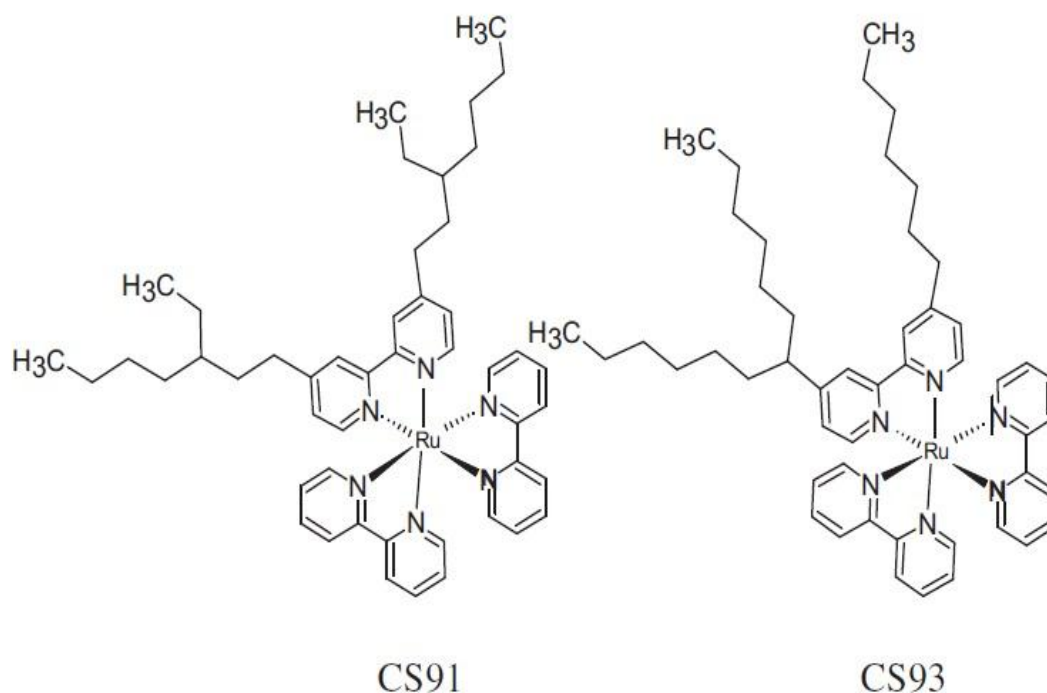


Figure 2.1 Structures of the exploited dyes [Ru(bpy)₂(4-dihexylmethyl-4'-heptyl-2,2'-bipyridine)](PF₆)₂ (CS91) and [Ru(bpy)₂(4,4'-bis(3-ethylheptyl)-2,2'-bipyridine)](PF₆)₂ (CS93) (Oner, Sahin, & Varlikli, 2012).

[Ru(bpy)₂(L₁)](PF₆)₂ (CS91);

Melting point: 136°C.

FTIR (KBr, cm⁻¹): 2956, 2926, 2859 (C-H), 1614, 1538, 1420, 1375 (bpy).

¹H NMR (DMSO-d₆) δ ppm: 8.82 (d, J = 8.2 Hz, 4H), 8.75 (s, 2H), 8.15 (t, J = 7.6 Hz, 4H), 7.70 (d, J = 5.2 Hz, 4H), 7.52 (m, 6H), 7.38 (d, J = 4.9 Hz, 2H), 2.74 (t, J = 8.1 Hz, 4H), 1.58 (m, 4H), 1.24 (m, 18H), 0.82 (m, 12H).

¹⁹F NMR (Acetone-d₆) δ ppm: -68.6(d, ¹J_{P-F} = 708 Hz).

³¹P NMR (Acetone-d₆) δ ppm: 78.9 (sept., ¹J_{P-F} = 708 Hz).

ESI-MS (m/z) [M-PF₆]⁺ 967.36, [M-2PF₆]²⁺ 411.20.

Elemental distribution calculated for $C_{48}H_{60}N_6P_2F_{12}Ru$: C, 51.84%; H, 5.44%; N, 7.56%, and found: C, 51.81%; H, 5.38%; N, 7.60%.

$[Ru(bpy)_2(L_2)](PF_6)_2$ (CS93);

FTIR (KBr, cm^{-1}): 2926, 2855 (C-H), 1614, 1540, 1422, 1376 (bpy).

1H NMR (DMSO- d_6) δ ppm: 8.82 (m, 5H), 8.71 (s, 1H), 8.15 (m, 4H), 7.70 (d, 4H), 7.52 (m, 6H), 7.35 (t, 2H), 2.75 (m, 3H), 1.64 (m, 6H), 1.22 (m, 24H), 0.80 (m, 9H).

^{19}F NMR (Acetone- d_6) δ ppm: -68.6 (d, $^1J_{P-F}$ = 708 Hz).

^{31}P NMR (Acetone- d_6) δ ppm: 78.9 (sept., $^1J_{P-F}$ = 708 Hz).

ESI-MS (m/z) $[M-PF_6]^{+}$ 995.39, $[M-2PF_6]^{2+}$ 425.21.

Elemental distribution calculated for $C_{50}H_{64}N_6P_2F_{12}Ru$: C, 52.68%; H, 5.66%; N, 7.37%, and found: C, 52.78%; H, 5.65%; N, 7.42% (Oner, Sahin, & Varlikli, 2012).

2.3 Fabrication of Silver Nanoparticles

Colloidal silver nanoparticles were synthesized according to the literature method (Solomon et al., 2007). A large excess of sodium borohydride was used to reduce the ionic silver and to keep the silver nanoparticles apart from each other in a coordinated form with the anions of BH_4^- . A 10 mL volume of 1.0 mM silver nitrate was added dropwise into the 30mL of 2.0 mM sodium borohydride solution in an ice bath under magnetic stirring. Color of the colloidal solution turned pale yellow after addition of the 2mL of silver nitrate and following purple and finally gray color when all of the silver nitrate had been added (See Figure 2.2). The 6000 RPM centrifuge (6000 RPM) method was used to separate the silver nanoparticles dispersed in water for size distribution analysis.

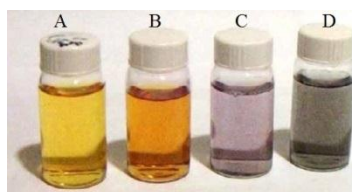


Figure 2.2 Colloidal silver in various stages of aggregation, (A) clear yellow sol, (B) dark yellow sol, (C) violet sol, and (D) grayish sol, as aggregation proceeds (Solomon et al., 2007).

2.3.1 Characterization of Silver Nanoparticles

Average size distribution results of Ag nanoparticles have been recorded as 84.6 nm (%100). The plasmon resonance of the produced metallic silver (while in form of yellow sol) yielded an absorption peak near 400 nm which corresponds to the particle size of 50–70 nm. Phase composition and crystallinity characteristics of the synthesized AgNPs were investigated by using X-ray diffractometer (see Figure 2.4). The X-ray diffraction patterns correspond to silver with a crystalline face centered-cubic (fcc) structure without any impurity. In order to determine the chemical environment as well as the oxidation state of Ag NPs, we also performed XPS measurements at the Ag 3d core levels (see Figure 2.5). The Ag 3d_{5/2} core level binding energy for the synthesized particles appeared at 367.57 which are in good agreement with binding energy of bulk metallic silver as shown earlier (Ozturk, et al., 2014). Size distribution results of the fabricated AgNPs were shown in Figure 2.3.

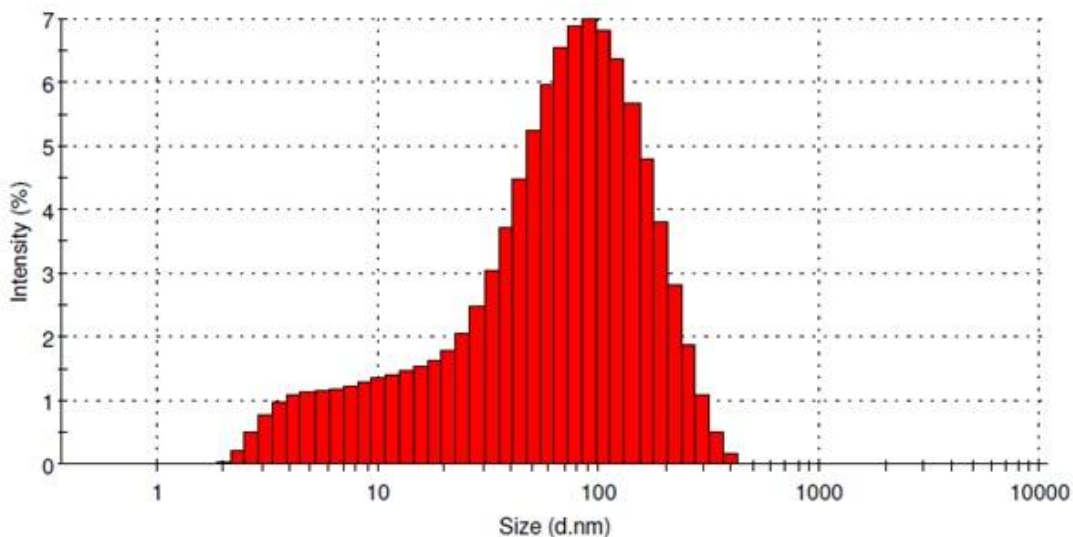


Figure 2.3 Size distribution analysis results of the fabricated AgNPs.

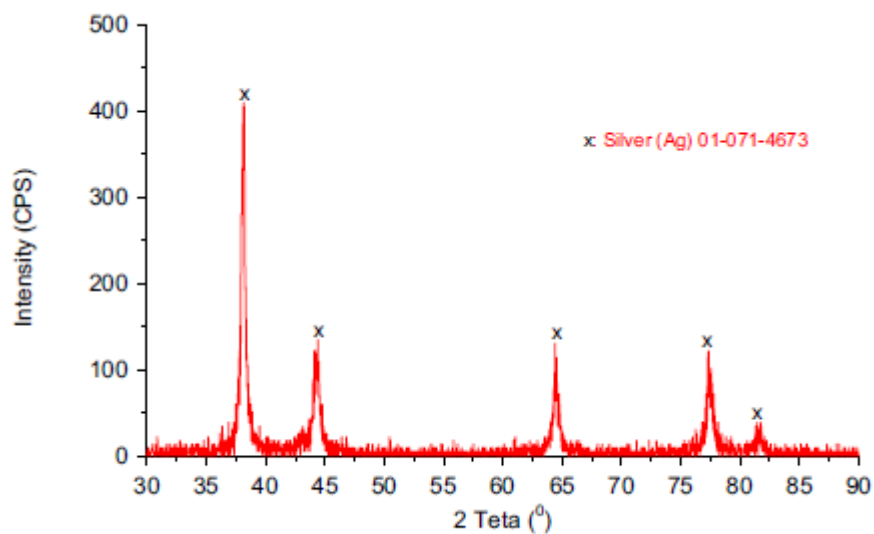


Figure 2.4 X-ray diffraction of synthesized silver nanoparticles.

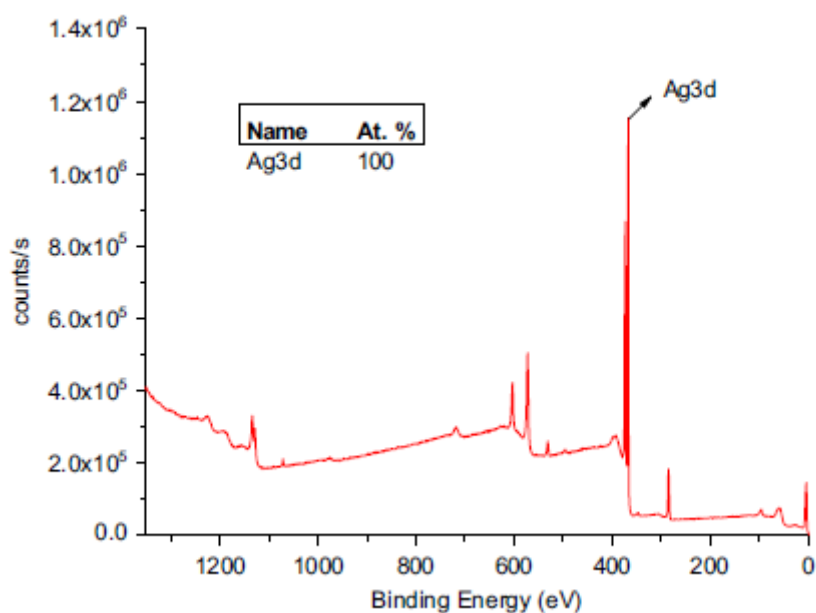


Figure 2.5 Ag 3d XPS spectra of Ag nanoparticles on ITO substrates.

2.3.2 Plasmon Absorption of Silver Nanoparticles

The specific colors of the colloidal silver solutions shown in Figure 2.2 are due to the Plasmon absorbance of the silver nanoparticles. Incident light creates oscillations in conduction electrons on the surface of the silver nanoparticles and electromagnetic

radiation is absorbed. The wavelength of the plasmon absorption maximum of the silver nanoparticles in solvent moiety can be used to estimate the particle size (Solomon et al., 2007). Here the Plasmon resonance of the produced metallic silver in different sizes was given in Figure 2.6.

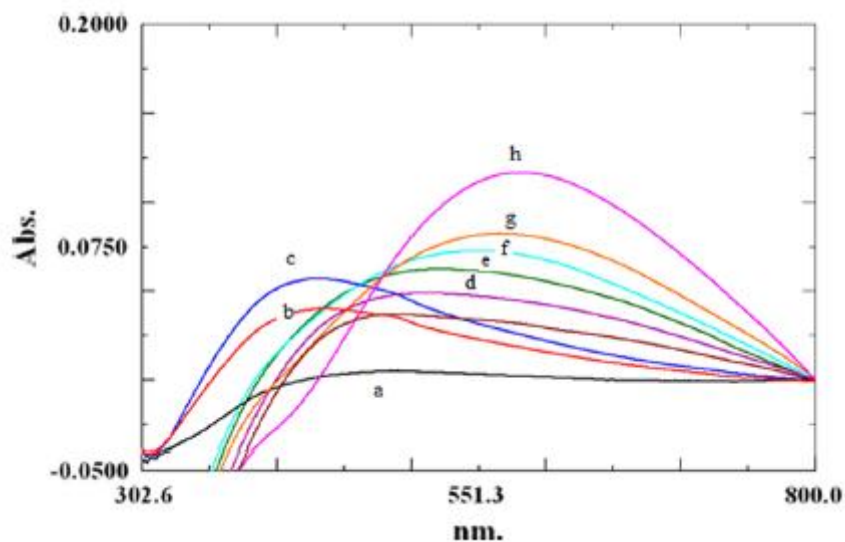


Figure 2.6 The UV–Vis absorption spectra of the different size of AgNPs during production. a: in the beginning of formation of AgNPs, b and c: particle diameter around 70 nm, d, e, f, g and h: average particle diameter at 100, 170, 240-1000 nm. B and c correspond to yellow sol and g and h correspond to grey sol (Ozturk, et al., 2014).

2.4 Fabrication of Thin Films

We referred the sensing composites as cocktails. The cocktails were prepared in 25 mL of glass vials. Silicon or poly(TMSP), plasticizer, perfluorochemical, ionic liquid, silver nanoparticles and the Ru dye were dissolved in tetrahydrofuran (THF). The cocktails were mixed under magnetic stirring to provide homogeneity at 20.00°C. The resulting composites were spread onto a 125 μm polyester support (Mylar TM type) by knife coating technique or exposed to high voltage for electrospinning. Compositions of the exploited sensing agents were shown in Table 2.1.

Table 2.1 Compositions of the exploited sensing agents

Matrix	Additives			
	Ionic liquid (mg)	Perfluro compound (mg)	AgNPs (mg)	Dye
poly(TMSP)	24	5	-	4 mg CS91
poly(TMSP)	24	5	2	4 mg CS91
poly(TMSP)	24	5	-	4 mg CS93
poly(TMSP)	24	5	2	4 mg CS93
silicon	24	5	-	4 mg CS91
silicon	24	5	2	4 mg CS91
silicon	24	5	-	4 mg CS93
silicon	24	5	2	4 mg CS93

2.5 Fabrication of Electrospun Nanofibers

2.5.1 Electrospinning Apparatus

A programmable syringe pump (Top Syringe Pump Top-5300) and a high voltage power supply (Gamma High Voltage ES30) were used together for fabrication of electrospun fibers. Figure 2.7 reveals the components of the electrospinning apparatus.

The homogeneous poly(TMSP) and/or silicon solutions were placed in a 10 mL plastic syringe fitted with a metallic needle of 0.4 mm of inner diameter. The syringe is fixed vertically on the syringe pump (Top Syringe Pump Top-5300) and the electrode of the high voltage power supply (Gamma High Voltage ES30) was clamped to the metal needle tip. The feed rate of the cocktail was 2.0 mL/h; the applied voltage was 28 kV. The electrospun fibers were collected on the surface of the aluminum foil.

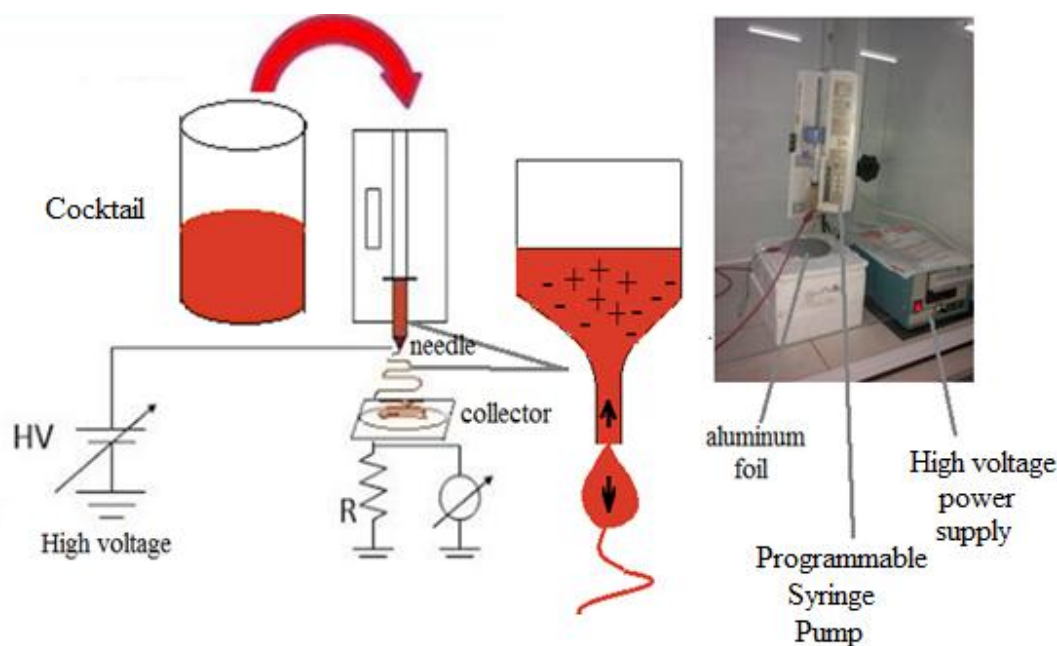


Figure 2.7 The most frequently used electrospinning set-up.

2.6 Instruments

2.6.1 Spectrophotometer and Spectrofluorometer Apparatus

The absorption spectra of the solutions and sensor films were recorded by using a Shimadzu 1801 UV-Visible (Japan) spectrophotometer. The steady state fluorescence measurements of the solutions, sensor films and fibers were recorded by using Varian Cary Eclipse and Edinburgh Instruments Spectrofluorometers. Fluorescence lifetimes were measured by time resolved fluorescence spectrometer of Edinburgh Instruments of FLS920 which works on the principle of time correlated single photon counting (TCSPC) method (see Figure 2.8). The samples were excited with microsecond flash lamp. The excitation and emission slits were set to 5 nm. During measurements, the Instrument Response Function (IRF) was obtained from a non-fluorescing suspension of a colloidal silica (LUDOX 30%, Sigma Aldrich) in water, held in 10mm path length quartz cell and was considered to be wavelength independent. The lifetime parameters were recovered by iterative convolution (reconvolution) with a weighted, nonlinear least-squares method using the measured IRF and emission decay data. The reduced chi-square values and plots of weighted

residuals were used to determine the ‘goodness of fit’ between the calculated and measured decay curves. In all cases the calculated chi square values (χ^2) were less than 1.2 and the residuals trace symmetrically distributed around the zero axes.

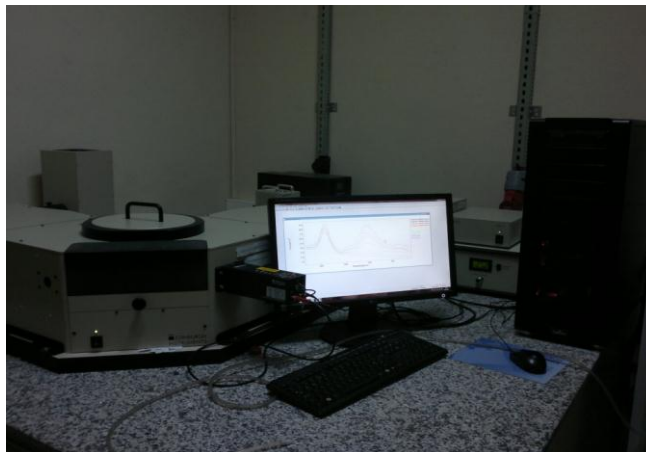


Figure 2.8 Time resolved fluorescence spectrometer of Edinburg Instruments of FLS920.

2.6.2 Gas Blender

Oxygen and nitrogen gases were mixed in the concentration range of 0–100% in a gas diluter (Sonimix 7000A gas blending system) (see Figure 2.9). The total pressure was maintained at 760 Torr (1 Torr = 133.322 Pa). The output flow rate of the gas mixture was maintained at 550 mL.min⁻¹. Gas mixtures were introduced into the sensing agent containing cuvette via a diffuser needle under ambient conditions.



Figure 2.9 Gas blender and oxygen and nitrogen gases.

2.6.3 Particle Size Distribution Analyzer

Size distribution analysis of the silver nanoparticles was performed with a Zeta sizer instrument in dispersed form in triethanolamine (Malvern Instruments Ltd.).

2.6.4 X-Ray Diffractometer

X ray diffraction patterns of the fabricated AgNPs were determined with XRD instrument from Thermo- Scientific. The diffraction patterns were recorded from 30 to 90° at a speed of 2°/min. The XPS analysis of the AgNPs was performed with Al-K α irradiation of a Thermo- Scientific instrument. The device was calibrated according to gold; 4f_{7/2}. A 10⁻⁸ mbar of vacuum was applied and 20 scans from a single point were recorded. Pass energy and energy step size values were reported as 150 eV and 1 eV, respectively.

CHAPTER THREE

OXYGEN SENSING STUDIES

3.1 Introduction

Monitoring of oxygen levels is of great importance in workplaces, environmental and biomedical analysis as well as industrial processes (Wang, & Wolfbeis, 2013). Accurate measurements of oxygen levels require development of reliable devices. Most of the optical chemical oxygen sensors work on the principle of luminescence quenching of organic dyes by gaseous or dissolved oxygen. Up to now, pyrene and its derivatives (Fujiwara, & Amao, 2003), pyrenebutyric acid, quinoline and phenanthrene (Ishiji, & Kaneko, 1995), transition metal complexes of osmium (Xu, Kneas, Demas, & DeGraff, 1996), rhenium (Sacksteder, Demas, & DeGraff, 1993; Hirao, & Fukuhara, 1998), platinum (Cywinski, et al., 2009; Wu, et al., 2010; Elosua, Hernaez, Matias, & Arregui, 2015), iridium and palladium (Borisov, et al., 2009; Toro, et al., 2010; Chu, & Chuang, 2015), polypyridine complexes of ruthenium (Roche, et al., 2010; Estella, et al., 2010; Jorge, et al., 2008; Wu, Song, Li, & Liu, 2010; Zhang, Lei, Mai, & Liua, 2011; Wang, et al., 2008; Zhang, Li, Lei, & Li, 2008), and metalloporphyrins have been used as oxygen sensitive molecular probes (Gulino, et al. 2006). Covalently assembled monolayer of 61-(p-hydroxyphenyl-methano) fullerene molecules (Gulino, et al., 2005), platinum (II) complexes of tetrakis(pentafluorophenyl)porphyrin (Frecher, Borisov, Zhdanov, Klimant, & Papkovsky, 2011) and octaethylporphine (PtOEP) with two other reference dyes have been used for very low concentrations of oxygen (Wang, et al., 2012). In another study micro- and nanoparticles of TiO₂ and microparticles of different materials have been used to investigate the phenomena underlying the role of matrix materials on optrode performance along with platinum-tetra-fluoro-phenyl-porphyrin (PtTFPP) (Chanti, Maier, & Porterfield, 2009). A combination of core-shell silica nanoparticles and platinum (II) meso-tetrakis (pentafluorophenyl) porphyrin (PtTFPP) was used to measure dissolved oxygen concentrations in the range of 0–40 mg/L (Chu, & Lo, 2010). Among them, the ruthenium (II) polypyridine complexes have been the most intensively utilized dye. They produce metal-to-ligand

charge transfer (MLCT) excited states which are readily quenched by oxygen. Additionally, their spectral response to oxygen in sol-gel and silicon based matrices is well understood. However, most of them suffer from nonlinear calibration plots within the measured oxygen concentrations, instabilities of the signal intensities, or from leaching in wet moieties (Roche, et al., 2010; Wu, Song, Li, & Liu, 2010; Zhang, Lei, Mai, & Liua, 2011). A short summary of the published ruthenium based oxygen sensors in terms of sensitivities, working ranges, response times, detection limits and long and/or short term photostability was given in Table 3.1. The matrix material plays an important role in the stability and sensitivity of the sensor. The oxygen-permeability directly influences the sensitivity. On the other hand, the host/dye compatibility is another important issue and poor compatibility may result in dye aggregate formation on either the micro- or nano-scale. Dye aggregates are not visible and can be detectable with spectroscopic techniques. Depending on the selected polymer, the ruthenium complexes possess moderate to high photostabilities. In this work, silicon and poly(1-trimethylsilyl-1-propyne) (poly(TMSP)) were chosen due to excellent oxygen solubilities, resistant characteristics to water and harsh conditions, protecting abilities of the indicator dyes from alterations providing an appropriate micro environment for them, and, tailoring abilities on electrospinning conditions. On the other hand, it is known that presence of the conducting metallic species like gold and silver is effective on emissive spectral properties of nearby fluorophores. The excited fluorophores may transfer their energy to the surface plasmon of proximal metal surfaces or particles, which subsequently reradiate and may facilitate the detection ability of the molecular probe. In this work, we utilized the silver nanoparticles (AgNPs) along with ionic liquid as additives for fabrication of polymeric oxygen sensitive mesoporous structures and electrospun nanofibers. The two amphiphilic red emitting ruthenium complexes that contain symmetric and asymmetric branched alkyl chains on their bipyridyl (bpy) ligands have been used for the first time. The ruthenium dyes of $[\text{Ru}(\text{bpy})_2(4\text{-dihexylmethyl-4'-heptyl-2,2'-bipyridine})](\text{PF}_6)_2$ (CS91) and $[\text{Ru}(\text{bpy})_2(4,4'\text{-bis(3-ethylheptyl)-2,2'-bipyridine})](\text{PF}_6)_2$ (CS93) were synthesized in our labs according to the literature information (Oner, Sahin, & Varlikli, 2012). The presence of branched alkyl groups on the bpy ligand is expected to increase the

compatibility of the dyes with the silicon matrix. In contrast to the water-soluble $[\text{Ru}(\text{bpy})_3]^{2+}$ complexes, the offered dyes were not subject of leaching in water or in flow systems.

Table 3.1 A short summary of the Ru based O₂ sensing studies. (NR: not reported, Ref.: Reference)

Sensitive dye/ measured parameter	Matrix materials	Sensitivity	Dynamic working range/ working range	Detection limit/ response time	Stability	Ref.
Ruthenium (4,7-diphenyl-1,10-phenanthroline) ₃ Cl ₂	trimethoxysilane (TEOS) xerogel	sensitivity (I ₀ /I per % O ₂) 5% O ₂ 0.0064 (on gold), 0.0013 (on glass); 50% O ₂ 0.00011 (on gold), 0.00015 (on glass)	0-30% [O ₂]	0.16% O ₂ for the sensor on glass, and 0.033% for the gold coated slide t _{90%} to be 1.06±0.62 s for the gold coated slide and 4.97±1.75 s for the sensor on glass	NR	(Roche, et al., 2010)
[Ruthenium(II)-tris(4,7-diphenyl-1,10-phenanthroline)] dichloride	fluorinated and non-fluorinated ORMOSILS, 3,3,3-trifluoropropyltrimethoxysilane (TFP-TMOS)	K _{SV} ([O ₂ %] ⁻¹) 0.208 ± 0.003 for PTEOS/TFP-TMOS 0.204 ± 0.002 for ETEOS/TFP-TMOS	0-100 % [O ₂] and 0-5 % [O ₂]	0.002% and 0.003% oxygen for non-fluorinated and fluorinated matrices.	was monitored for 7 months 24% and 27% signal drift after 1 week of storage	(Estella, et al., 2010)

Table 3.1 A short summary of the Ru based O₂ sensing studies. (NR: not reported, Ref.: Reference) (cont.)

[Ru(II)-tris(4,7-diphenyl-1,10-phenanthroline)] ²⁺	Sol-gel matrix and core-shell CdSe-ZnS semiconductor nanocrystals	I_0/I [O ₂] 0.0080 I_{Ru} [T] -0.032 S_{QD} [T] 0.0068	0-100 % [O ₂] and 0-30 % [O ₂]	0.1% [O ₂] (Reported LOD for previous work exploiting the same composite)	Enhanced photostability with respect to hydrolytic sol-gels. There are no long-term studies reported.	(Jorge, et al., 2008)
[Ru(Bphen) ₂ bpy] ²⁺ (Bphen=4,7-diphenyl-1,10-phenanthroline, bpy=2,20-bipyridyl)	covalently grafted to the backbones of the ordered functionalized mesoporous MCM-41	downward Stern-Volmer plots Lehrer model K_{SV1} ([O ₂ %] ⁻¹) 0.9655±0.1240	Effectively works on 0-10 % [O ₂]	Response time is 1.2 s, the recovery time is about 29 s	NR	(Wu, Song, Li, & Liu, 2010)

Table 3.1 A short summary of the Ru based O₂ sensing studies. (NR: not reported, Ref.: Reference) (cont.)

[Ru(Phen) ₂ Phen-Si] ²⁺ (Phen = 1,10-phenanthroline, Phen-Si = 2-[4- <i>l</i> -3-(triethoxysilyl)propyl]phenyl) imidazo [4,5- <i>f</i>]-1,10-phenanthroline)	covalently grafted to the backbones of the ordered functionalized mesoporous MSU-3	I ₀ /I ₁₀₀ Ru/MSU-3 4.95 Ru-MSU-3 9.80	0-100 % [O ₂]	Ru/MSU-3 response; 7.5 s, recovery; 20.5 s Ru-MSU-3 response; 5.6 s, recovery; 20.2 s	Short time stability was tested for 3200 s.	(Zhang, Lei, Mai, & Liua, 2011)
[Ru ₃ (bpy) ₆ (TMMB)] ⁶⁺ (1) and [Ru ₃ (phen) ₆ (TMMB)] ⁶⁺ (2) (bpy ¼ 2,20-bipyridine, phen ¼ 1,10-phenanthroline, TMMB ¼ 1,3,5-tris [2-(20-pyridyl)benzimidazolyl]methylbenzene)	two mesoporous silicate (MS) matrices.	I ₀ /I 3.17, 5.39, 3.21, 5.00	0-100% [O ₂]	Response/recovery (s); 2.85/ 26.6 2.38/33.25 3.32/25.65 2.40/28.50	NR	(Wang, et al., 2008)
[Ru(bpy) ₂ (Bpy-Si)] ²⁺	covalently grafted to the backbones of the ordered functionalized mesoporous MSU-3	I ₀ /I recorded at different temp. (A) 10°C, (B) 45°C and (C) 65°C 7.1, 2.3, and 2.13	0-100% [O ₂]	Response 3s, recovery 21s at 10°C	The improvement of photostability under light irradiation has been reported	(Zhang, Li, Lei, & Li, 2008)

Table 3.1 A short summary of the Ru based O₂ sensing studies. (NR: not reported, Ref.: Reference) (cont.)

tris(2,2'-bipyridyl)ruthenium(II)chloride (Ru(bipy) ₃ ²⁺)	polymethyl methacrylate and ethyl cellulose with ionic liquids/electrospun nanofibers	1.19 × 10 ⁻² (% ⁻¹) and 8.1 × 10 ⁻³ (% ⁻¹)	0-100% [O ₂]	Response 4s, recovery 22s	long term stability more than 3 years.	(Oner, Sahin, & Varlikli, 2012)
4,7-diphenyl-1,10-phenanthroline Ligand and RuCl ₃ .3H ₂ O	tetraethoxysilane (TEOS) and tetramethoxysilane (TMOS).	K _{sv} (Pa ⁻¹) TEOS R =2, 6.47x10 ⁻⁵ TEOS R = 4, 5.02x10 ⁻⁵ MTEOS R = 2 , 7.8x10 ⁻¹³ MTEOS R =4, 5.9x10 ⁻¹³ Water: precursor ratio (R)	NR	t ₉₀ (x10 ⁻³) s TEOS R =2, 40 TEOS R = 4, 462 MTEOS R = 2, 4.9 MTEOS R =4, 4.9	NR	(Mc Donagh, Bowe, Mongey, & MacCraith , 2002)

Table 3.1 A short summary of the Ru based O₂ sensing studies. (NR: not reported, Ref.: Reference) (cont..)

tris(2,2'-bipyridyl)ruthenium (II) chloride (Ru(bipy) ₃ ²⁺)	acid-catalyzed tetraethyl ortho silicate (TEOS) based sol-gel matrix and 1-ethyl-3-methylimidazolium tetrafluoroborate (EMIMBF ₄)	K _{sv} values for 3 different sols; 0.0027, 0.0072 and 0.0710	0.0–100% pO ₂ Excellent linearity	response and regeneration times were 5 and 10 s.	NR	(Williams, Winfield, & Miller, 1983)
[Ru(bpy) ₂ (4-dihexylmethyl-4'-heptyl-2,2'-bipyridine)](PF ₆) ₂ (CS91) and [Ru(bpy) ₂ (4,4'-bis(3-ethylheptyl)-2,2'-bipyridine)](PF ₆) ₂ (CS93)	poly(1-trimethylsilyl-1-propyne) (poly(TMSP)) and silicon	K _{sv} ; CS91 in silicon: 0.0151 CS93 in silicon: 0.0150 CS91 in poly(TMSP): 0.011 CS93 in poly(TMSP): 0.0095	0-100% [O ₂]	For Ag-free matrices: 3-12 s For Ag containing matrices: 4-15 s	Long term stability; more than 8 months, short term stability; excellent, no leaching after 10 measurements.	This work

3.2 Spectral Characterization of Fluoroionophore

3.2.1 Absorption Spectra Related Characteristic

Absorption spectra of CS91 and CS93 were recorded in THF, silicon and in poly(TMSP), both in the absence and presence of silver nanoparticles. Figure 3.1 and 3.2 reveal the absorption spectra of the dyes recorded in THF. The absorption spectrum of the CS91 exhibited two maxima at 286 and 456 nm. The CS93 exhibited similar behavior in THF and the two absorption maxima appeared at 281 and 455 nm, respectively (see Figure 3.1 and 3.2). Figures 3.3 and 3.4 reveal absorption spectra of the dyes in solid matrices of silicon and poly(TMSP) both in the absence and presence of AgNPs. Absorption maxima of the Ag-free CS91 dye appeared at 459 and 461 nm in silicon and poly(TMSP), respectively. High molar extinction coefficients accompanied to the absorption bands observed around 460 nm. These broad absorption bands centered around 460 nm can be assigned to MLCT. However, when AgNPs were added into the matrix the absorption maxima exhibited 27 nm and 30 nm of blue-shift in poly(TMSP) and silicon, respectively. The reported blue-shift can be attributed to plasmon absorption of the AgNPs competing with the absorption of the Ru dye. The absorption spectra related characteristics of the dyes were shown in Table 3.2.

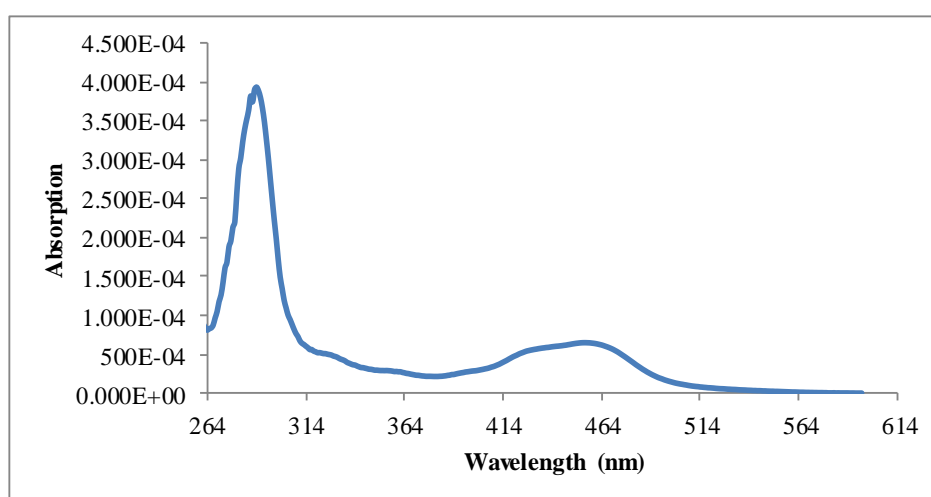


Figure 3.1 Absorption spectrum of CS91 dye in THF.

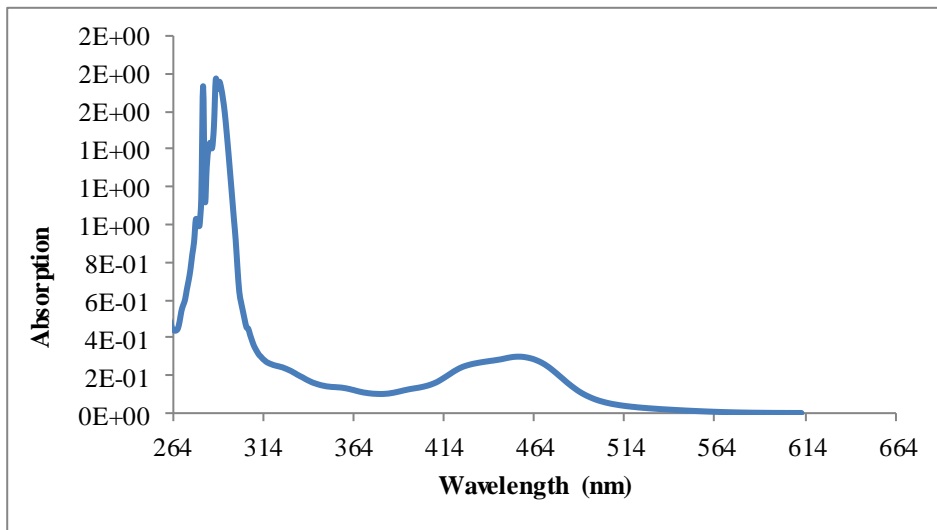


Figure 3.2 Absorption spectrum of CS93 dye in THF.

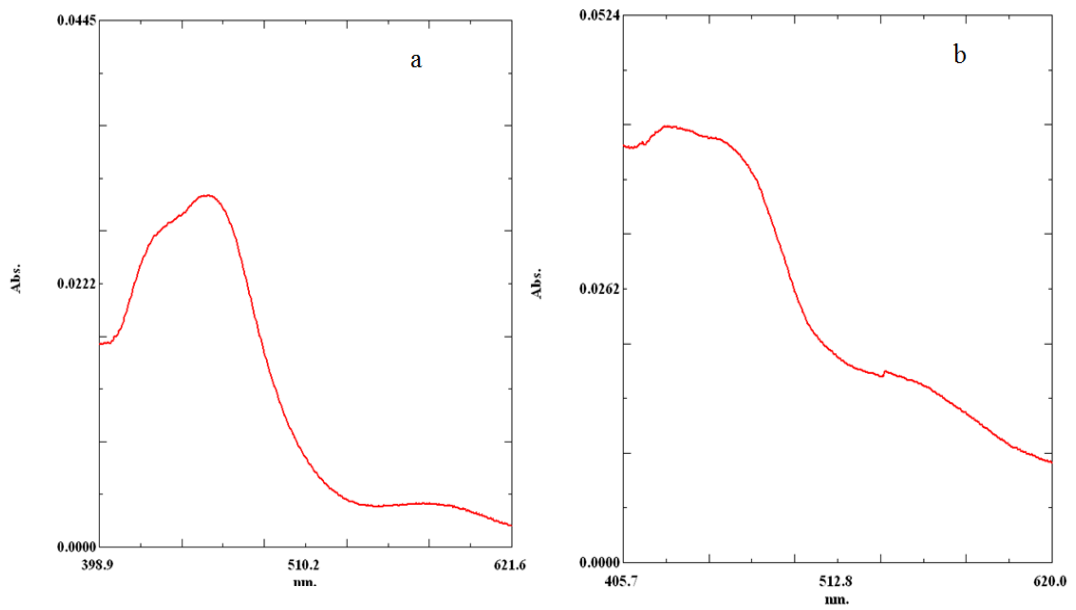


Figure 3.3 Absorption spectrum of poly(TMSP) embedded CS91 in the absence (a) and the presence (b) of AgNPs.

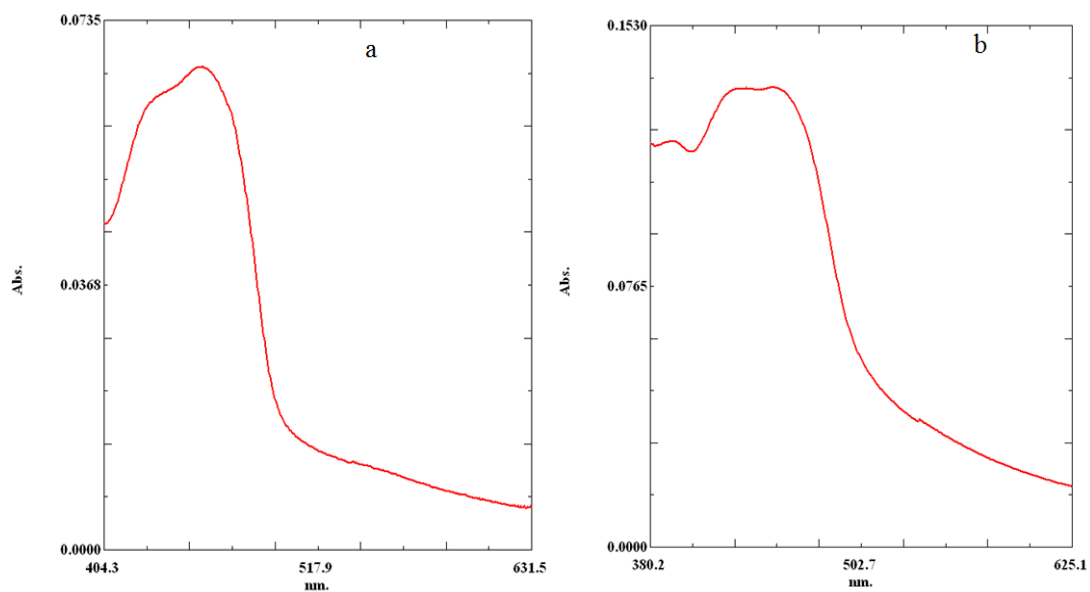


Figure 3.4 Absorption spectrum of silicon embedded CS93 in the absence (a) and the presence (b) of AgNPs.

Table 3.2 The absorption spectra related characteristics of the dyes in different moieties.

Dye	Matrix	Nano silver	$\lambda_{\max 1}, \lambda_{\max 2}$ (nm)	ϵ_1, ϵ_2 (molar extinction coefficient) ($L \times cm^{-1} \times mol^{-1}$)
CS91	poly(TMSP)	-	457, 570	70 000, 2 000
CS91	poly(TMSP)	+	430	40 000
CS93	poly(TMSP)	-	456	60 000
CS93	poly(TMSP)	+	442	130 000
CS91	silicon	-	459	91 000
CS91	silicon	+	427, 460	82 000, 1 100
CS93	silicon	-	460, 540	52 000, 4 000
CS93	silicon	+	460	83 000
CS91	THF	-	456	90 000
CS93	THF	-	455	100 000

3.2.2 Emission Spectra Related Characteristic

Excitation and emission spectra of the CS91 and CS93 were recorded in THF. Figure 3.5 and 3.6 reveal the excitation and emission spectra of the dyes recorded in THF. In all cases we excited the dye at 450 nm. The dyes exhibited emission maxima

at 625 nm in THF. The emission spectra of the exploited dyes were recorded in silicon and poly(TMSP), both in the absence and presence of silver nanoparticles. The emission spectrum of the CS91 exhibited maxima at 632 and 630 nm in silicon and poly(TMSP), respectively. The CS93 exhibited similar behavior in emission wavelength in all of the exploited moieties. Table 3.3 shows emission spectra related characteristics of the dyes in all of the exploited moieties in the presence and absence of the AgNPs. The Stoke's Shifts were extracted from excitation-emission data and were shown in Table 3.3. Not only in the THF but also in solid phases the dyes exhibited high Stoke's Shifts ranging between 175-184 nm.

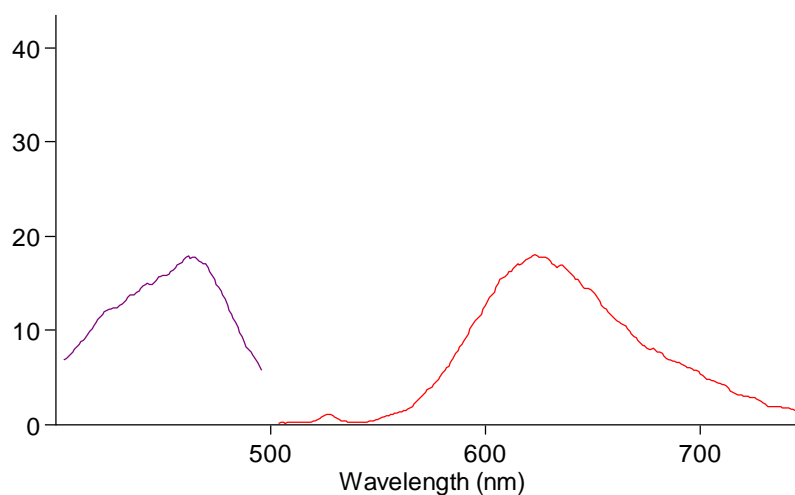


Figure 3.5 Excitation and emission spectrum of CS91 dye in THF.

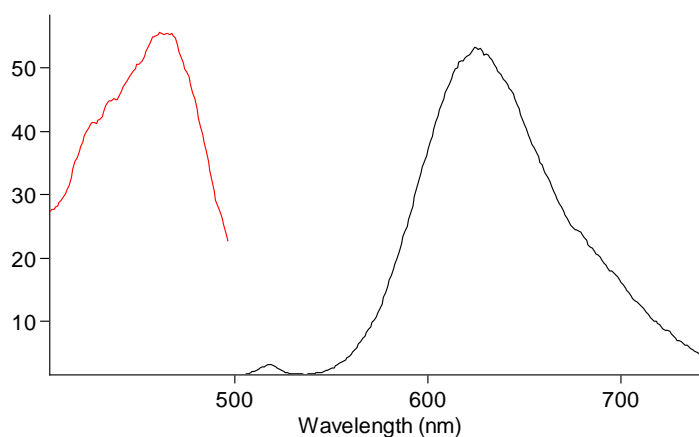


Figure 3.6 Excitation and emission spectrum of CS91 dye in THF.

Table 3.3 Fluorescence spectra related characteristics of the CS91 and CS93 in poly(TMSP), silicon and in THF.

Dye	Matrix	Thin film/ nanofiber	Nano silver (mg)	$\lambda_{\max}^{\text{ex}}$ (nm)	$\lambda_{\max}^{\text{em}}$ (nm)	Stoke's shift ($\Delta\lambda$) (nm)	Quantum yield (ϕ_F)
CS91	poly(TMSP)	TF	-	450	630	180	
CS91	poly(TMSP)	NF	-	450	632	182	
CS91	poly(TMSP)	TF	+	450	634	184	
CS91	poly(TMSP)	NF	+	450	634	184	
CS93	poly(TMSP)	TF	-	450	632	182	
CS93	poly(TMSP)	NF	-	450	638	188	
CS93	poly(TMSP)	TF	+	450	632	182	
CS93	poly(TMSP)	NF	+	450	632	182	
CS91	silicon	TF	-	450	632	182	0.58
CS91	silicon	NF	-	450	628	178	
CS91	silicon	TF	+	450	634	184	0.87
CS91	silicon	NF	+	450	632	182	
CS93	silicon	TF	-	450	632	182	
CS93	silicon	NF	-	450	628	178	
CS93	silicon	TF	+	450	630	180	0.78
CS93	silicon	NF	+	450	628	178	
CS91	THF	-	-	450	625	175	0.43
CS93	THF	-	-	450	625	175	0.46

3.2.3 Quantum Yield Calculations

Fluorescence quantum yield values, (ϕ_F) were calculated employing comparative William's method (Williams, Winfield, & Miller, 1983). Alkaline solution of 8-Hydroxypyrene-1,3,6-Trisulfonic Acid, Trisodium Salt (HPTS) in water was used as reference standard whose fluorescence quantum yield is $\phi_F = 0.75$.

For this purpose, absorbance and emission spectra of five different concentrations of reference standard and the employed CS91 and CS93 dyes were recorded. The integrated fluorescence intensities were plotted vs. absorbance for reference and employed dyes respectively. The ratio of the gradients of the plots is proportional

to the quantum yield. Equation 3.1 was used to calculate fluorescence quantum yields (φ_F). In the following Equation 3.1 ST and X are denote standard and sample, respectively, and also Grad and n are the gradient of the plot and refractive index of the solvent or polymer matrix material, respectively. Figures 3.7 and 3.8 show absorbance vs integrated fluorescent intensity plots of the CS91, CS93 in THF and silicon matrix in the absence and presence of AgNPs and HPTS in alkaline solution.

$$\varphi_F = \varphi_{ST} \left(\frac{\text{Grad}_X}{\text{Grad}_{ST}} \right) \left(\frac{n_X^2}{n_{ST}^2} \right) \quad (3.1)$$

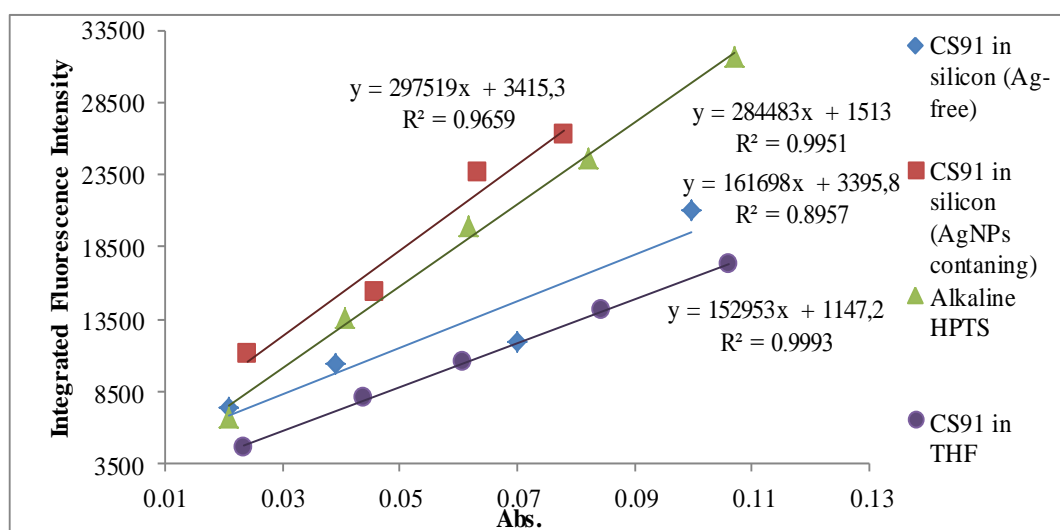


Figure 3.7 The integrated fluorescence intensities vs absorbance values of HPTS in alkaline solution, CS91 in THF and silicon matrix in the absence and presence of AgNPs.

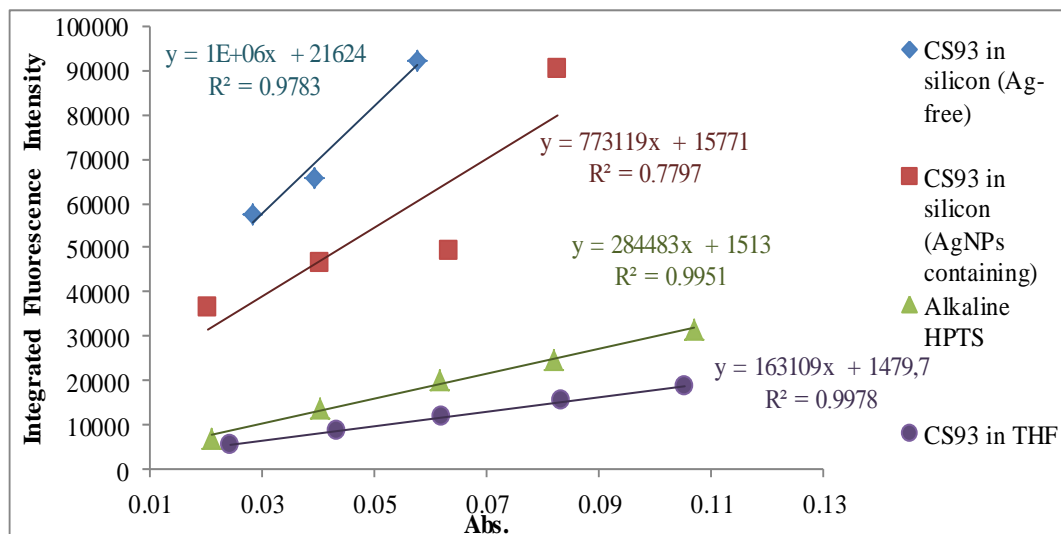


Figure 3.8 The integrated fluorescence intensities vs absorbance values of HPTS in alkaline solution, CS93 in THF and silicon matrix in the absence and presence of AgNPs.

Quantum yield calculations were performed in THF and silicon matrices for Ag-free and Ag containing forms. ϕ_F values of 0.43 and 0.46 were found to be for CS91 and CS93 in THF, respectively. The CS91 exhibited Φ_F value of 0.87 in the presence of AgNPs when embedded in silicon in form of thin film. The Ag-free composite of CS91 yielded an ϕ_F value of 0.58. Presence of AgNPs enhanced the quantum yield 1.5 fold with respect to the Ag-free forms. Table 3.3 reveals the calculated ϕ_F values for the tested moieties.

3.2.4 SEM Images of Electrospun Membranes

The surface morphologies of the fibers and films were studied using scanning electron microscope (SEM) instrument (FEI QUANTA FEG 250). The fibers and porous surfaces fabricated exploiting the simple electrospinning technique; were characterized with SEM photographs. While Ag containing cocktails resulting in a porous structure, the Ag-free ones were in fiber forms. The SEM images of electrospun membranes of different compositions at various magnifications were shown in Figure 3.9.

While the silver containing cocktails were resulting with porous structures, the Ag-free ones were in fiber forms. To our opinion, the high voltage extending to

28000 V distinctly affected dielectric properties of the polymer in the presence of the silver nanoparticles with respect to the Ag-free structures and therefore inhibited formation of the continuous fibers.

In cases of porous structures and fiber forms, the empty spaces of the holes within the structures allow satisfactory diffusion of O₂. It was observed that the Ag-free electrospun membranes made up of both, silicon and poly(TMSP) exhibited 3D network structure with a random fiber orientation. The diameters of the poly(TMSP) based fibers were around 450 nm. Usage of the silicon based matrix resulted in thicker fiber structures with average diameters of 4 μm. This type of fibrous-structure of the electrospun membrane provides higher surface area than that of continuous thin films. Production of nano-scale fibers and further increase of the surface area may be achieved by changing conditions of the electrospinning process such as solvent composition, viscosity, concentration, temperature, humidity and working distance, which results in either smaller diameter fibers or increased porosity at the fiber surface (Ozturk, et al., 2014).

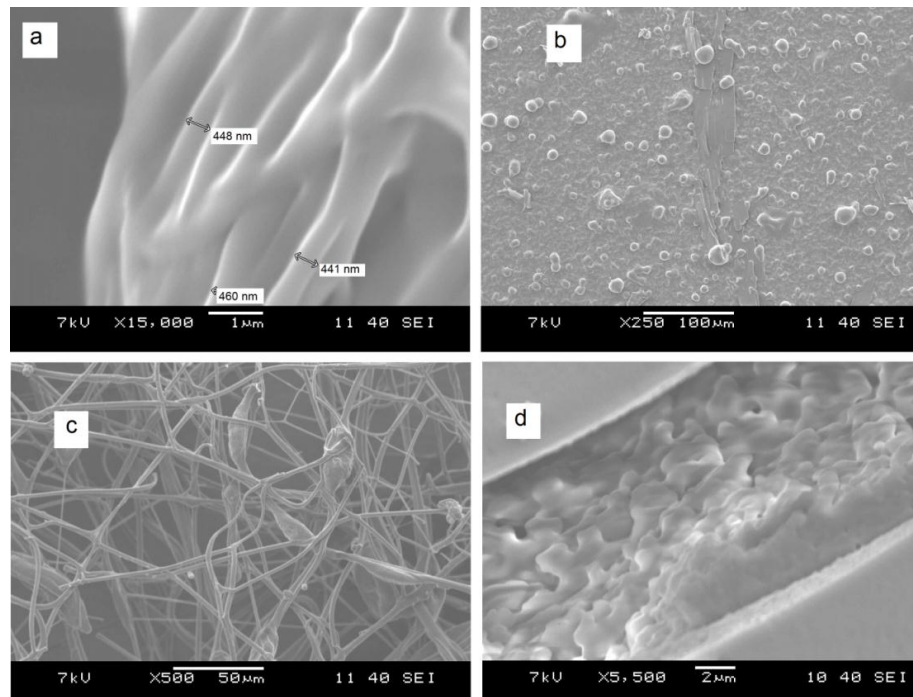


Figure 3. 9 SEM photographs of electrospun nanofibers, micro fibers and mesoporous structures under different magnifications. (a): the CS93 embedded in Ag-free poly(TMSP), (b): Ag containing poly(TMSP), (c): Ag-free silicon, (d): Ag containing silicon.

3.3 Oxygen Sensing Studies

3.3.1 Oxygen Sensing Studies in Clean Air

Oxygen induced spectral responses of CS91 and CS93 in silicon and poly(TMSP) were recorded for increasing concentrations of oxygen between 0.0-100.0 %. The oxygen sensitivity tests were performed for thin film and nanofiber forms of CS91 and CS93 both in the absence and presence of the AgNPs. Experimental results were shown between Figure 3.10- 3.25 As expected, in all cases the composites exhibited quenching behavior after exposure to oxygen. The quenching of the excited state luminescence intensity of the dyes by oxygen molecules was monitored at 630 nm.

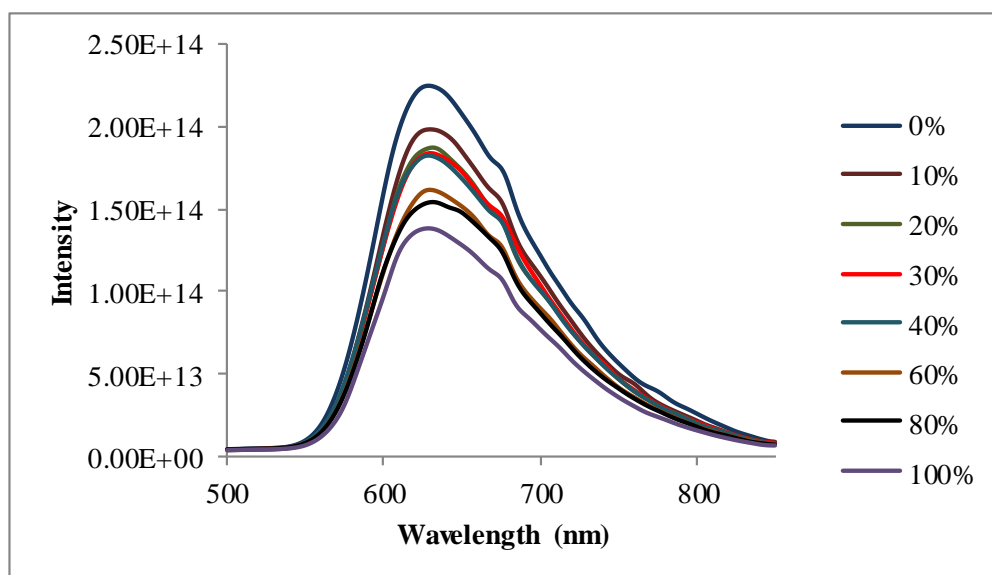


Figure 3.10 Oxygen responses of the thin film of the CS91 dye in poly(TMSP) matrix. Oxygen concentrations were shown in graphic for all results respectively.

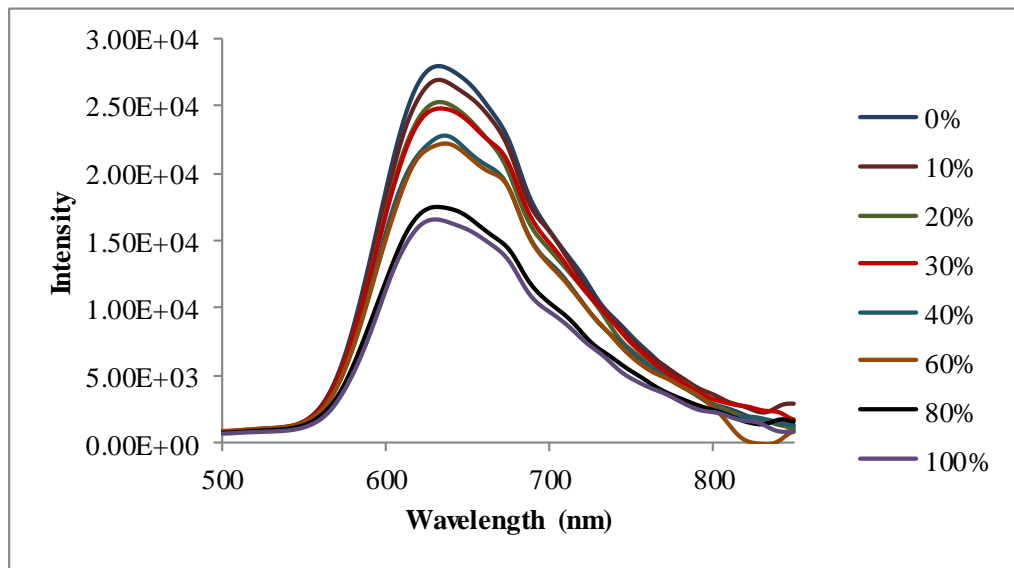


Figure 3.11 Oxygen responses of the AgNPs including thin film of the CS91 dye in poly(TMSP) matrix. Oxygen concentrations were shown in graphic for all results respectively.

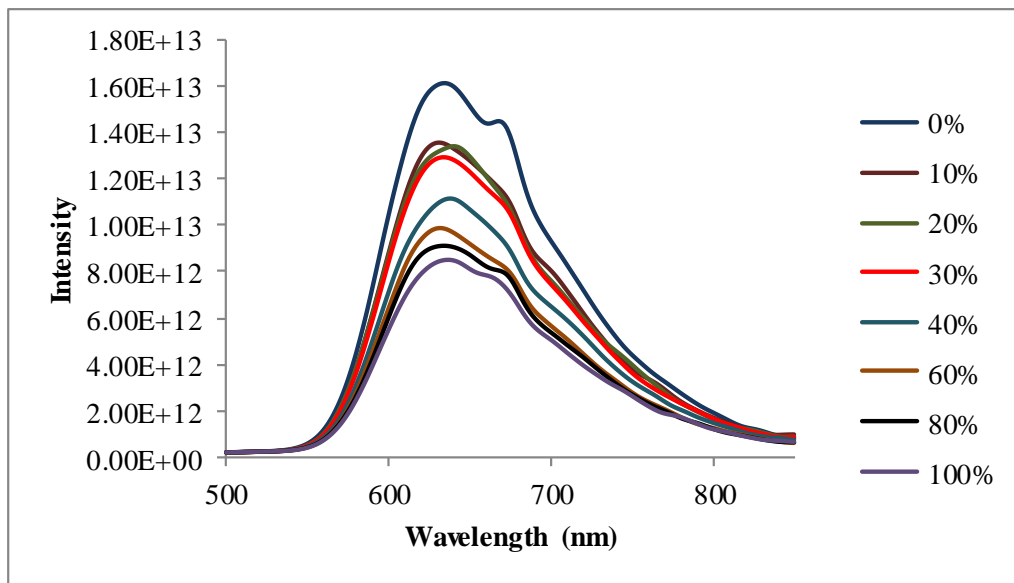


Figure 3.12 Oxygen responses of the nanofibers of the CS91 dye in poly(TMSP) matrix. Oxygen concentrations were shown in graphic for all results respectively.

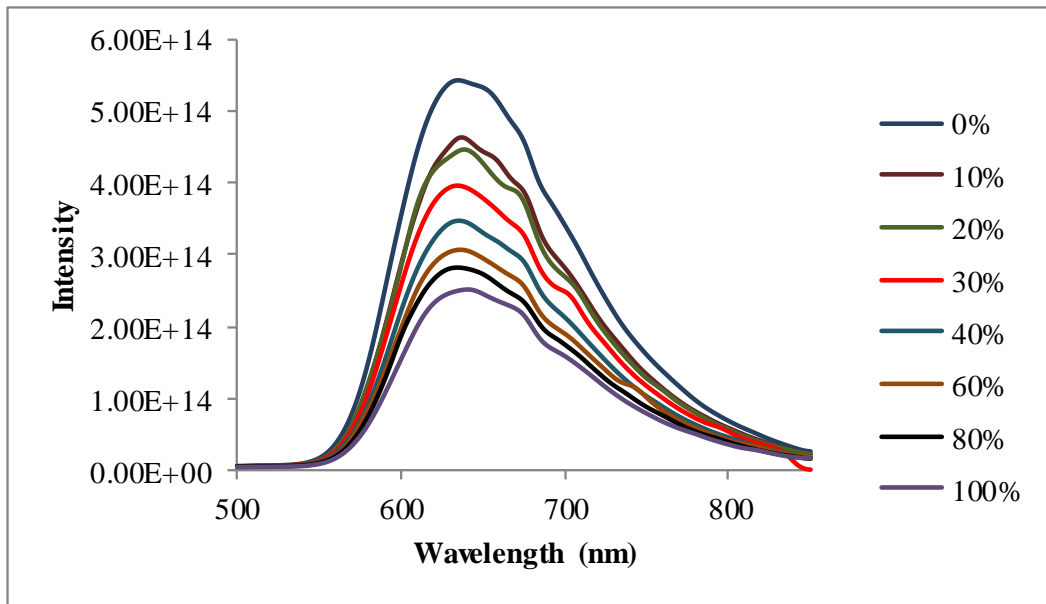


Figure 3.13 Oxygen responses of the AgNPs including nanofibers of the CS91 dye in poly(TMSP) matrix. Oxygen concentrations were shown in graphic for all results respectively.

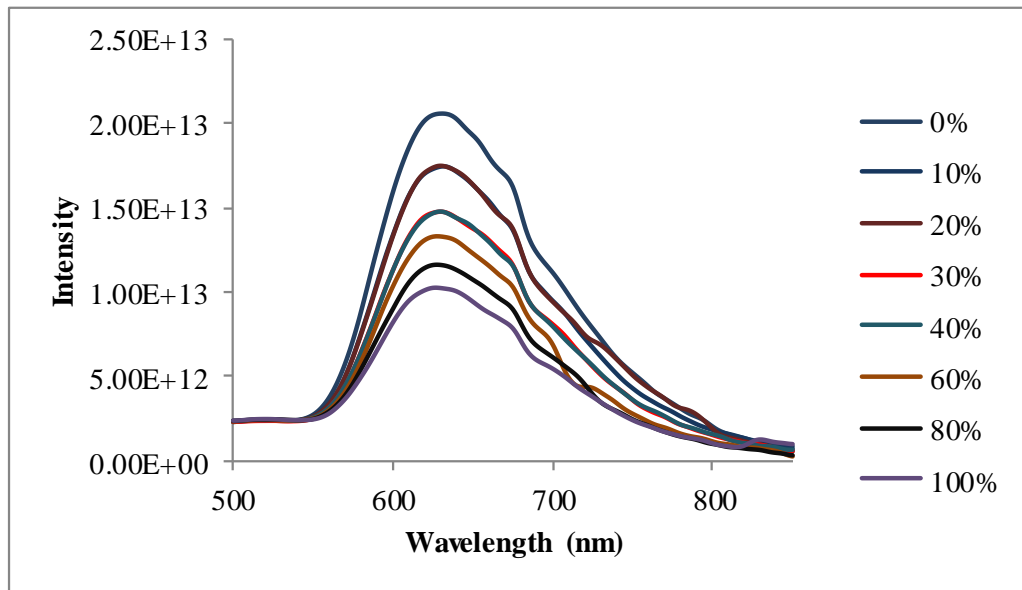


Figure 3.14 Oxygen responses of the thin film of the CS91 dye in silicon matrix. Oxygen concentrations were shown in graphic for all results respectively.

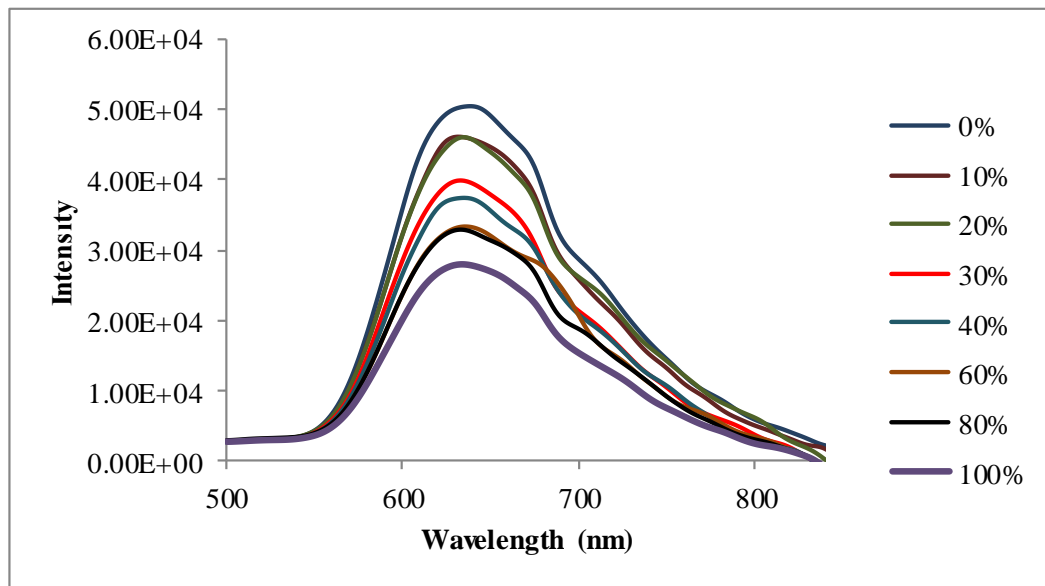


Figure 3.15 Oxygen responses of the AgNPs including thin film of the CS91 dye in silicon matrix. Oxygen concentrations were shown in graphic for all results respectively.

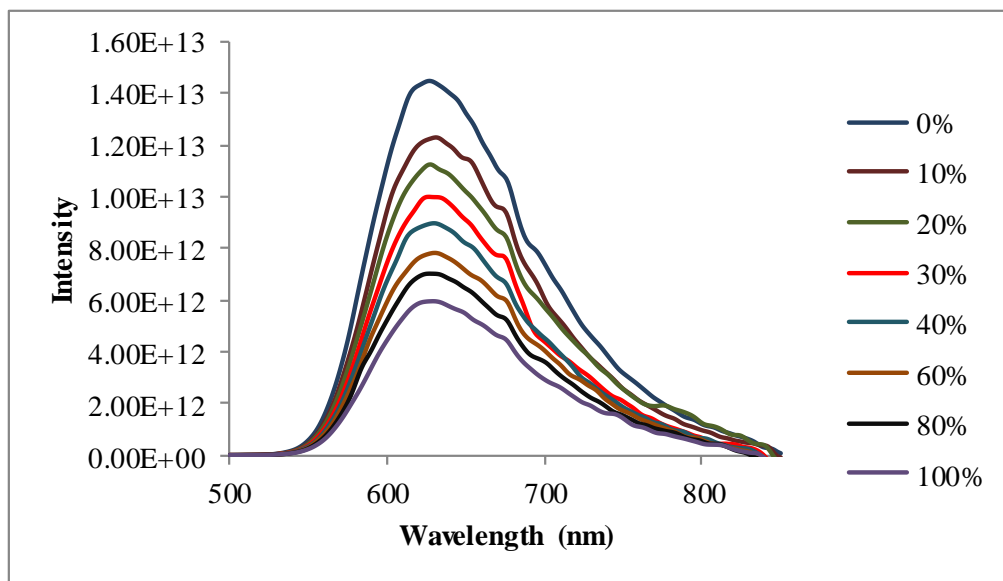


Figure 3.16 Oxygen responses of the nanofiber of the CS91 dye in silicon matrix. Oxygen concentrations were shown in graphic for all results respectively.

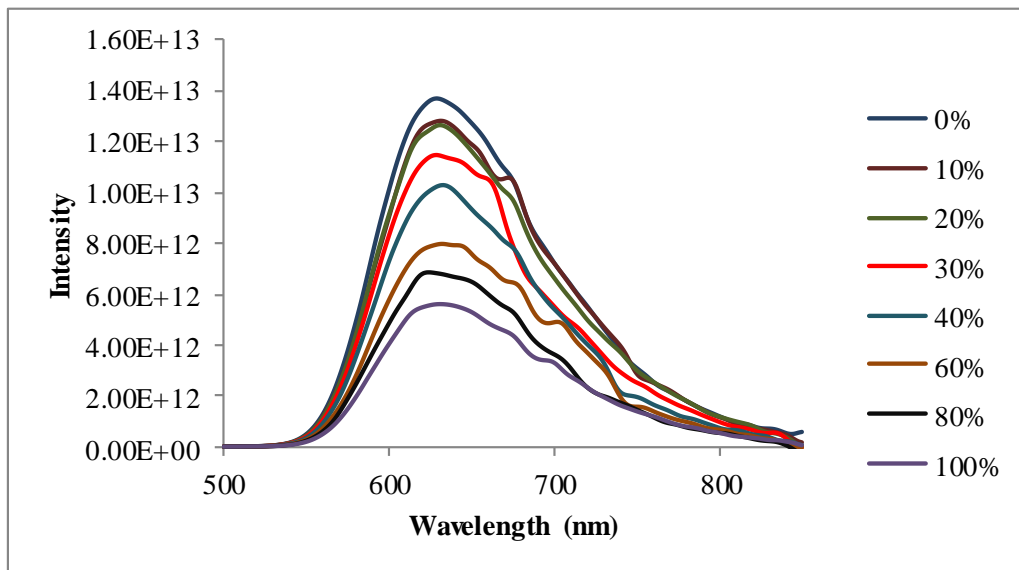


Figure 3.17 Oxygen responses of the AgNPs including nanofiber of the CS91 dye in silicon matrix. Oxygen concentrations were shown in graphic for all results respectively.

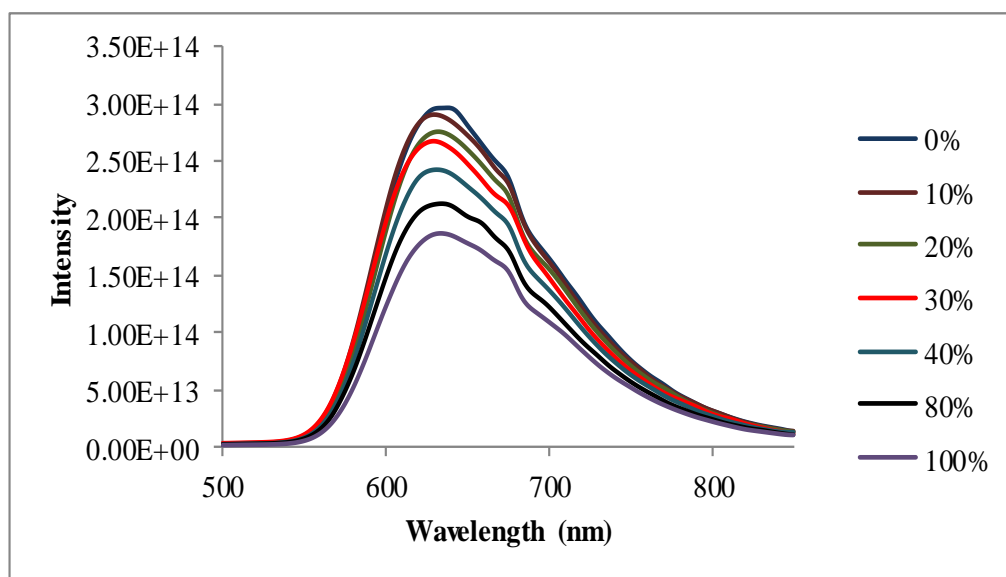


Figure 3.18 Oxygen responses of the thin film of the CS93 dye in poly(TMSP) matrix. Oxygen concentrations were shown in graphic for all results respectively.

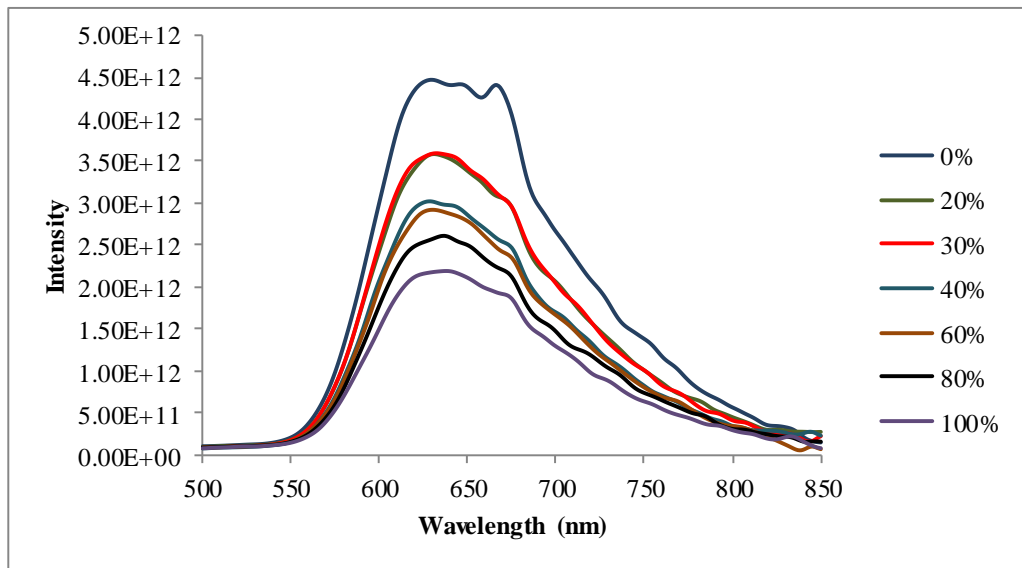


Figure 3.19 Oxygen responses of the AgNPs including thin film of the CS93 dye in poly(TMSP) matrix. Oxygen concentrations were shown in graphic for all results respectively.

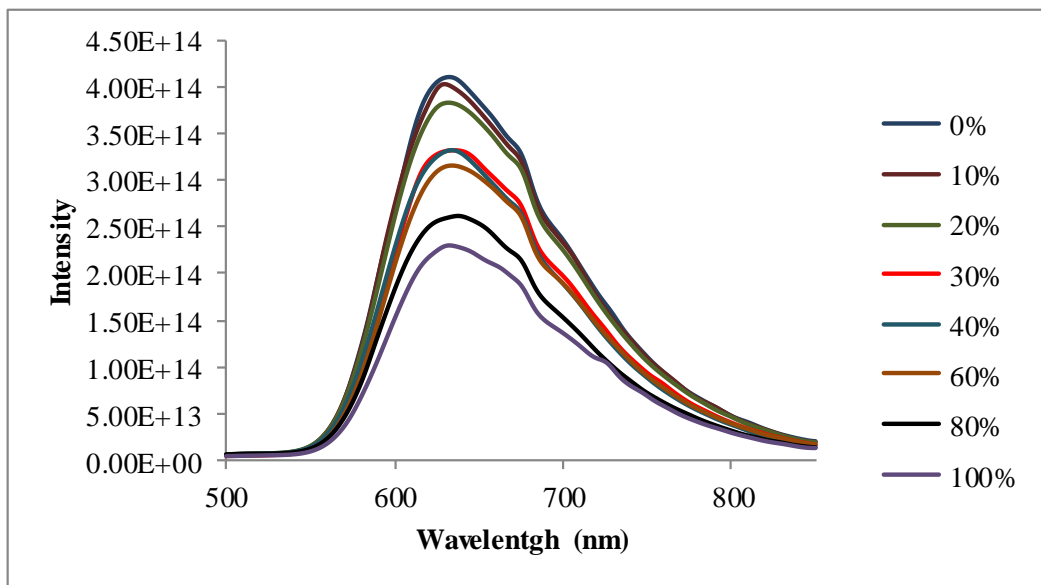


Figure 3.20 Oxygen responses of the nanofibers of the CS93 dye in poly(TMSP) matrix. Oxygen concentrations were shown in graphic for all results respectively.

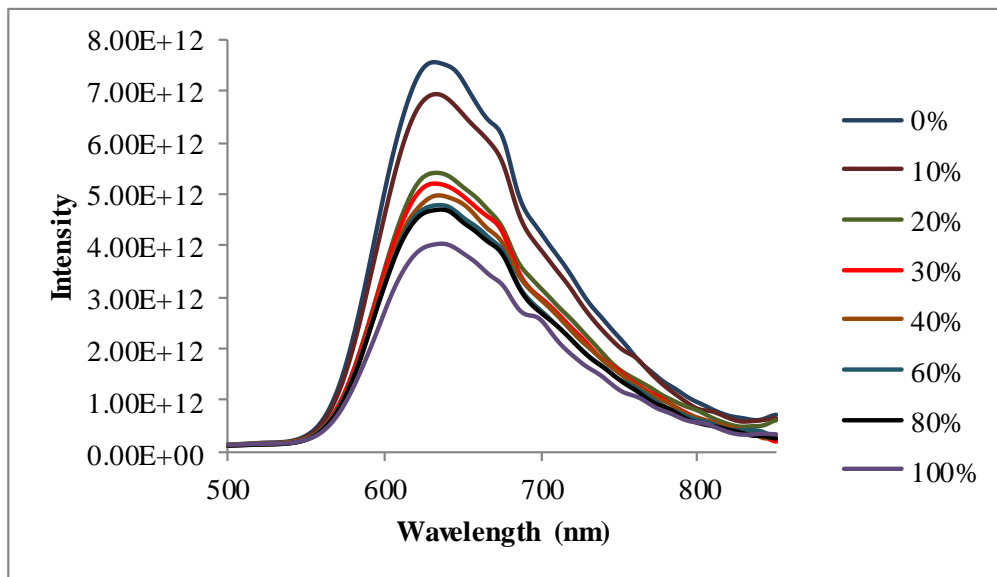


Figure 3.21 Oxygen responses of the AgNPs including nanofibers of the CS93 dye in poly(TMSP) matrix. Oxygen concentrations were shown in graphic for all results respectively.

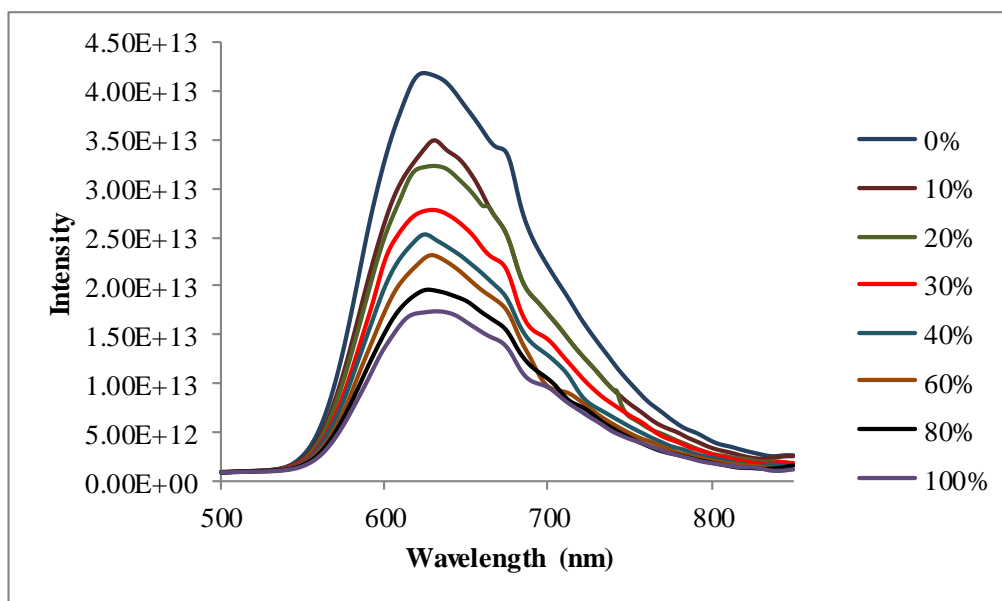


Figure 3.22 Oxygen responses of the thin film of the CS93 dye in silicon matrix. Oxygen concentrations were shown in graphic for all results respectively.

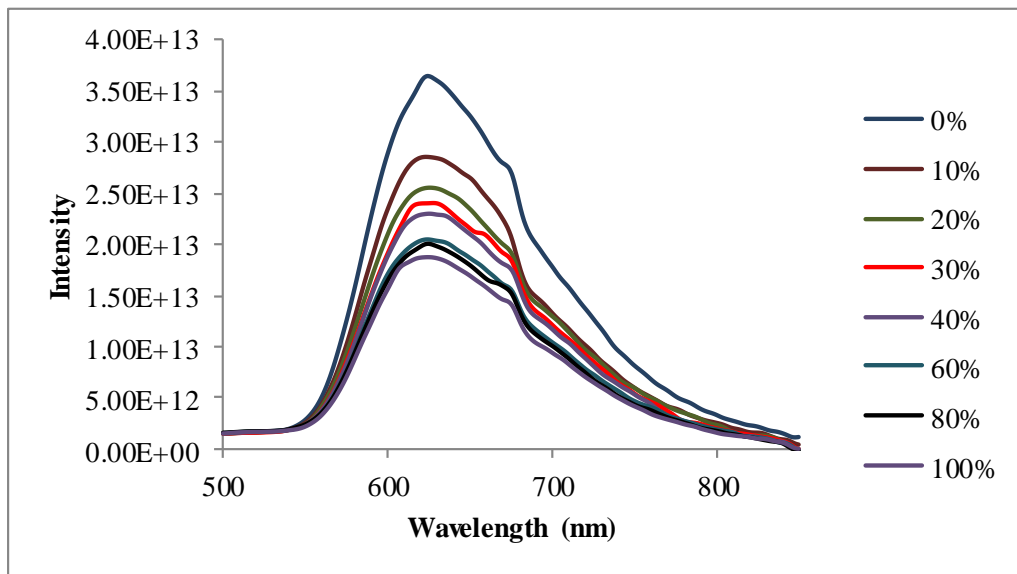


Figure 3.23 Oxygen responses of the AgNPs thin film of the CS93 dye in silicon matrix. Oxygen concentrations were shown in graphic for all results respectively.

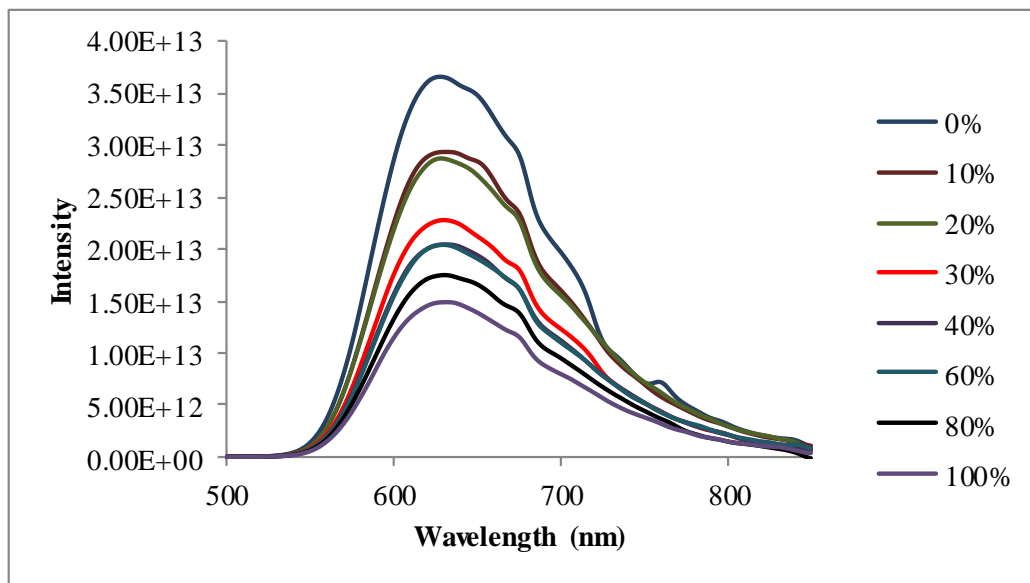


Figure 3.24 Oxygen responses of the nanofibers of the CS93 dye in silicon matrix. Oxygen concentrations were shown in graphic for all results respectively.

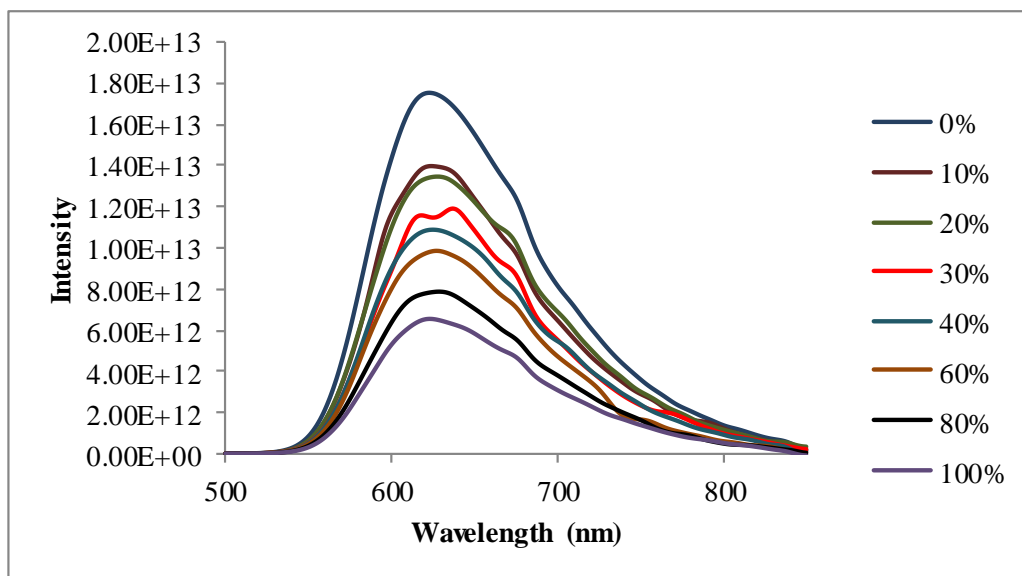


Figure 3.25 Oxygen responses of the AgNPs including nanofibers of the CS93 dye in silicon matrix. Oxygen concentrations were shown in graphic for all results respectively.

Table 3.4 reveals the overall response of each composite towards oxygen in terms of relative single change. Among them, the Ag containing CS93 embedded in silicon in form of nanofiber exhibited the highest relative signal change of 63% when exposed to oxygen. The dyes encapsulated in silicon matrices exhibited better response compared to the poly(TMSP) (see Table 3. 4). The spectral response of the dyes to oxygen has also been evaluated by Stern-Volmer analysis.

Table 3.4 Emission spectra related characteristics

Dye	Matrix	Thin film/ nanofiber	Nano silver (mg)	Response of the composites to oxygen (%)
CS91	poly(TMSP)	TF	-	38
CS91	poly(TMSP)	NF	-	48
CS91	poly(TMSP)	TF	+	38
CS91	poly(TMSP)	NF	+	54
CS93	poly(TMSP)	TF	-	37
CS93	poly(TMSP)	NF	-	44
CS93	poly(TMSP)	TF	+	52
CS93	poly(TMSP)	NF	+	47
CS91	silicon	TF	-	50
CS91	silicon	NF	-	59
CS91	silicon	TF	+	44
CS91	silicon	NF	+	59
CS93	silicon	TF	-	59
CS93	silicon	NF	-	59
CS93	silicon	TF	+	48
CS93	silicon	NF	+	63

3.3.2 Stern–Volmer Analysis of the Plots Recorded in Clean Air

The quenching of the excited state luminescence intensity of the dyes by oxygen molecules was monitored at 630 nm. Triplet oxygen is able to quench efficiently the fluorescence of ruthenium complexes via collisions with the fluorophore in its excited state leading to a non-radiative energy transfer. This effect is called “dynamic fluorescence quenching”. The degree of quenching relates to the frequency of collisions, and therefore to the concentration, pressure, temperature and matrix material of the sensor. If the luminescence quenching is purely dynamic, both, the intensity and excited state lifetimes are related to the oxygen concentration by the Stern–Volmer equation: where I_0 and I are the luminescence intensities and τ_0 and τ are decay times of the luminophore in the absence and presence of oxygen, respectively. K_{SV} is the Stern–Volmer constant, $[O_2]$ is the oxygen concentration and k_q is the quenching constant, which is related to the diffusion coefficient of oxygen throughout the matrix. For an ideal homogeneous environment, a plot of the ratio of

I_0/I or τ_0/τ versus $[O_2]$ yields a straight line with an intercept at 1 and a slope of K_{SV} , which is a measure of sensor sensitivity.

If the luminophore is distributed in heterogeneous sites in the solid matrix, the Stern–Volmer plot becomes nonlinear. In this work, the intensity based oxygen induced Stern–Volmer plots of CS91 and CS93 were produced for Ag-free and Ag containing matrices for oxygen concentrations in the range of 0.0–100.0% oxygen. Figure 3.26 and 3.27 show the gathered Stern-Volmer plots of the CS91 and CS93 in poly(TMSP) and silicon matrices, respectively. In all cases the dyes exhibited linear or linearisable calibration plots for a large concentration range of 0.0–100.0%.

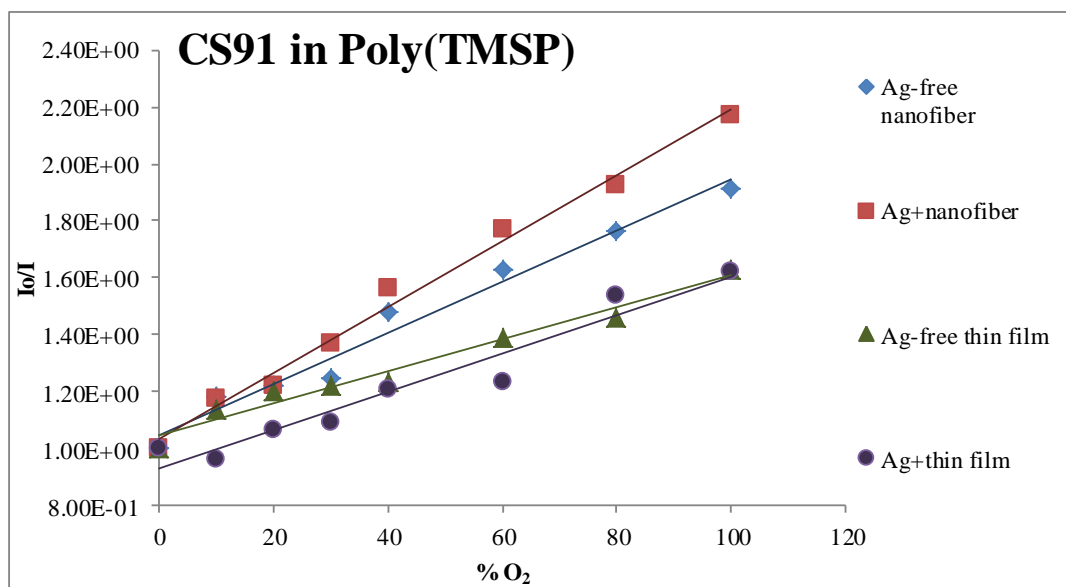


Figure 3.26 Gathered Stern-Volmer plots of nanofibers and thin films of CS91 dye in polyTMSP matrix.

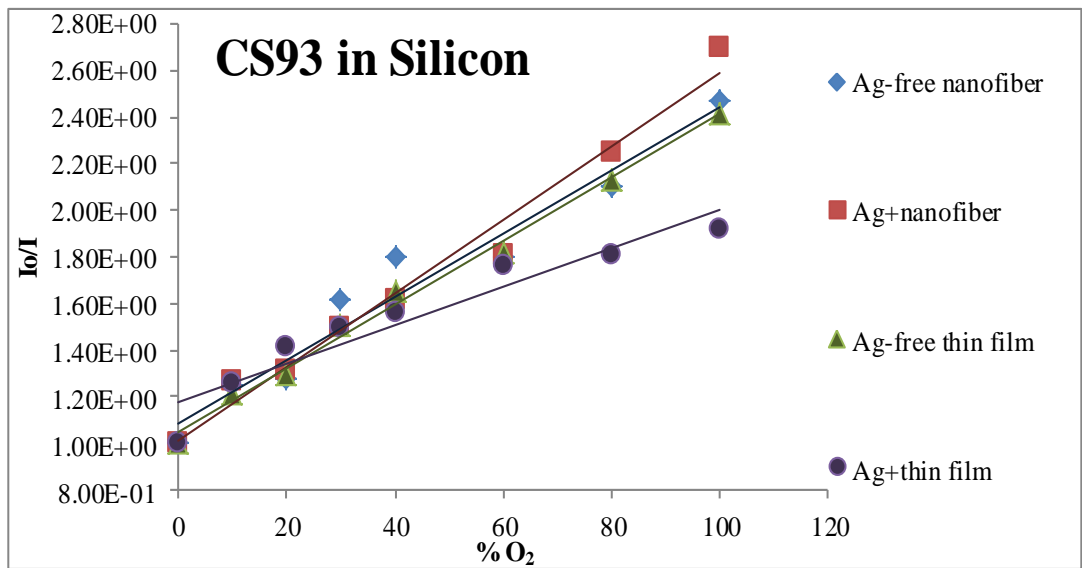


Figure 3.27 Gathered Stern-Volmer plots of nanofibers and thin films of CS93 dye in silicon matrix.

The K_{SV} values extracted from the slopes of the plots were shown in Table 3.5 for all of the exploited moieties. The; K_{SV} value is an indicator of the sensitivity. The greater the value of K_{sv} , the greater the sensitivity of the optical sensor. The Ag containing CS91 in silicon has the highest Stern- Volmer constant. The nanofiber form of Ag containing silicon embedded CS93 follows it. The regression coefficients (R^2) were also shown in Table 3.5. The best R^2 value of 0.9900 was reported for Ag containing poly(TMSP) embedded CS91 in form of nanofiber. The calibration plots of all forms of CS91 and CS93 were shown in Table 3.5.

Table 3.5 The Stern Volmer plots for clean air and contaminated conditions, oxygen induced relative signal changes, related regression coefficients and Ksv values extracted from the slopes of the plots.

Dye	Matrix	Thin film/nanofiber	Nano silver (mg)	Stern-Volmer plots (clean air)	$K_{sv}[\text{O}_2\%]^{-1}$	Regression coefficient
CS91	poly(TMSP)	TF	-	$y=0.005x+1.050$	0.0050	0.0975
CS91	poly(TMSP)	NF	-	$y=0.0087x+1.0641$	0.0087	0.9531
CS91	poly(TMSP)	TF	+	$y=0.0068x+0.9451$	0.0068	0.9736
CS91	poly(TMSP)	NF	+	$y=0.011x+1.0$	0.011	0.9900
CS93	poly(TMSP)	TF	-	$y=0.0059x+0.9559$	0.0059	0.9719
CS93	poly(TMSP)	NF	-	$y=0.0080x+0.9349$	0.0080	0.9627
CS93	poly(TMSP)	TF	+	$y=0.0095x+1.049$	0.0095	0.9714
CS93	poly(TMSP)	NF	+	$y=0.0083x+1.112$	0.0083	0.8912
CS91	silicon	TF	-	$y=0.0098x+0.9896$	0.0098	0.9962
CS91	silicon	NF	-	$y=0.0137x+1.0346$	0.0137	0.9946
CS91	silicon	TF	+	$y=0.0073x+1.0169$	0.0073	0.9754
CS91	silicon	NF	+	$y=0.0151x+0.8282$	0.0151	0.9649
CS93	silicon	TF	-	$y=0.0136x+1.0507$	0.0136	0.9921
CS93	silicon	NF	-	$y=0.013x+1.061$	0.0130	0.9740
CS93	silicon	TF	+	$y=0.0083x+1.1731$	0.0083	0.9077
CS93	silicon	NF	+	$y=0.015x+1.009$	0.0150	0.9790

3.3.3 Oxygen Sensing Studies under Volatile Organic Compounds

Oxygen sensing performance of the embedded CS91 and CS93 dyes was also tested in the presence of vapors of refinery related species, benzene, toluene, ethyl benzene, hexane and xylene. We exposed the sensor slides to the different concentrations of volatile organic vapors in a closed desiccator with an internal volume 5 L by placing 40 mL of solvent (contained in the small 50 mL beaker). The vapors were obtained via ordinary evaporation at room temperature. The mean laboratory temperature was 20°C ($\pm 0.7^\circ\text{C}$) throughout all experiments. Concentrations of the gaseous were calculated using their partial vapor pressure at 20°C considering the Raoult's law. The partial pressures were calculated in terms of percent composition for all of the volatiles and were found to be 9.89, 2.89, 1.32,

0.81, 15.97 and 9.12 mmHg for benzene, toluene, ethyl benzene, xylene and hexane, respectively. The response to oxygen was tested under given concentrations of organic vapors. Figures between 3.28- 3.43 reveal oxygen responses of the thin film and nanofiber forms of the sensing agents of CS91 and CS93 in silicon and poly(TMSP). All tests were performed both in the absence and presence of AgNPs.

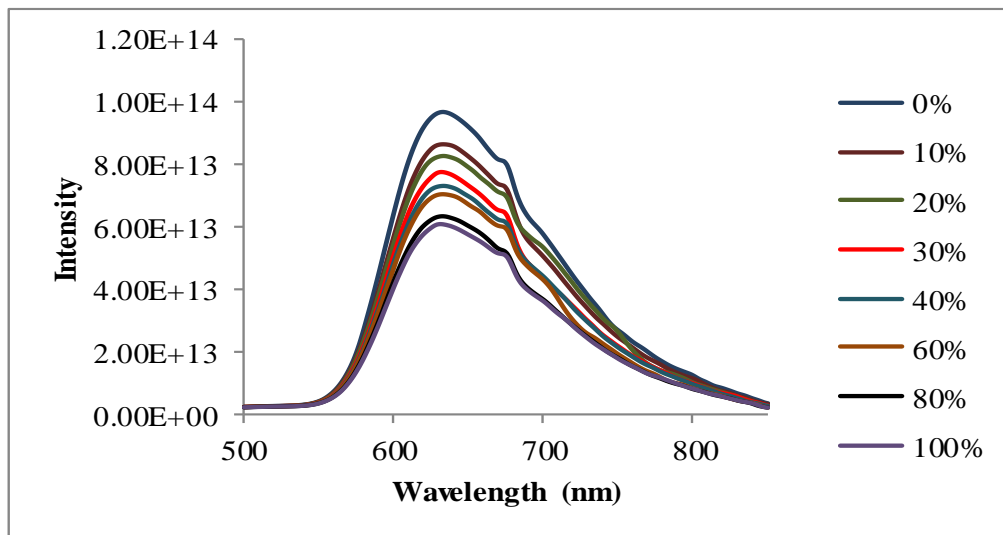


Figure 3.28 Oxygen responses of the thin film of the CS91 dye in poly(TMSP) matrix in the presence of VOCs. Oxygen concentrations were shown in graphic for all results respectively.

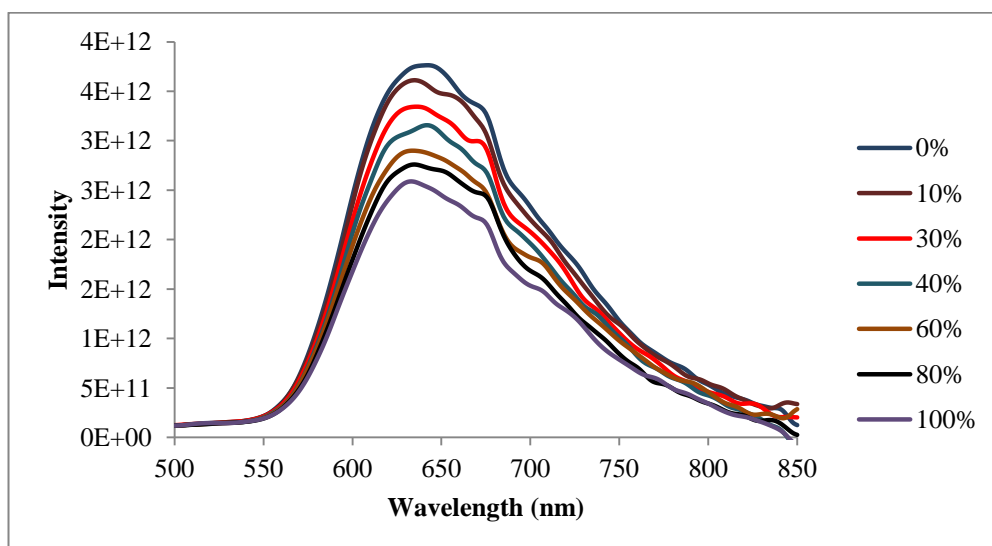


Figure 3.29 Oxygen responses of the AgNPs including thin film of the CS91 dye in poly(TMSP) matrix in the presence of VOCs. Oxygen concentrations were shown in graphic for all results respectively.

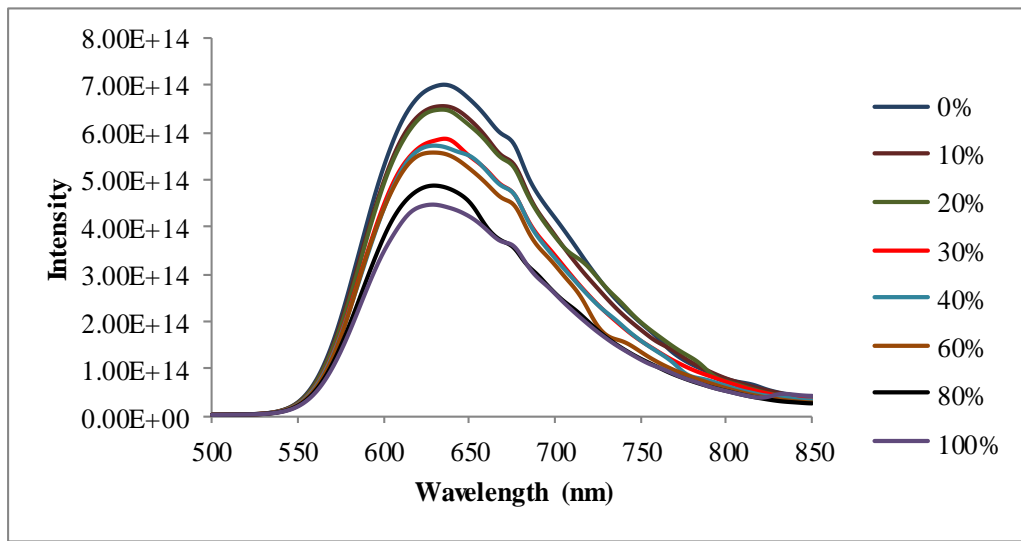


Figure 3.30 Oxygen responses of the nanofiber of the CS91 dye in poly(TMSP) matrix in the presence of VOCs. Oxygen concentrations were shown in graphic for all results respectively.

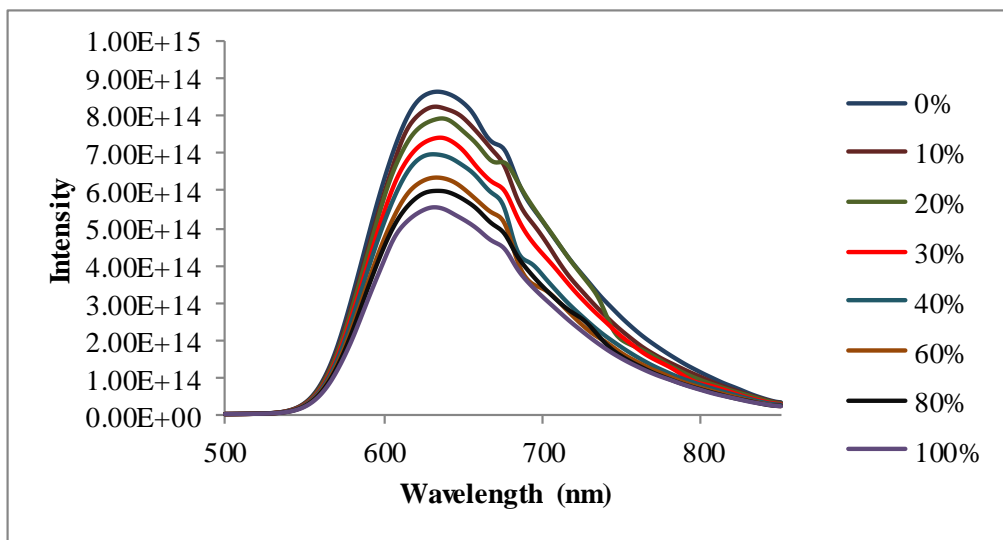


Figure 3.31 Oxygen responses of the AgNPs including nanofiber of the CS91 dye in poly(TMSP) matrix in the presence of VOCs. Oxygen concentrations were shown in graphic for all results respectively.

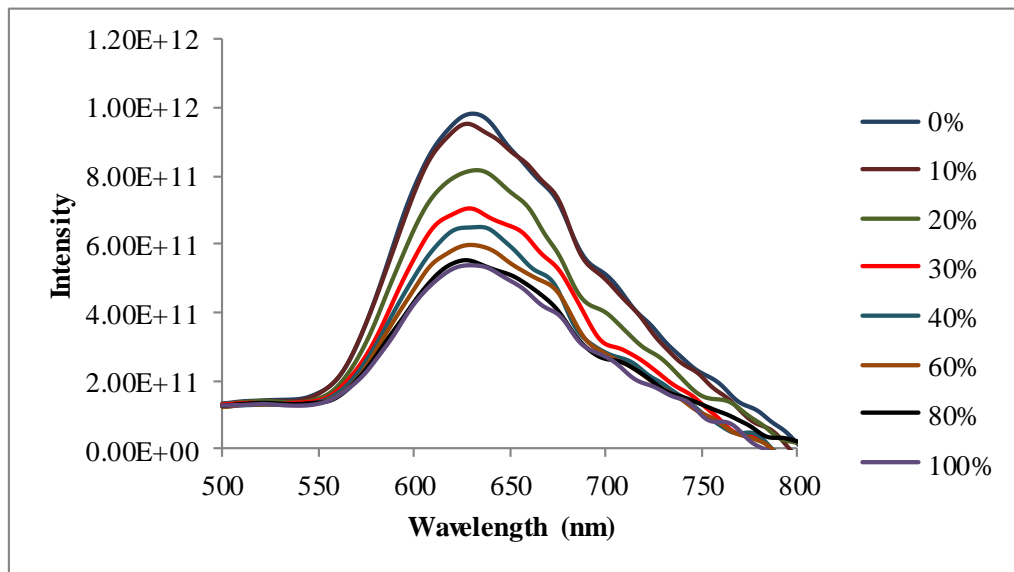


Figure 3.32 Oxygen responses of the thin film of the CS91 dye in silicon matrix in the presence of VOCs. Oxygen concentrations were shown in graphic for all results respectively.

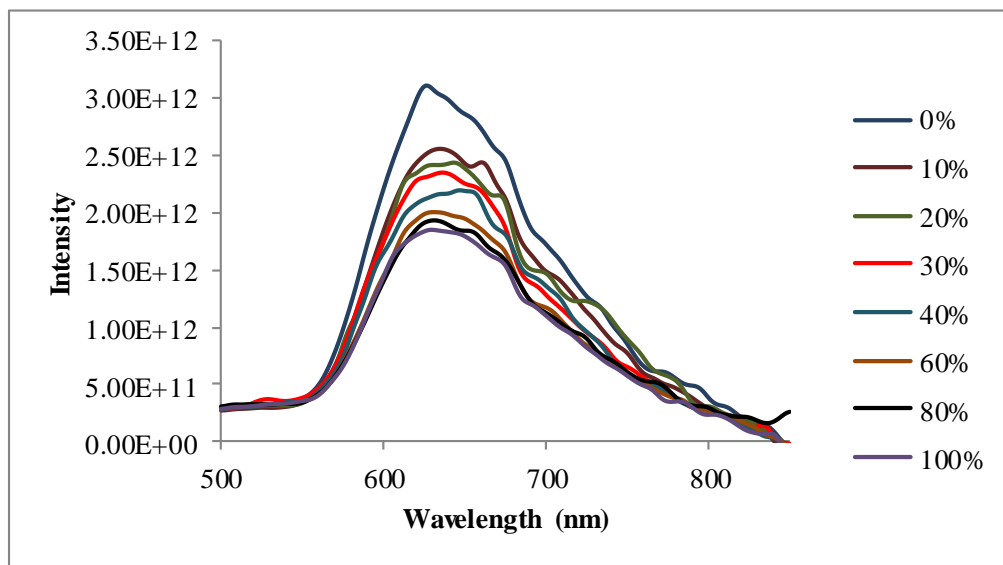


Figure 3.33 Oxygen responses of the AgNPs including thin film of the CS91 dye in silicon matrix in the presence of VOCs. Oxygen concentrations were shown in graphic for all results respectively.

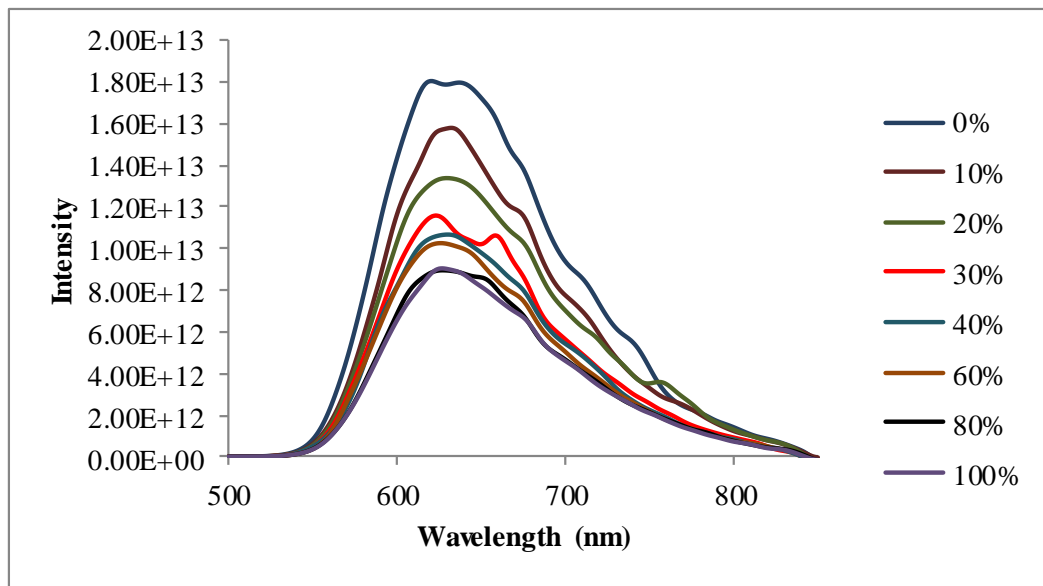


Figure 3.34 Oxygen responses of the nanofiber of the CS91 dye in silicon matrix in the presence of VOCs. Oxygen concentrations were shown in graphic for all results respectively.

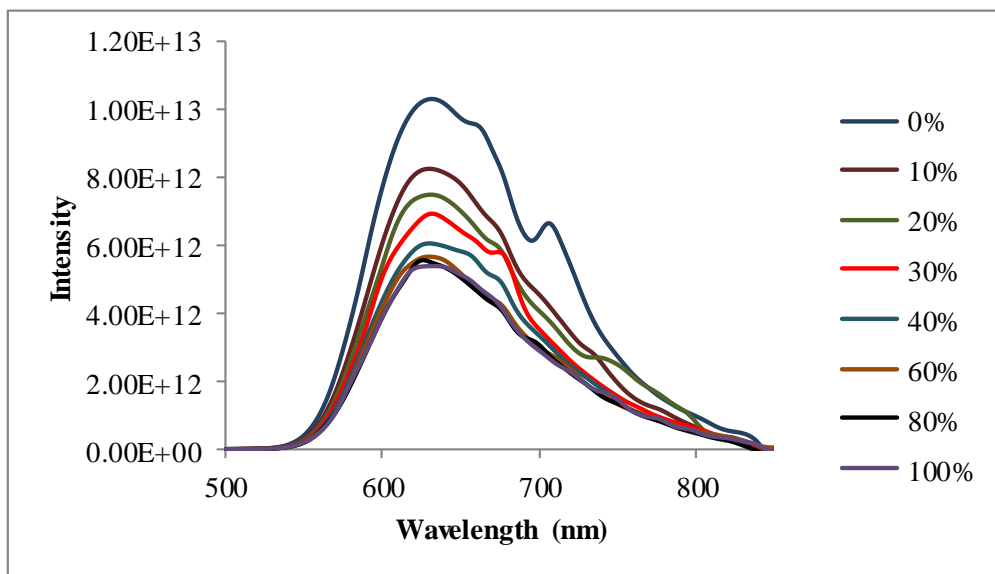


Figure 3.35 Oxygen responses of the AgNPs including nanofiber of the CS91 dye in silicon matrix in the presence of VOCs. Oxygen concentrations were shown in graphic for all results respectively.

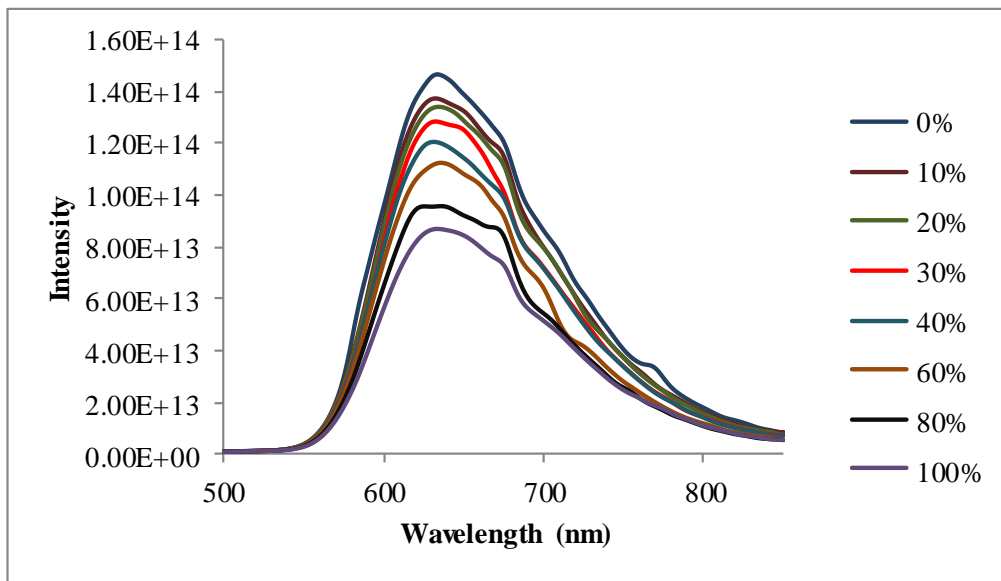


Figure 3.36 Oxygen responses of the thin film of the CS93 dye in poly(TMSP) matrix in the presence of VOCs. Oxygen concentrations were shown in graphic for all results respectively.

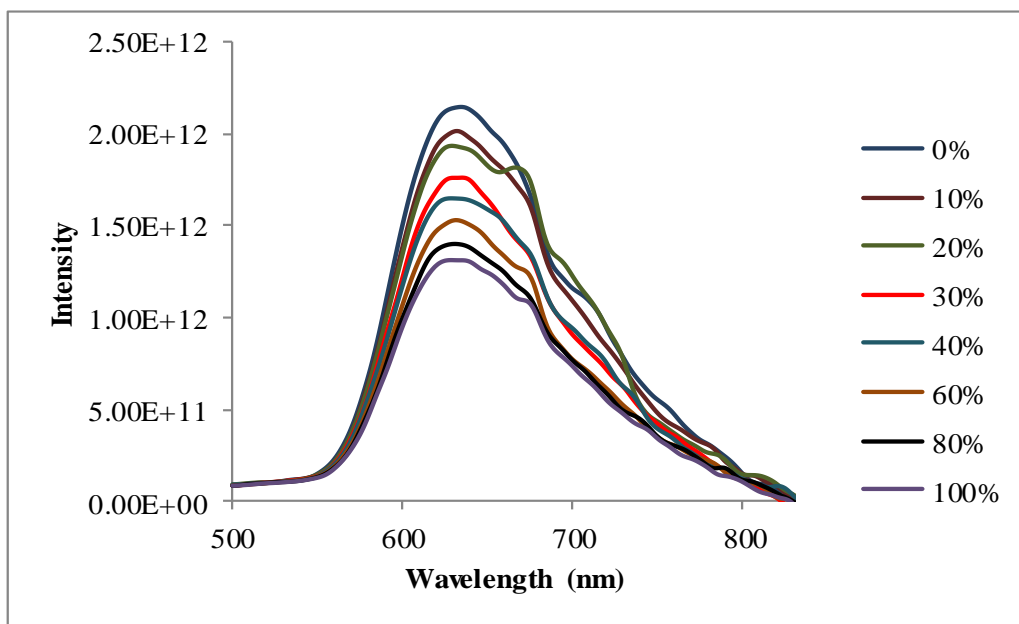


Figure 3.37 Oxygen responses of the AgNPs including thin film of the CS93 dye in poly(TMSP) matrix in the presence of VOCs. Oxygen concentrations were shown in graphic for all results respectively.

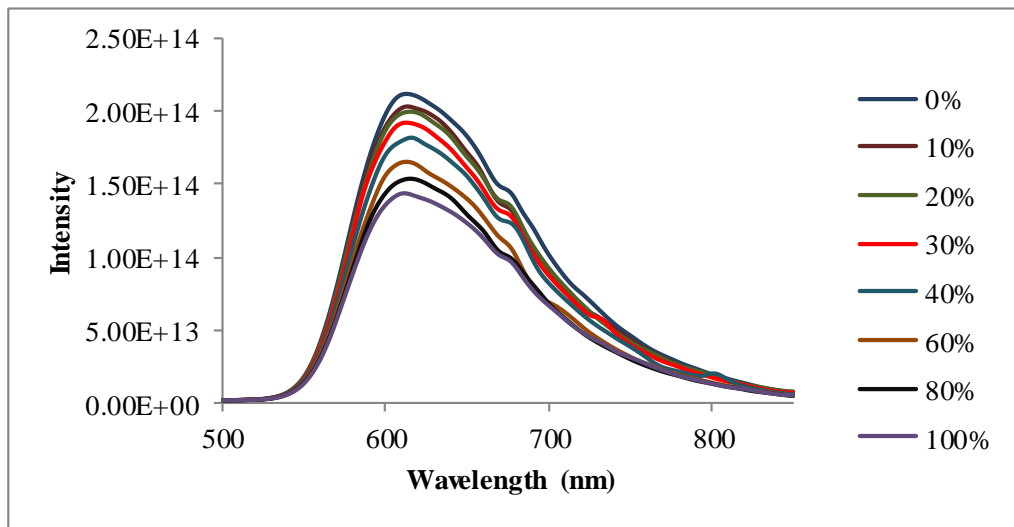


Figure 3.38 Oxygen responses of the nanofiber of the CS93 dye in poly(TMSP) matrix in the presence of VOCs. Oxygen concentrations were shown in graphic for all results respectively.

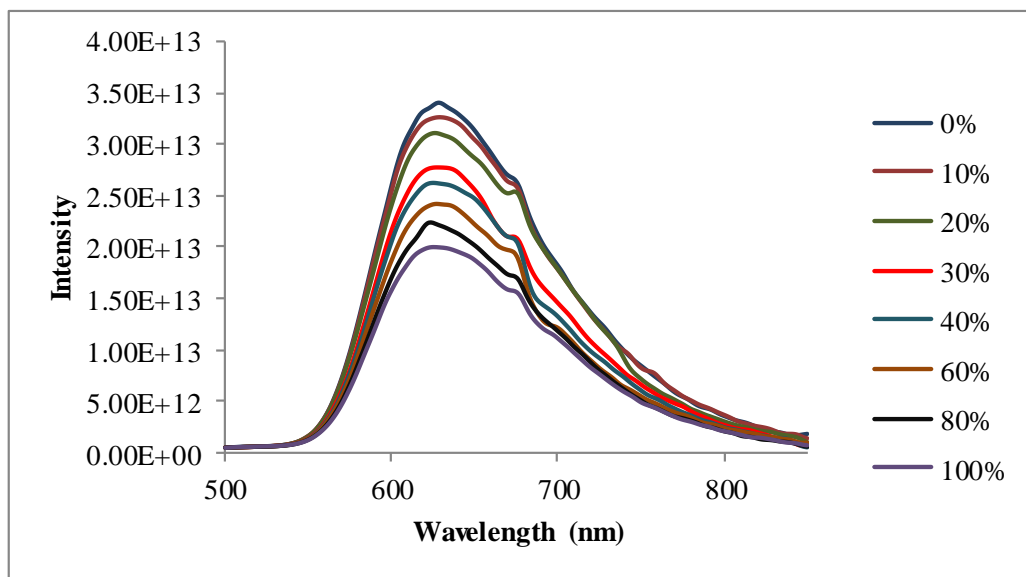


Figure 3.39 Oxygen responses of the AgNPs including nanofiber of the CS93 dye in poly(TMSP) matrix in the presence of VOCs. Oxygen concentrations were shown in graphic for all results respectively.

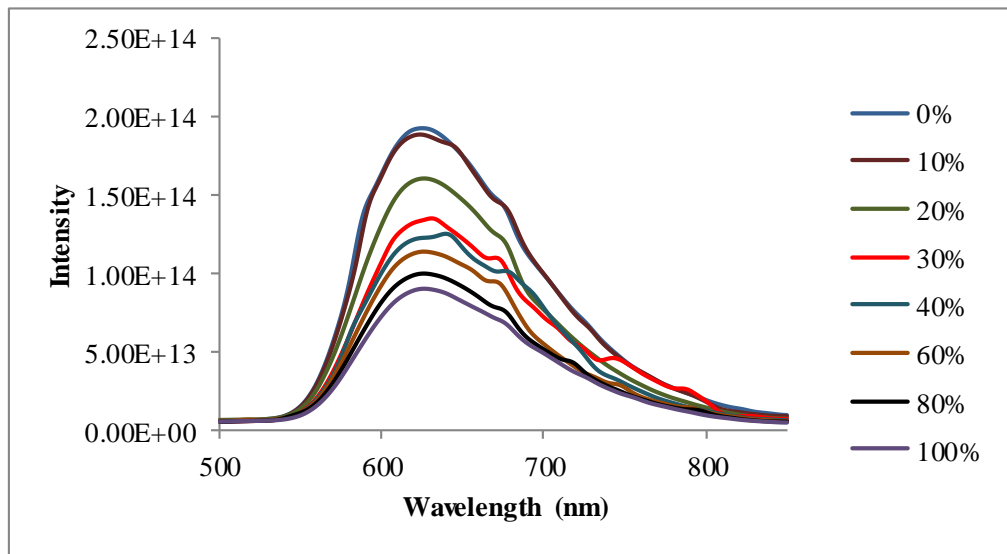


Figure 3.40 Oxygen responses of the thin film of the CS93 dye in silicon matrix in the presence of VOCs. Oxygen concentrations were shown in graphic for all results respectively.

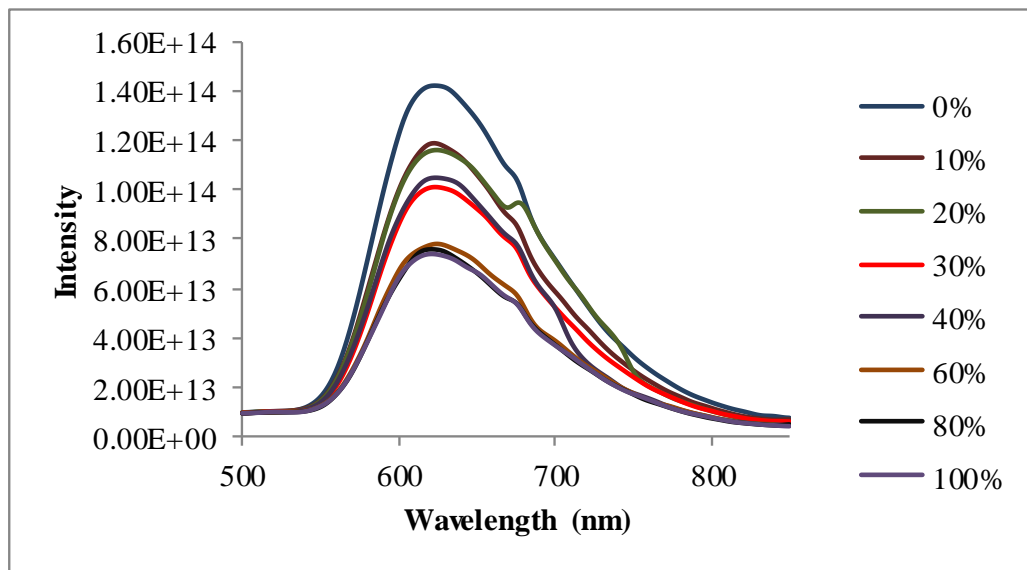


Figure 3.41 Oxygen responses of the AgNPs including thin film of the CS93 dye in silicon matrix in the presence of VOCs. Oxygen concentrations were shown in graphic for all results respectively.

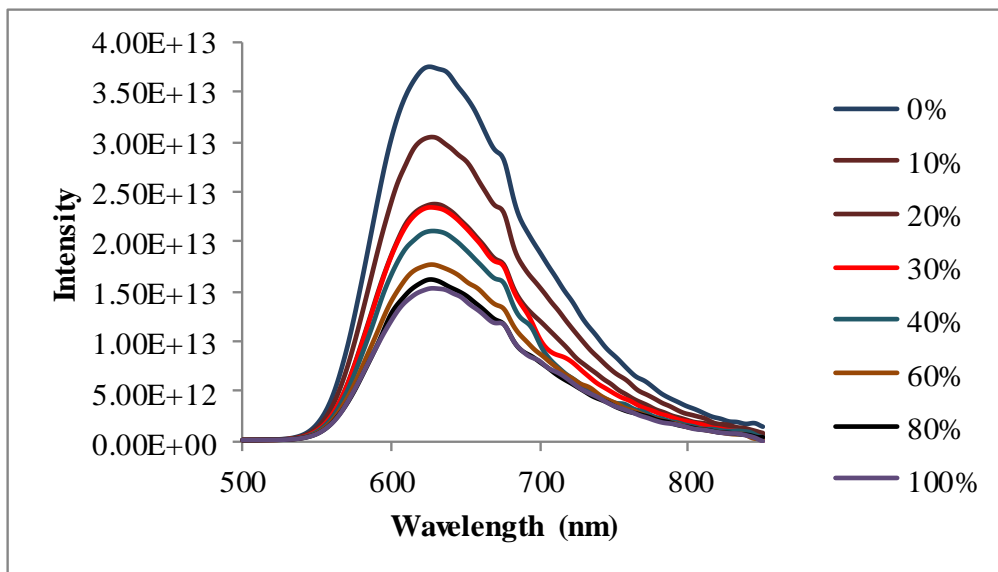


Figure 3.42 Oxygen responses of the nanofiber of the CS93 dye in silicon matrix in the presence of VOCs. Oxygen concentrations were shown in graphic for all results respectively.

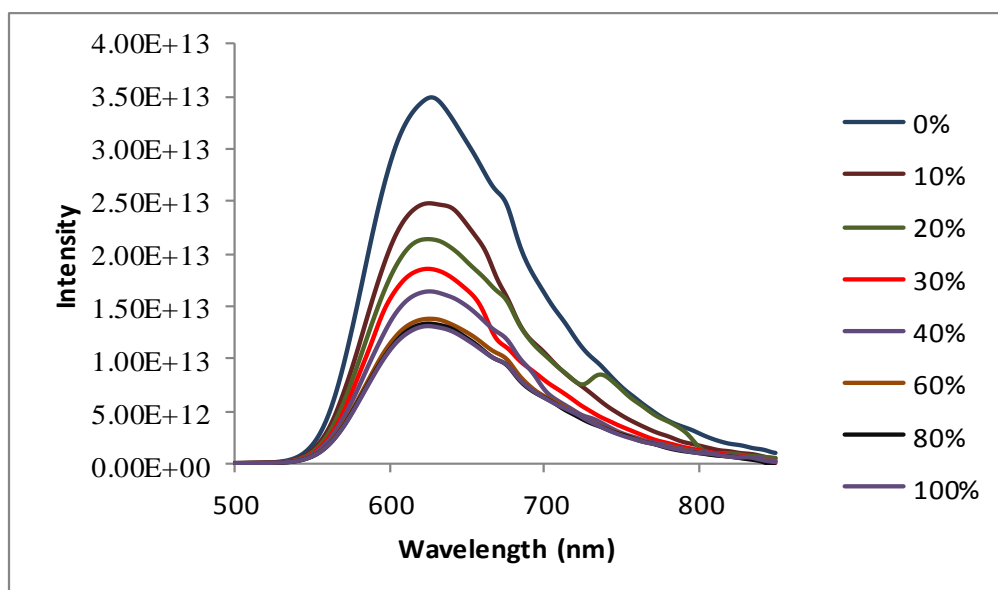


Figure 3.43 Oxygen responses of the AgNPs including nanofiber of the CS93 dye in silicon matrix in the presence of VOCs. Oxygen concentrations were shown in graphic for all results respectively.

3.3.4 Stern-Volmer Analysis of the Plots Recorded Under VOCs

The Stern-Volmer plots were derived for each sensing moiety. The slopes of the plots recorded under organic volatiles exhibited slight drops with respect to the plots recorded under clean air. However, from the Stern-Volmer constants it can be

concluded that the offered composites exhibit computing responses to oxygen even under organic volatiles. Figure 3.44 and 3.45 reveal representative Stern-Volmer plots of nanofibers and thin films of CS91 and CS93 in poly(TMSP) and silicon matrices in the presence of VOCs. The Stern-Volmer plots of all of the tested moieties under contaminated conditions were given in Table 3.6.

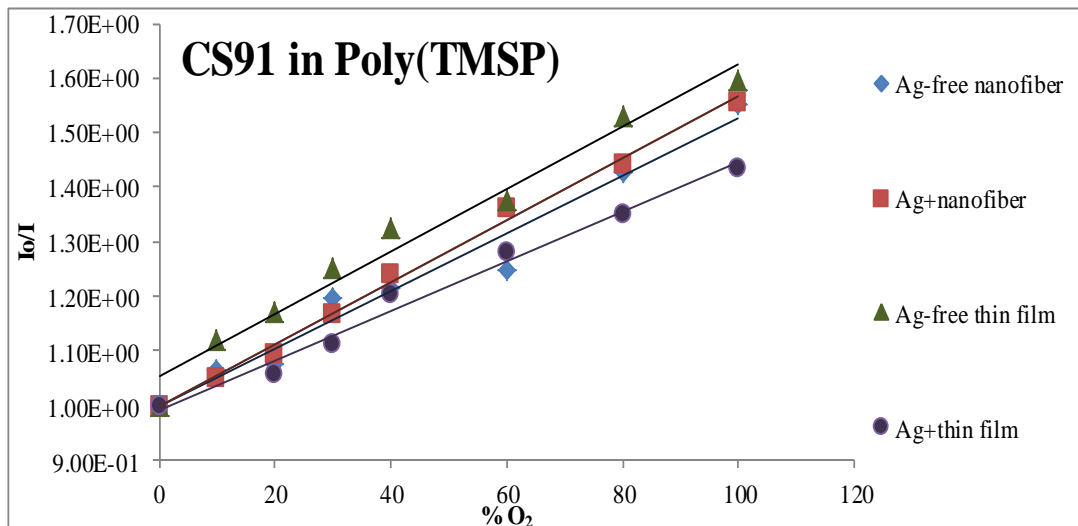


Figure 3.44 Gathered Stern-Volmer plots of nanofibers and thin films of CS91 dye in polyTMSP matrix in the presence of VOCs

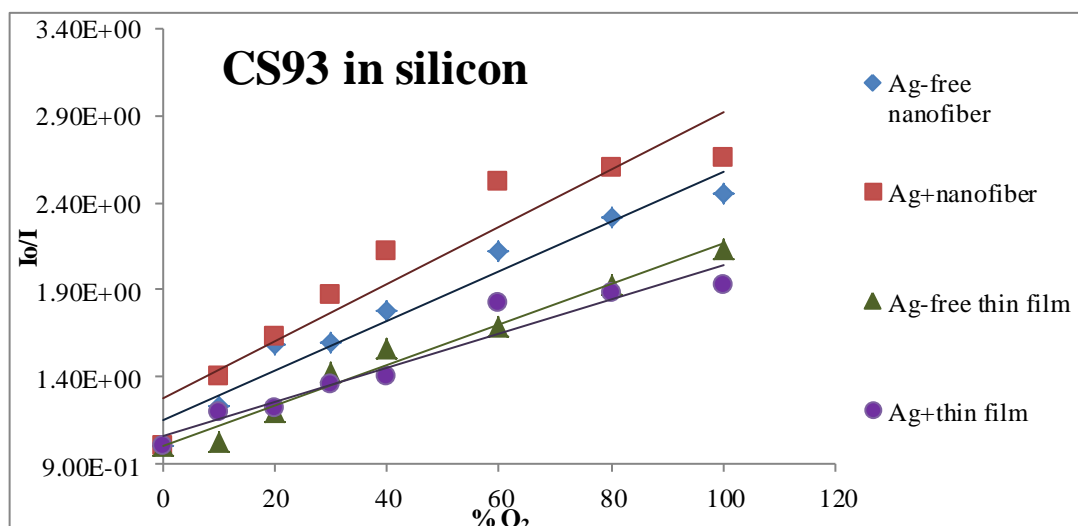


Figure 3.45 Gathered Stern-Volmer plots of nanofibers and thin films of CS93 dye in silicon matrix in the presence of VOCs.

Table 3.6 The Stern Volmer plots for contaminated conditions of volatile organics, oxygen induced relative signal changes, related regression coefficients and Ksv values extracted from the slopes of the plots.

Dye	Matrix	Thin film/nanofiber	Nano silver (mg)	Stern-Volmer plots (under organic vapors)	$K_{sv}[\text{O}_2\%]^{-1}$	Response of the composites to oxygen (%)
CS91	poly(TMSP)	TF	-	$y=0.0057x+1.0521$	0.0057	37
CS91	poly(TMSP)	NF	-	$y=0.0055x+0.9779$	0.0055	36
CS91	poly(TMSP)	TF	+	$y=0.0045x+0.9972$	0.0045	30
CS91	poly(TMSP)	NF	+	$y=0.0057x+0.9976$	0.0057	36
CS93	poly(TMSP)	TF	-	$y=0.0066x+0.9608$	0.0066	40
CS93	poly(TMSP)	NF	-	$y=0.0048x+0.9357$	0.0048	30
CS93	poly(TMSP)	TF	+	$y=0.0065x+1.0073$	0.0065	39
CS93	poly(TMSP)	NF	+	$y=0.0071x+0.9880$	0.0071	41
CS91	silicon	TF	-	$y=0.0084x+1.0149$	0.0084	45
CS91	silicon	NF	-	$y=0.0097x+1.1359$	0.0097	50
CS91	silicon	TF	+	$y=0.0061x+1.1332$	0.0061	40
CS91	silicon	NF	+	$y=0.0087x+1.1789$	0.0087	48
CS93	silicon	TF	-	$y=0.0113x+1.0337$	0.0113	53
CS93	silicon	NF	-	$y=0.0143x+1.1487$	0.0143	59
CS93	silicon	TF	+	$y=0.0096x+1.0636$	0.0096	48
CS93	silicon	NF	+	$y=0.0164x+1.2772$	0.0164	62

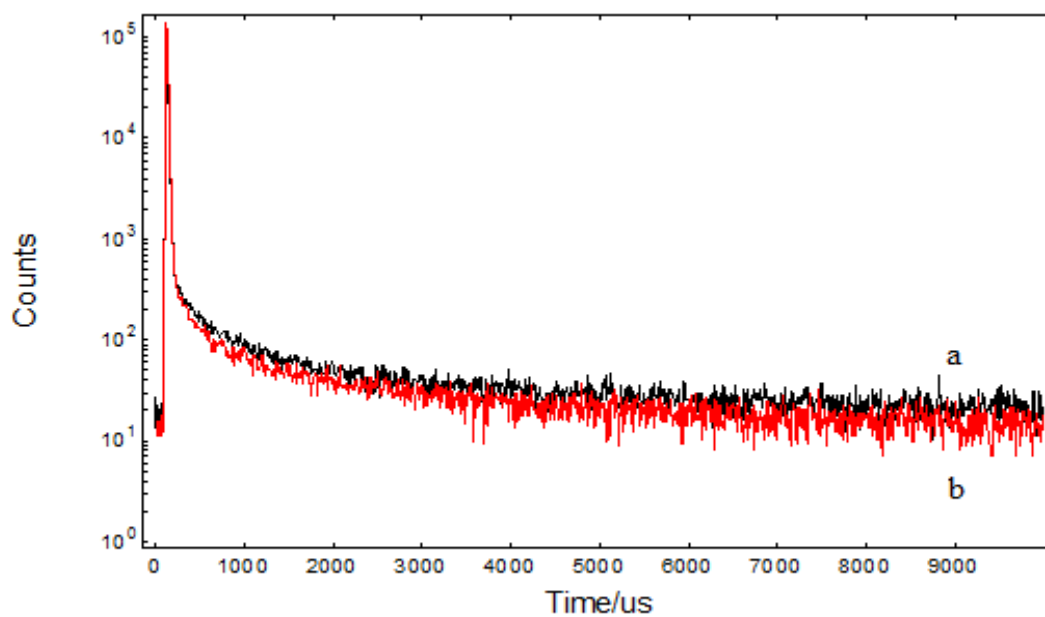
The silicon embedded CS93 exhibited the best Stern-Volmer constants and relative signal changes both in the presence and absence of the AgNPs in nanofiber forms. The silicon embedded CS91 exhibited competing results with CS93 for both in the presence and absence of the AgNPs in nanofiber forms. Calculated relative signal changes for poly(TMSP) embedded forms were less with respect to the silicon based matrices (see Table 3.6).

3.4 Lifetime Based Measurements

The fluorescence lifetimes were recorded in poly(TMSP) and in silicon in the absence and presence of the silver nanoparticles for CS91 and CS93, respectively. Similar experiments were also performed in the presence of VOCs. The dyes were excited with a microsecond flash lamp and/or a laser light source at 450 and 467 nm and the emissions were acquired at 630 nm (laser with 890 pico second pulse width). The decay characteristics were measured in oxygen free and 100 % oxygen containing moieties.

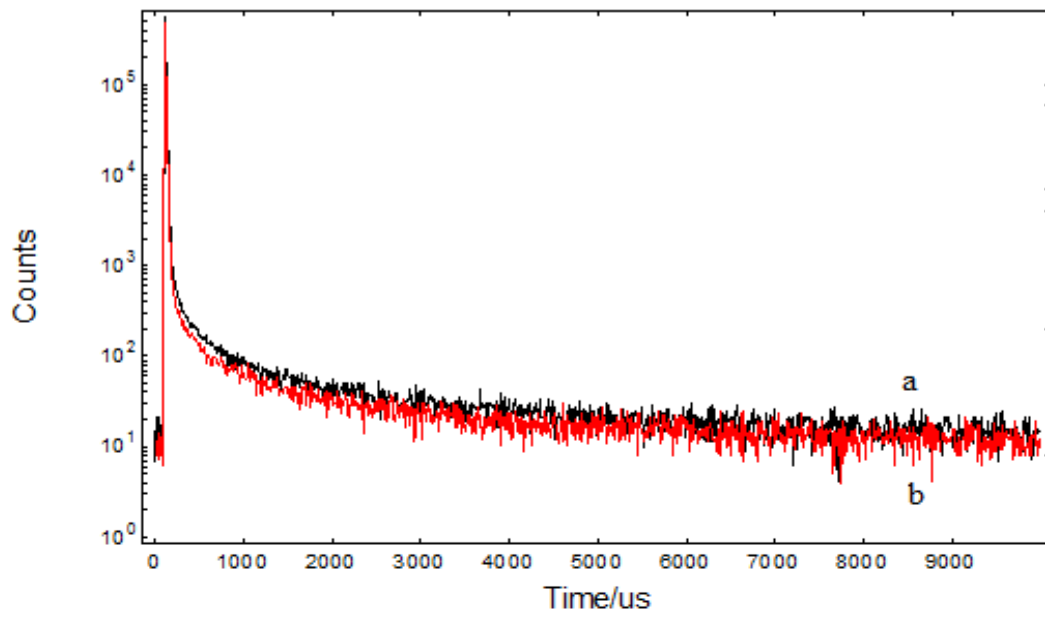
These lifetimes ranged between 172- 182 μs for the short lifetime component and between 1552- 2331 μs for the long one. The contribution of the longer lifetime component to mean lifetime was dominant and at an average of 70.0% both in the absence and presence of the quencher.

In all cases, the exploited dyes exhibited shorter lifetimes in both components in the presence of oxygen with respect to oxygen free moieties. However, the observed drops in signal intensity in the presence of quencher were not enough to draw a calibration plot for different concentrations of oxygen. In other terms the relative signal change was not high enough to derive significant calibration plots in the presence of quencher. Therefore, we did not utilize the life times as a calibration tool. The figures between 3.46- 3.49 show the comparative lifetime measurements of the poly(TMSP) embedded CS91 in both absence and presence of AgNPs under fully oxygenated and oxygen free conditions. The CS93 exhibited similar experimental results (see Figure 3.50- 3.53). From the figures it can also be concluded that there is no significant difference between the results recorded under clean air and VOCs.



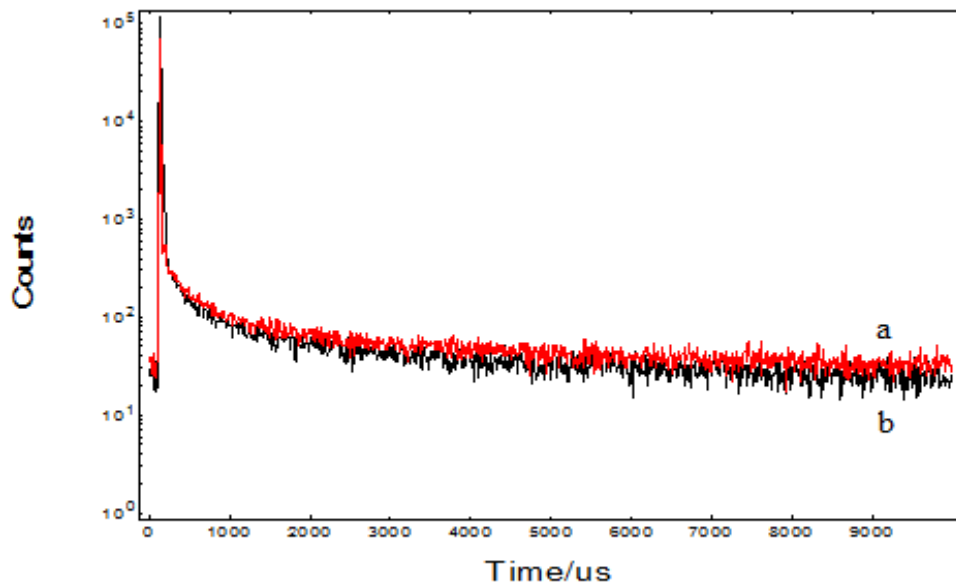
	Fix	Value / μs	Std. Dev / μs	Fix	Value	Std. Dev	Rel %
τ_1	<input type="checkbox"/>	281.7456	12.55316	B₁	<input type="checkbox"/>	241.584	6.3584
τ_2	<input type="checkbox"/>	2006.4482	105.78369	B₂	<input type="checkbox"/>	70.091	3.6054
τ_3	<input type="checkbox"/>			B₃	<input type="checkbox"/>		
τ_4	<input type="checkbox"/>			B₄	<input type="checkbox"/>		
				A	<input type="checkbox"/>	20.405	
a				$\chi^2 : 1.124$			
	Fix	Value / μs	Std. Dev / μs	Fix	Value	Std. Dev	Rel %
τ_1	<input type="checkbox"/>	198.4134	8.73320	B₁	<input type="checkbox"/>	241.881	7.2399
τ_2	<input type="checkbox"/>	1854.9191	76.61720	B₂	<input type="checkbox"/>	65.016	2.5187
τ_3	<input type="checkbox"/>			B₃	<input type="checkbox"/>		
τ_4	<input type="checkbox"/>			B₄	<input type="checkbox"/>		
				A	<input type="checkbox"/>	14.043	
b				$\chi^2 : 1.214$			

Figure 3.46 Lifetime measurements of the poly(TMSP) embedded CS91 in the presence of AgNPs under oxygen free condition(a) and fully oxygenated (b) in clean air.



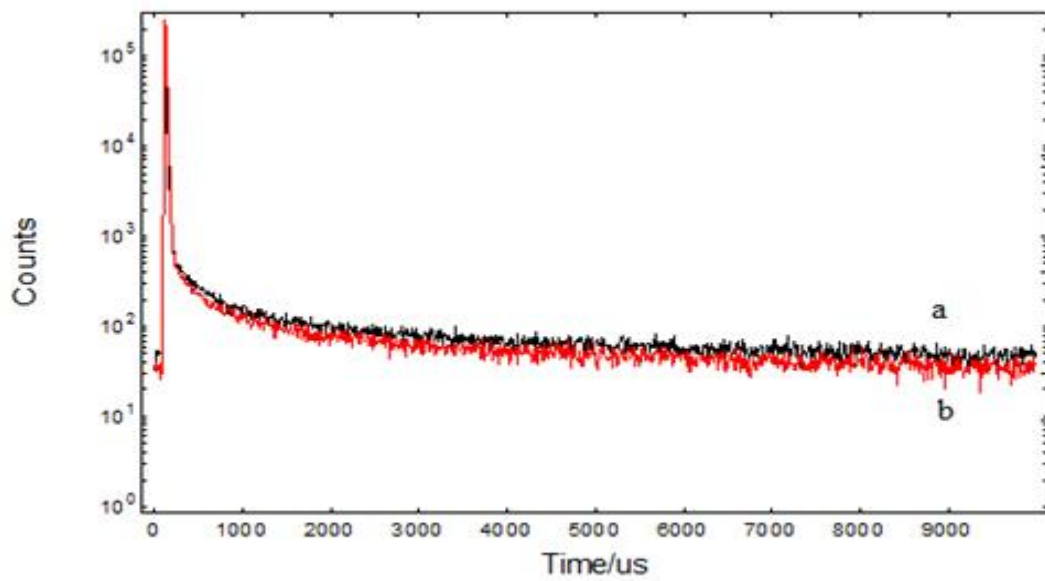
	Fix	Value / μs	Std. Dev / μs	Fix	Value	Std. Dev	Rel %
τ_1	<input type="checkbox"/>	172.8059	5.50348	B_1	<input type="checkbox"/>	447.431	33.77
τ_2	<input type="checkbox"/>	1590.2603	47.99008	B_2	<input type="checkbox"/>	95.355	66.23
τ_3	<input type="checkbox"/>			B_3	<input type="checkbox"/>		
τ_4	<input type="checkbox"/>			B_4	<input type="checkbox"/>		
				A	<input type="checkbox"/>	14.424	
a		$\chi^2 : 1.223$					
	Fix	Value / μs	Std. Dev / μs	Fix	Value	Std. Dev	Rel %
τ_1	<input type="checkbox"/>	198.4001	8.42927	B_1	<input type="checkbox"/>	263.611	33.36
τ_2	<input type="checkbox"/>	1552.3125	62.14269	B_2	<input type="checkbox"/>	67.312	66.64
τ_3	<input type="checkbox"/>			B_3	<input type="checkbox"/>		
τ_4	<input type="checkbox"/>			B_4	<input type="checkbox"/>		
				A	<input type="checkbox"/>	11.681	
b		$\chi^2 : 1.032$					

Figure 3.47 Lifetime measurements of the poly(TMSP) embedded CS91 under oxygen free condition(a) and fully oxygenated (b) in clean air.



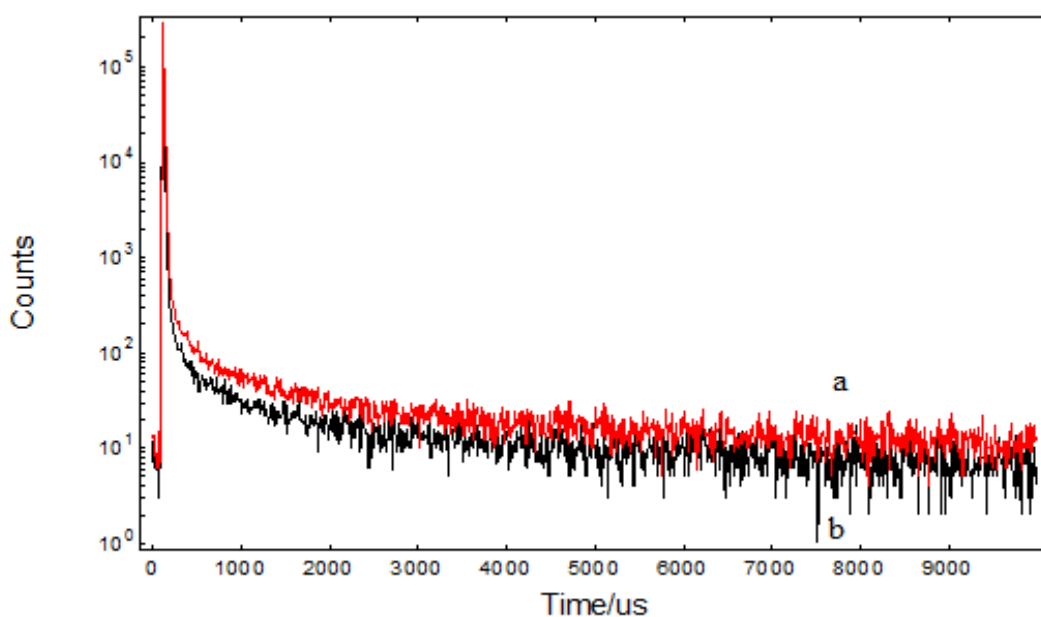
	Fix	Value / μs	Std. Dev / μs	Fix	Value	Std. Dev	Rel %
τ_1	<input type="checkbox"/>	279.0507	12.95016	B₁	<input type="checkbox"/>	238.879	6.5138
τ_2	<input type="checkbox"/>	2355.2008	138.88189	B₂	<input type="checkbox"/>	72.025	3.2769
τ_3	<input type="checkbox"/>			B₃	<input type="checkbox"/>		
τ_4	<input type="checkbox"/>			B₄	<input type="checkbox"/>		
				A	<input type="checkbox"/>	31.902	
a		$\chi^2 : 1.049$					
	Fix	Value / μs	Std. Dev / μs	Fix	Value	Std. Dev	Rel %
τ_1	<input type="checkbox"/>	168.4057	7.09278	B₁	<input type="checkbox"/>	316.128	9.3396
τ_2	<input type="checkbox"/>	1854.1170	71.97003	B₂	<input type="checkbox"/>	80.082	2.6806
τ_3	<input type="checkbox"/>			B₃	<input type="checkbox"/>		
τ_4	<input type="checkbox"/>			B₄	<input type="checkbox"/>		
				A	<input type="checkbox"/>	24.841	
b		$\chi^2 : 1.247$					

Figure 3.48 Lifetime measurements of the poly(TMSP) embedded CS91 in the presence of AgNPs under oxygen free condition(a) and fully oxygenated (b) in the presence of VOCs.



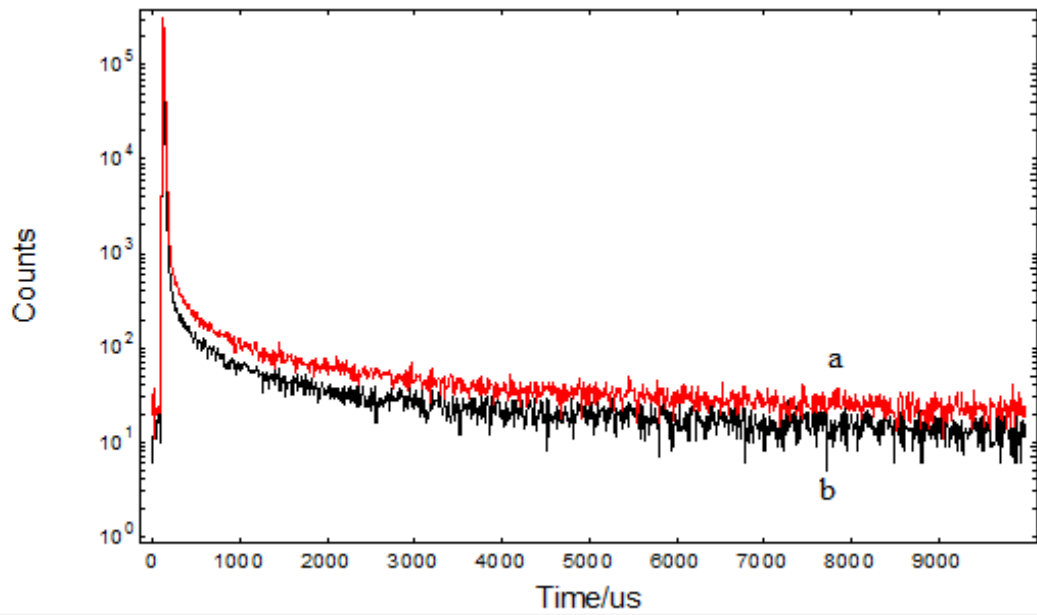
	Fix	Value / μs	Std. Dev / μs	Fix	Value	Std. Dev	Rel %
τ_1	<input type="checkbox"/>	282.9554	10.39582	B₁	<input type="checkbox"/>	363.225	7.8716
τ_2	<input type="checkbox"/>	2407.6321	116.63945	B₂	<input type="checkbox"/>	107.786	3.9303
τ_3	<input type="checkbox"/>			B₃	<input type="checkbox"/>		
τ_4	<input type="checkbox"/>			B₄	<input type="checkbox"/>		
				A	<input type="checkbox"/>	46.330	
a				$\chi^2 : 1.077$			
	Fix	Value / μs	Std. Dev / μs	Fix	Value	Std. Dev	Rel %
τ_1	<input type="checkbox"/>	259.4310	9.76870	B₁	<input type="checkbox"/>	331.310	7.6989
τ_2	<input type="checkbox"/>	2331.4040	108.67440	B₂	<input type="checkbox"/>	94.028	3.3650
τ_3	<input type="checkbox"/>			B₃	<input type="checkbox"/>		
τ_4	<input type="checkbox"/>			B₄	<input type="checkbox"/>		
				A	<input type="checkbox"/>	34.676	
b				$\chi^2 : 1.103$			

Figure 3.49 Lifetime measurements of the poly(TMSP) embedded CS91 under oxygen free condition(a) and fully oxygenated (b) in the presence of VOCs



	Fix	Value / μs	Std. Dev / μs	Fix	Value	Std. Dev	Rel %
τ_1	<input type="checkbox"/>	156.2255	8.10540	B_1	<input type="checkbox"/>	216.027	7.9011
τ_2	<input type="checkbox"/>	1577.4248	58.58992	B_2	<input type="checkbox"/>	63.214	2.3889
τ_3	<input type="checkbox"/>			B_3	<input type="checkbox"/>		
τ_4	<input type="checkbox"/>			B_4	<input type="checkbox"/>		
				A	<input checked="" type="checkbox"/>	11.410	
a				$\chi^2 : 1.177$			
	Fix	Value / μs	Std. Dev / μs	Fix	Value	Std. Dev	Rel %
τ_1	<input type="checkbox"/>	205.7377	12.87171	B_1	<input type="checkbox"/>	114.502	4.9234
τ_2	<input type="checkbox"/>	1957.0290	121.45436	B_2	<input type="checkbox"/>	28.958	1.6393
τ_3	<input type="checkbox"/>			B_3	<input type="checkbox"/>		
τ_4	<input type="checkbox"/>			B_4	<input type="checkbox"/>		
				A	<input checked="" type="checkbox"/>	5.966	
b				$\chi^2 : 1.182$			

Figure 3.50 Lifetime measurements of the silicon embedded CS93 in the presence of AgNPs under oxygen free condition (a) and fully oxygenated (b) in clean air.



	Fix	Value / μs	Std. Dev / μs	Fix	Value	Std. Dev	Rel %
τ_1	<input type="checkbox"/>	209.1253	6.94670	B₁	<input type="checkbox"/>	408.581	29.85
τ_2	<input type="checkbox"/>	1893.8588	62.20370	B₂	<input type="checkbox"/>	106.052	70.15
τ_3	<input type="checkbox"/>			B₃	<input type="checkbox"/>		
τ_4	<input type="checkbox"/>			B₄	<input type="checkbox"/>		
				A	<input type="checkbox"/>	22.273	
a				$\chi^2 : 1.155$			
	Fix	Value / μs	Std. Dev / μs	Fix	Value	Std. Dev	Rel %
τ_1	<input type="checkbox"/>	229.1185	10.57001	B₁	<input type="checkbox"/>	214.986	30.71
τ_2	<input type="checkbox"/>	1903.7827	89.76011	B₂	<input type="checkbox"/>	58.368	69.29
τ_3	<input type="checkbox"/>			B₃	<input type="checkbox"/>		
τ_4	<input type="checkbox"/>			B₄	<input type="checkbox"/>		
				A	<input type="checkbox"/>	12.829	
b				$\chi^2 : 1.169$			

Figure 3.51 Lifetime measurements of the silicon embedded CS93 under oxygen free condition (a) and fully oxygenated (b) in clean air.

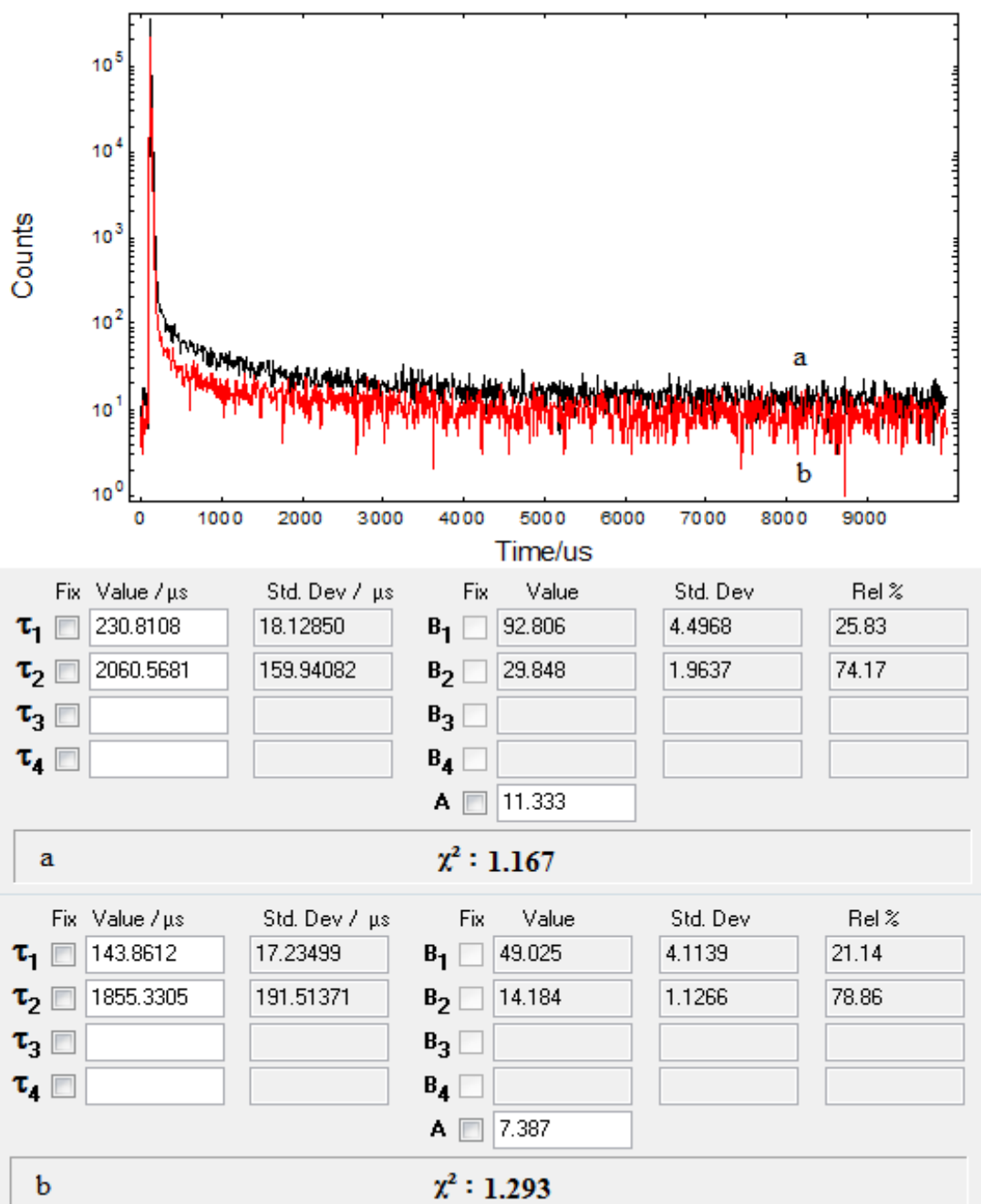
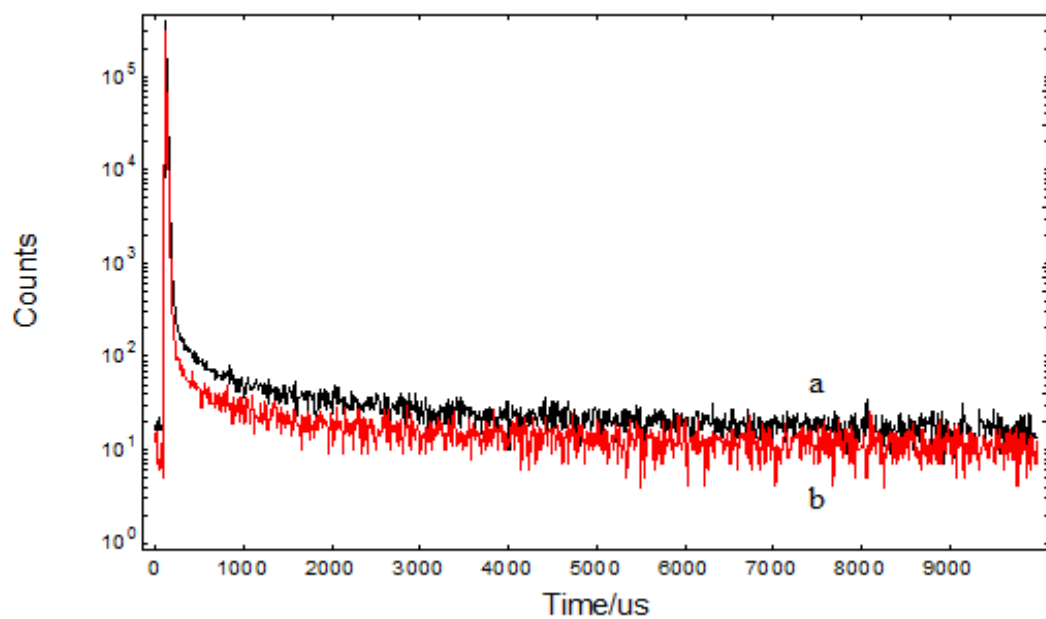


Figure 3.52 Lifetime measurements of the silicon embedded CS93 in the presence of AgNPs under oxygen free condition (a) and fully oxygenated (b) in the presence of VOCs.



	Fix	Value / μs	Std. Dev / μs	Fix	Value	Std. Dev	Rel %	
τ_1	<input type="checkbox"/>	170.7269	10.81183	B_1	<input type="checkbox"/>	154.913	6.6781	23.02
τ_2	<input type="checkbox"/>	1866.3168	96.56949	B_2	<input type="checkbox"/>	47.390	2.0785	76.98
τ_3	<input type="checkbox"/>			B_3	<input type="checkbox"/>			
τ_4	<input type="checkbox"/>			B_4	<input type="checkbox"/>			
				A	<input type="checkbox"/>	15.902		
a				$\chi^2 : 1.078$				
	Fix	Value / μs	Std. Dev / μs	Fix	Value	Std. Dev	Rel %	
τ_1	<input type="checkbox"/>	164.3820	18.16351	B_1	<input type="checkbox"/>	68.330	4.8126	22.78
τ_2	<input type="checkbox"/>	1625.1651	133.26436	B_2	<input type="checkbox"/>	23.425	1.7767	77.22
τ_3	<input type="checkbox"/>			B_3	<input type="checkbox"/>			
τ_4	<input type="checkbox"/>			B_4	<input type="checkbox"/>			
				A	<input type="checkbox"/>	10.354		
b				$\chi^2 : 1.174$				

Figure 3.53 Lifetime measurements of the silicon embedded CS93 under oxygen free condition (a) and fully oxygenated (b) in the presence of VOCs.

3.5 Response and Regeneration Characteristics

The response characteristics of CS91 and CS93 were tested in an alternating atmosphere of O₂ and N₂. Fig 3.50-3.81 illustrates response and regeneration performances of CS91 in poly(TMSP) and CS93 in silicon for Ag-free matrices, respectively. The data were acquired both for clean air and under volatile organic compounds. The responses shown between the figures 31-65 are belong to clean air and the ones between 66- 81 were recorded under vapors of organic volatiles. Almost all of the kinetic response curves exhibited a good performance in alternating atmospheres of oxygen and nitrogen with a good reproducibility. The reproducibility tests were applied during 1800 seconds for all of the sensing agents. They yielded varying numbers of cycles ranging between 34- 41. This means 52.9 sec. and 43.9 sec of response- recovery time for the slowest and the fastest individual cycles, respectively. Response time is defined as the time taken to attain 90% of the signal intensity (τ_{90}) when the gas is changed. The individual response times of Ag-free forms were in the range of 3–12 s when going to higher O₂ concentrations.

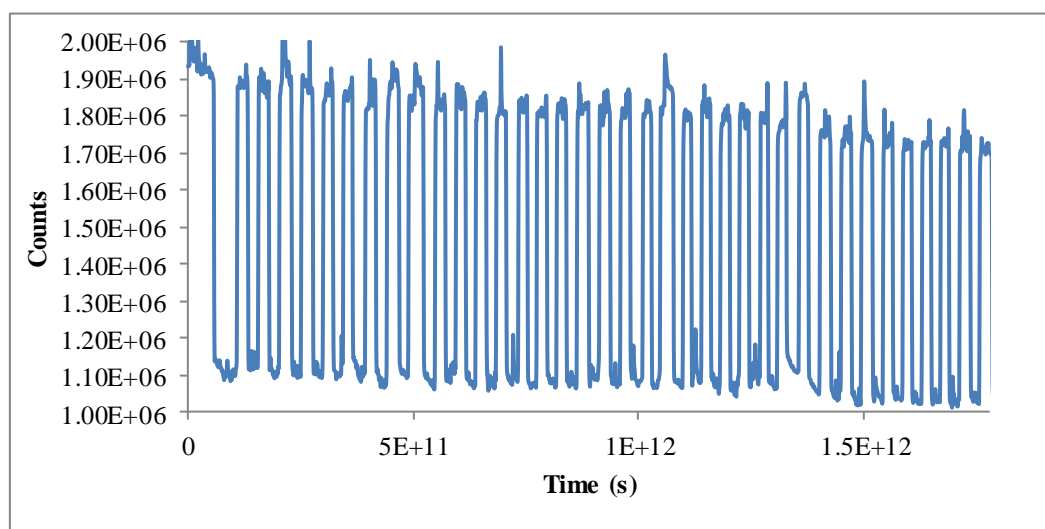


Figure 3.54 Kinetic results of the thin film of the CS91 dye in poly(TMSP) matrix.

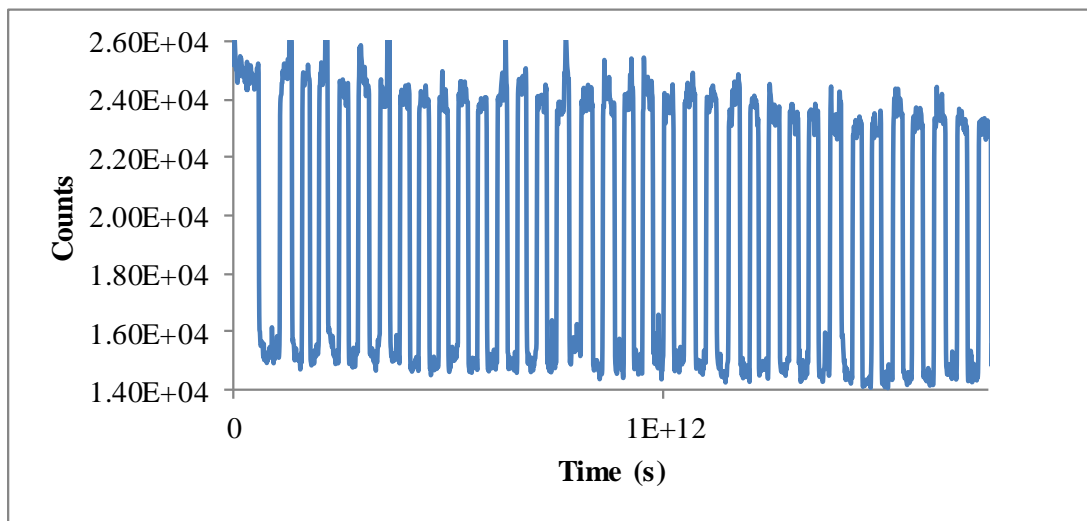


Figure 3.55 Kinetic results of the AgNPs including thin film of the CS91 dye in poly(TMSP) matrix.

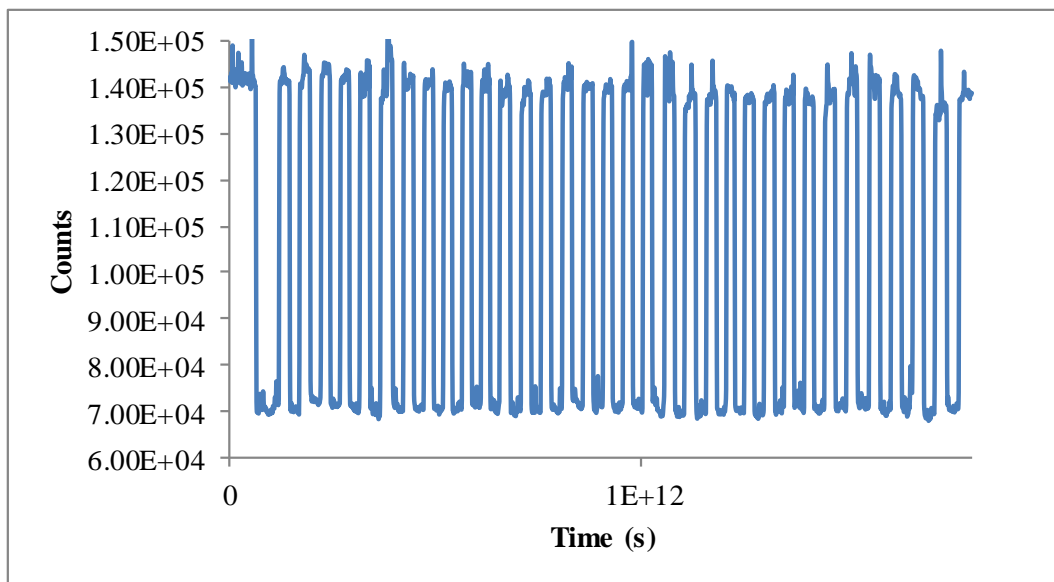


Figure 3.56 Kinetic results of the nanofibers of the CS91 dye in poly(TMSP) matrix.

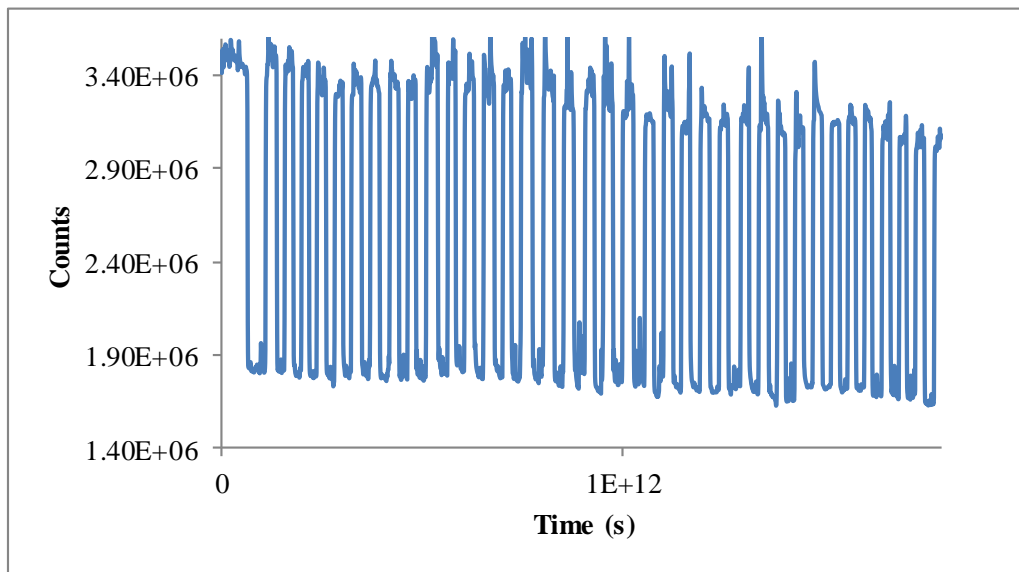


Figure 3.57 Kinetic results of the AgNPs including nanofibers of the CS91 dye in poly(TMSP) matrix.

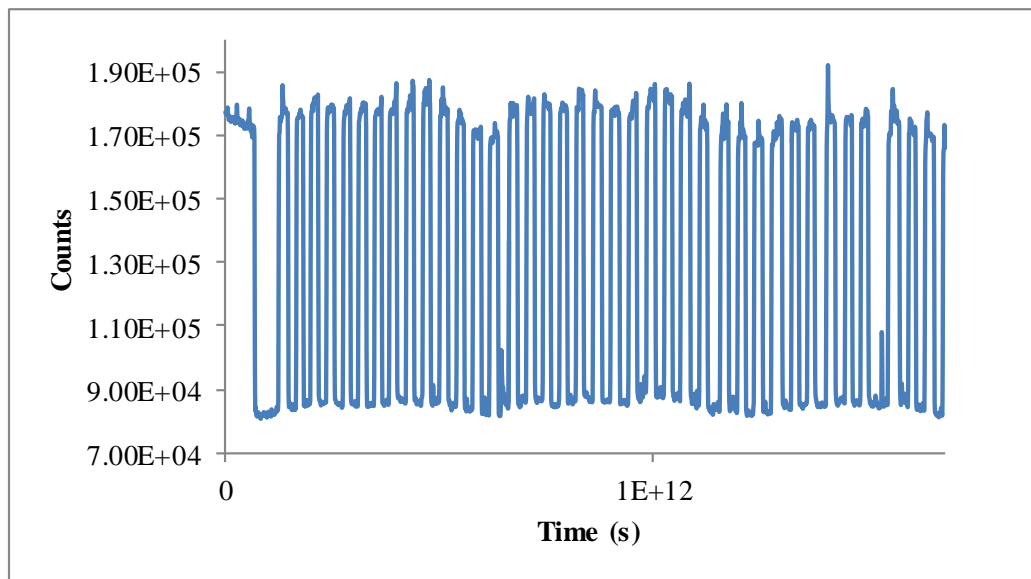


Figure 3.58 Kinetic results of the thin film of the CS91 dye in silicon matrix.

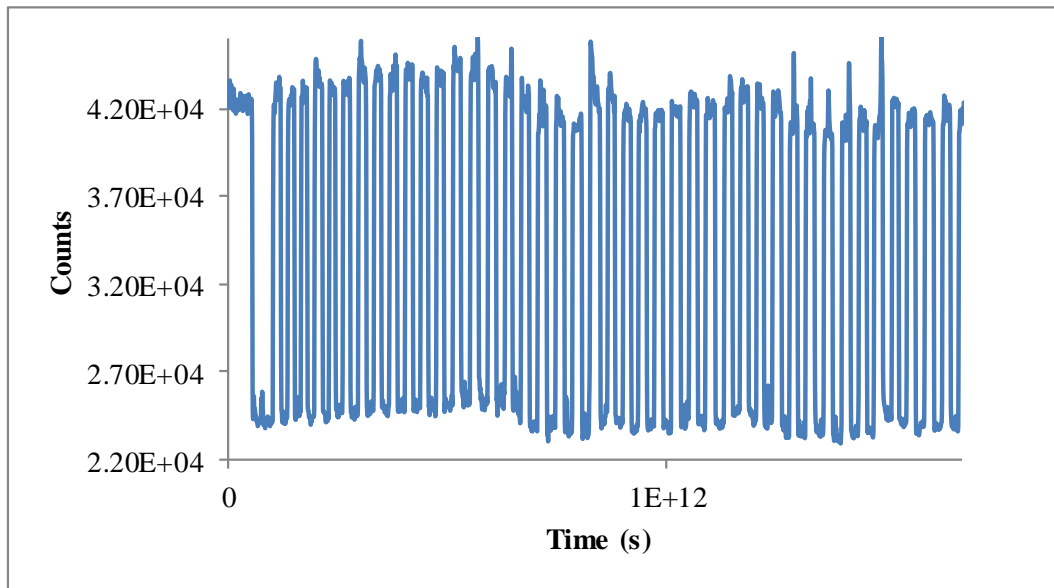


Figure 3.59 Kinetic results of the AgNPs including thin film of the CS91 dye in silicon matrix.

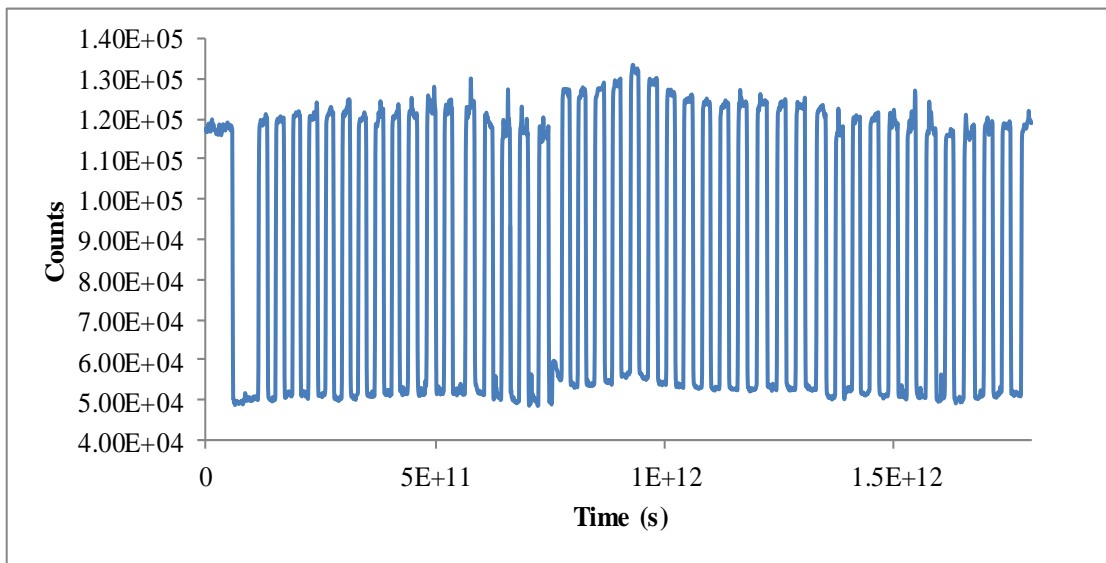


Figure 3.60 Kinetic results of the nanofiber of the CS91 dye in silicon matrix.

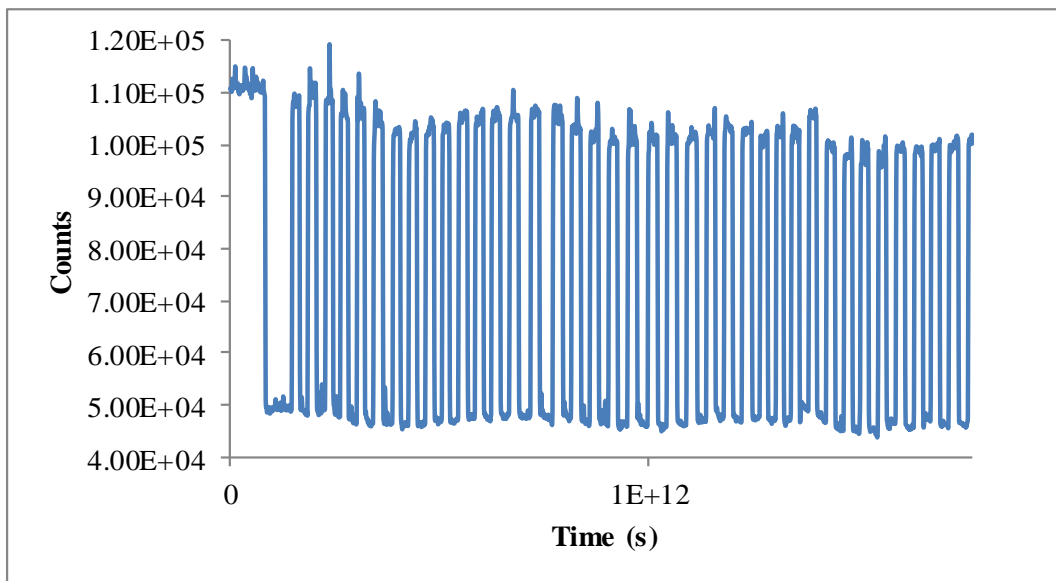


Figure 3.61 Kinetic results of the AgNPs including nanofiber of the CS91 dye in silicon matrix.

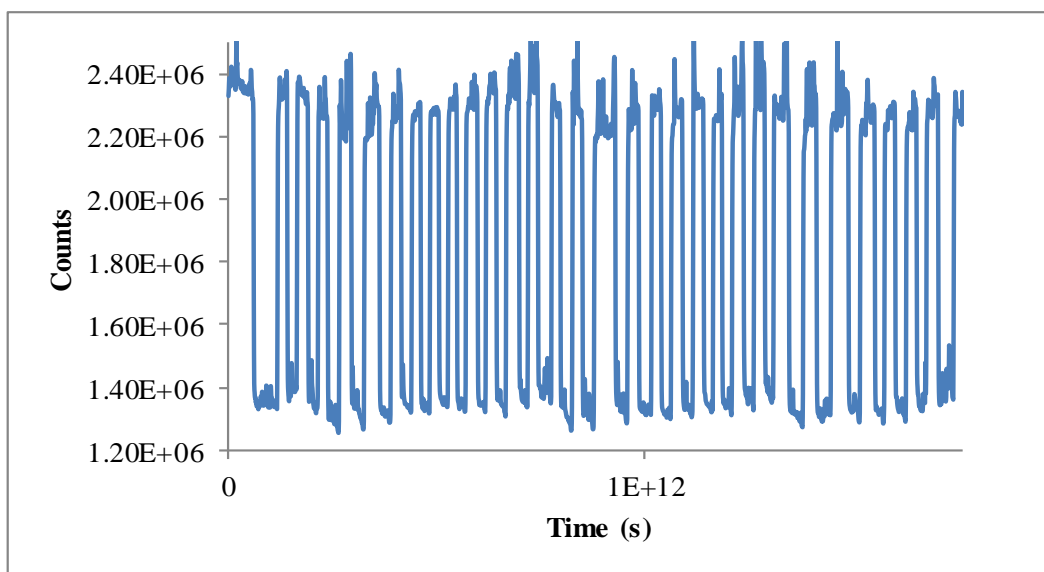


Figure 3.62 Kinetic results of the thin film of the CS93 dye in poly(TMSP) matrix.

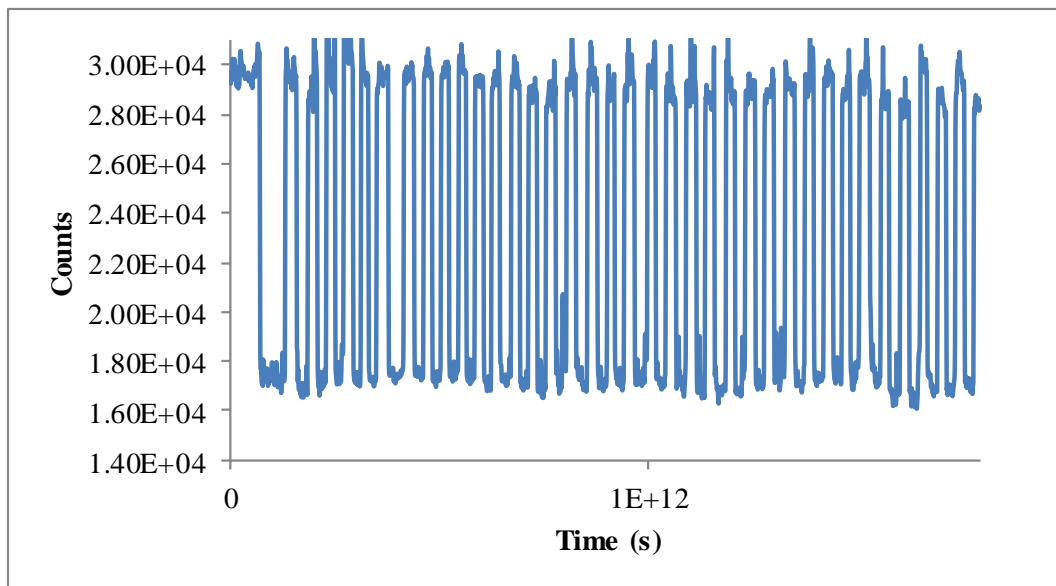


Figure 3.63 Kinetic results of the AgNPs including thin film of the CS93 dye in poly(TMSP) matrix.

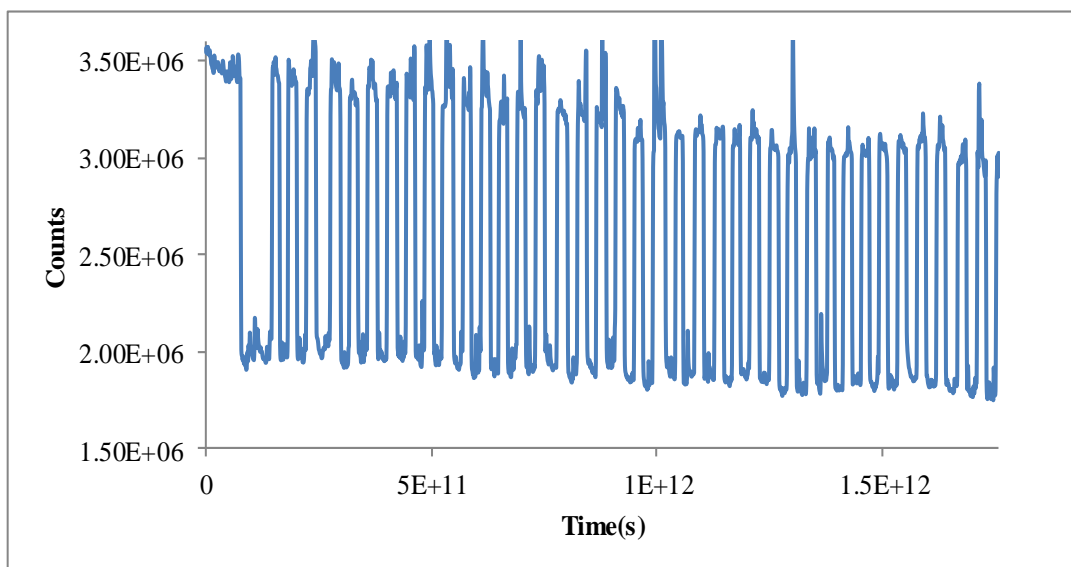


Figure 3.64 Kinetic results of the nanofibers of the CS93 dye in poly(TMSP) matrix.

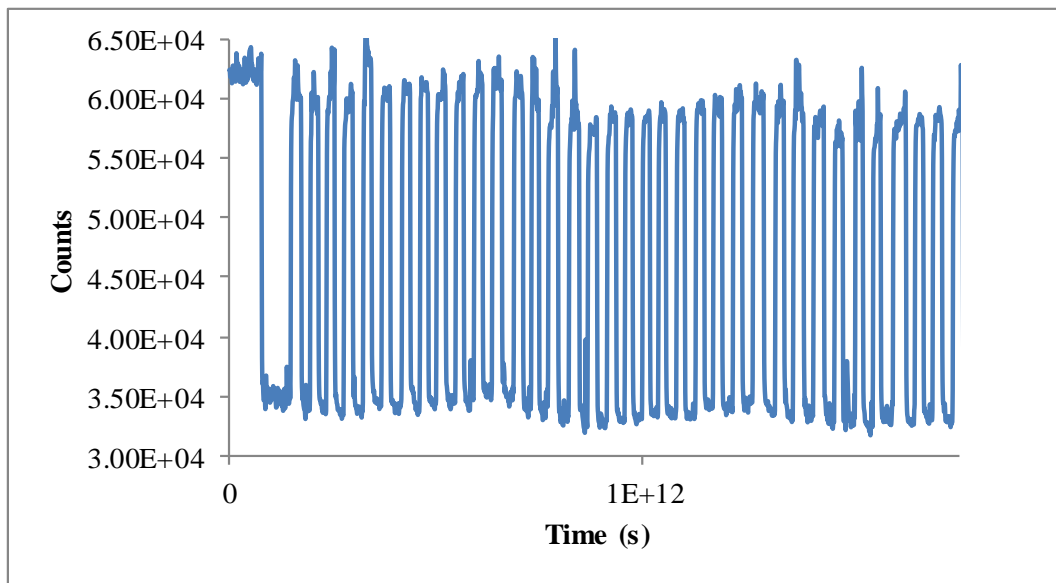


Figure 3.65 Kinetic results of the AgNPs including nanofibers of the CS93 dye in poly(TMSP) matrix.

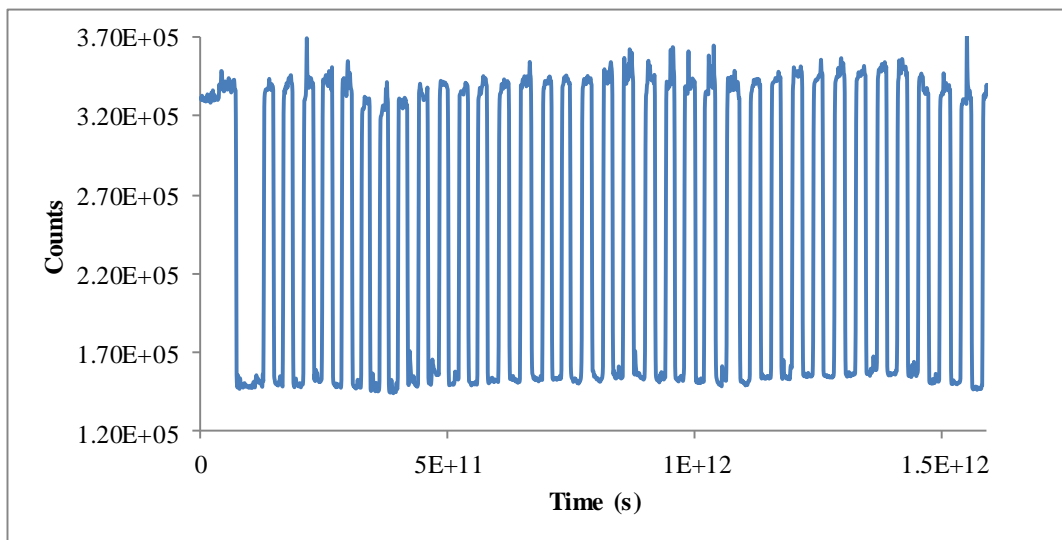


Figure 3.66 Kinetic results of the thin film of the CS93 dye in silicon matrix.

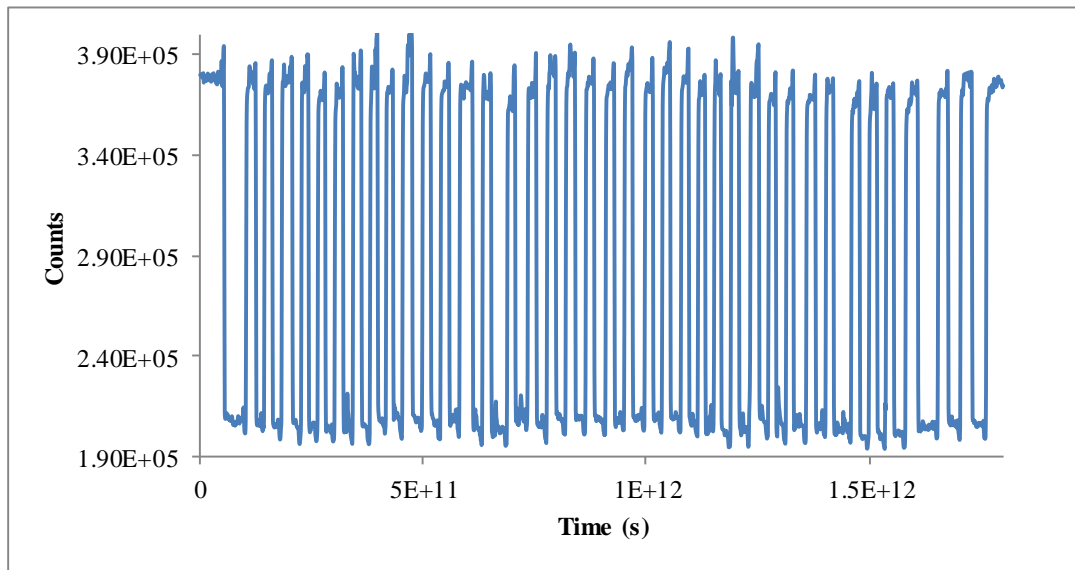


Figure 3.67 Kinetic results of the AgNPs thin film of the CS93 dye in silicon matrix.

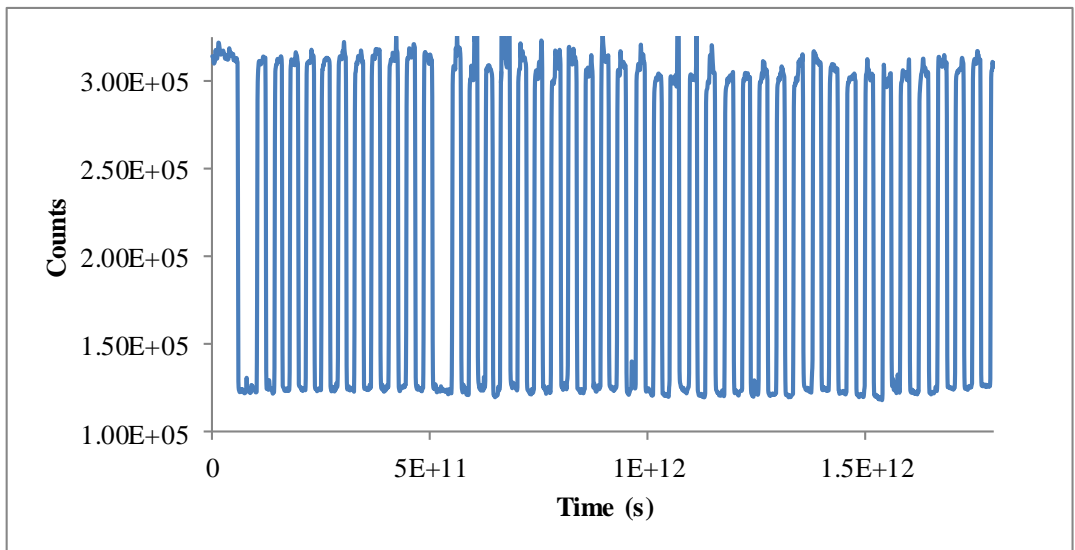


Figure 3.68 Kinetic results of the nanofibers of the CS93 dye in silicon matrix.

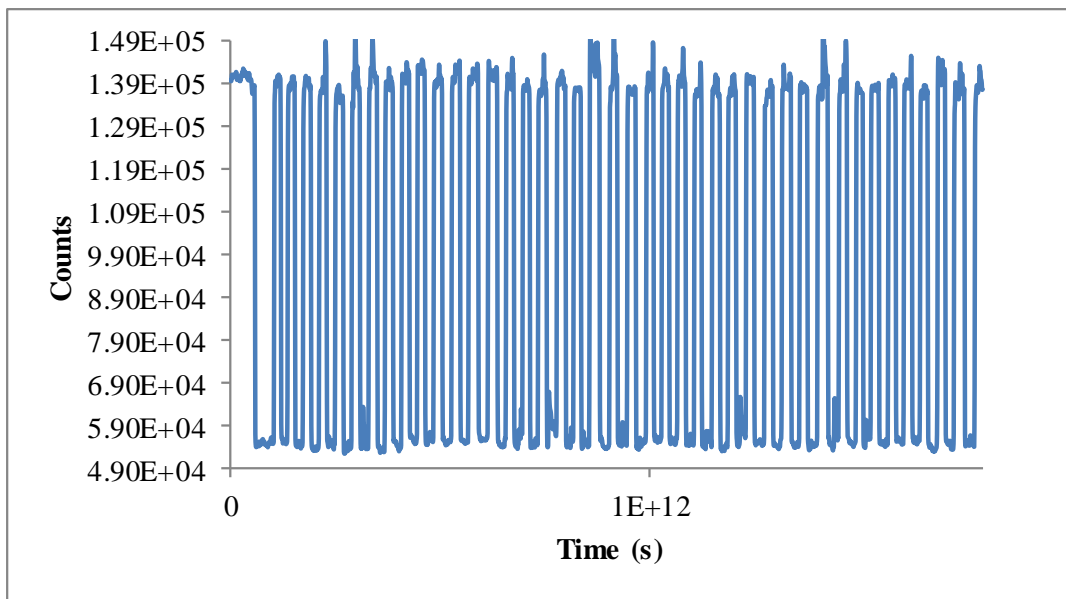


Figure 3.69 Kinetic results of the AgNPs nanofiber of the CS93 dye in silicon matrix.

The kinetic data shown in the Figures 3.59, 3.61, 3.63 and 3.66- 3.69 indicate the best reproducibility performance without any drift. They exhibited low standard deviation for the upper and lower signal averages under clean air conditions. Among the figures between 3.50- 3.65 the figures of 3.50, 3.51, 3.53 and 3.60 indicate a drift after repeated cycles which is an indicator of a bad regeneration performance.

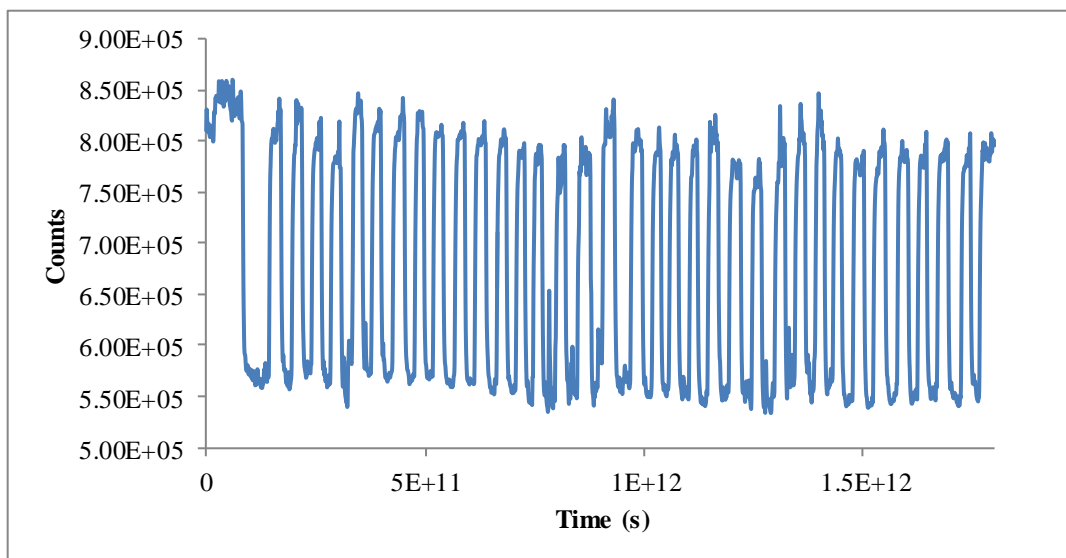


Figure 3.70 Kinetic results of the thin film of the CS91 dye in poly(TMSP) matrix in the presence of VOCs.

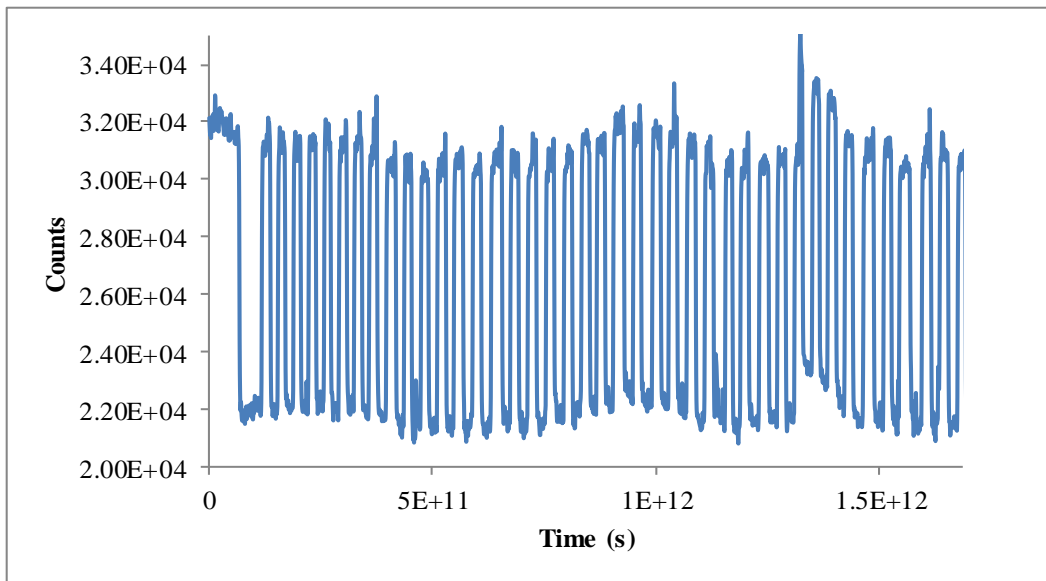


Figure 3.71 Kinetic results of the AgNPs including thin film of the CS91 dye in poly(TMSP) matrix in the presence of VOCs.

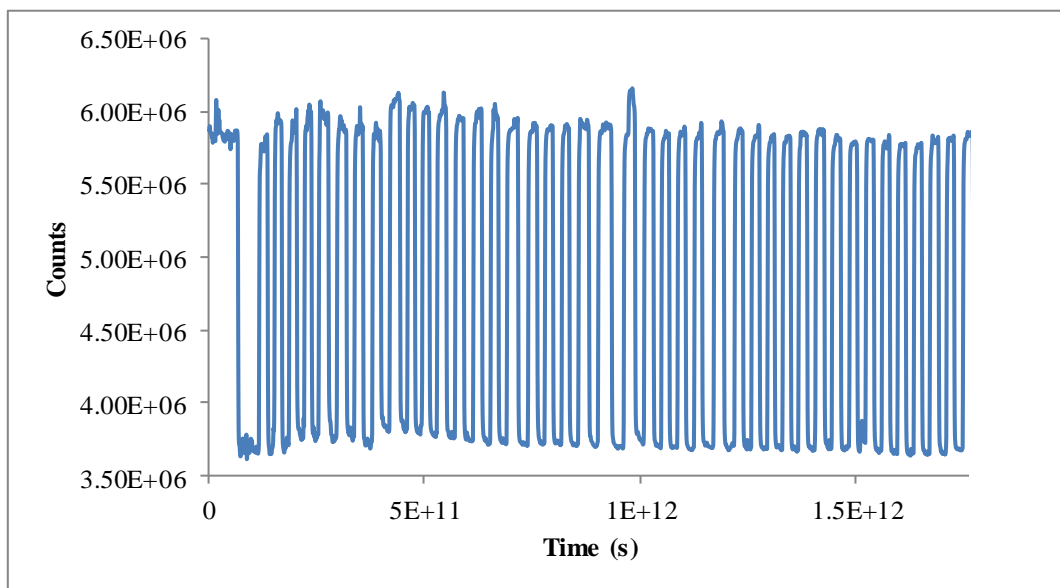


Figure 3.72 Kinetic results of the nanofiber of the CS91 dye in poly(TMSP) matrix in the presence of VOCs.

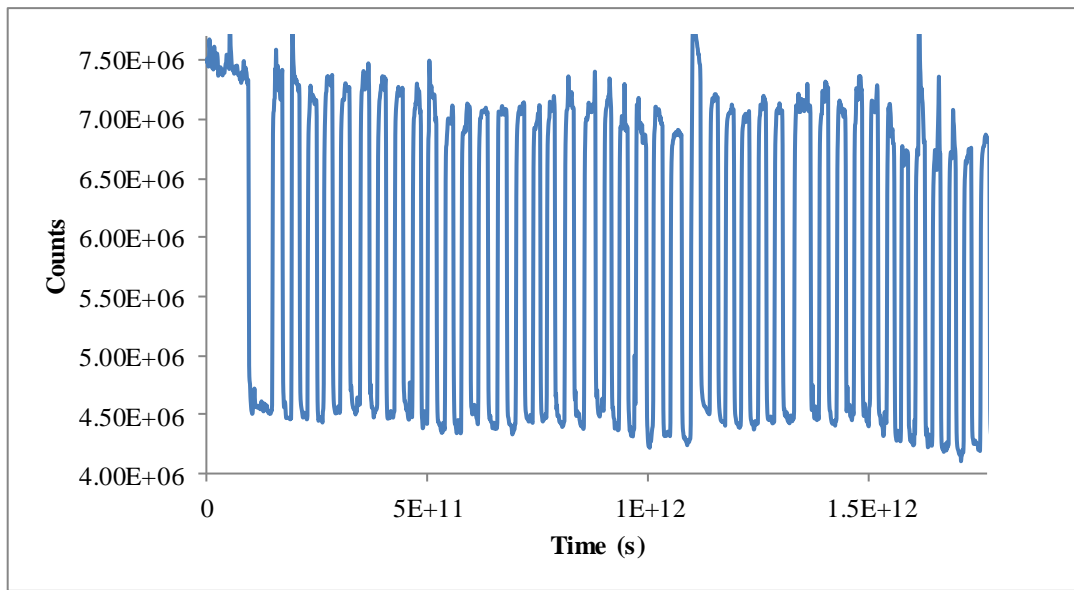


Figure 3.73 Kinetic results of the AgNPs including nanofiber of the CS91 dye in poly(TMSP) matrix in the presence of VOCs.

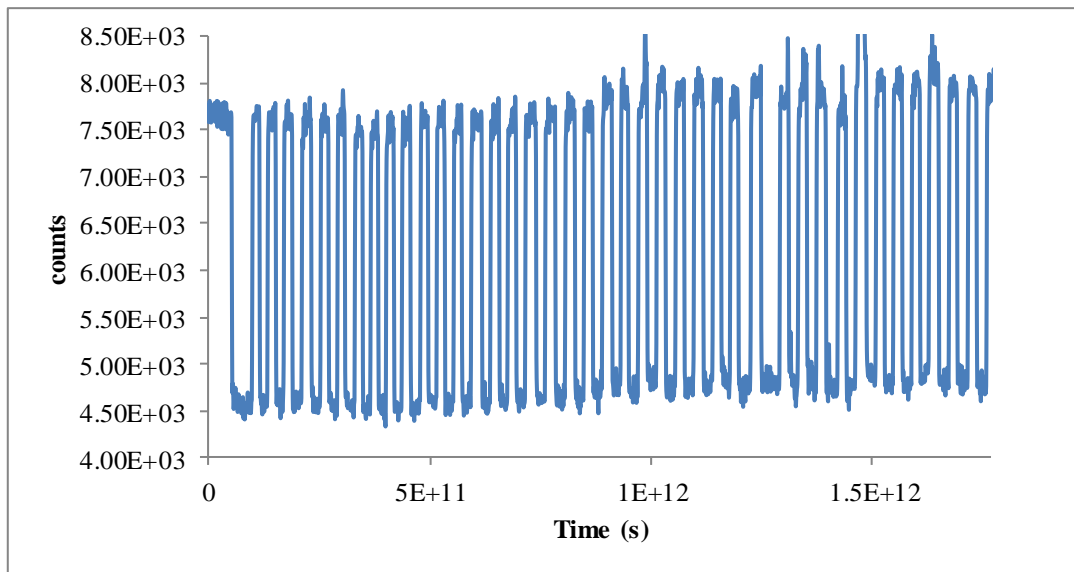


Figure 3.74 Kinetic results of the thin film of the CS91 dye in silicon matrix in the presence of VOCs.

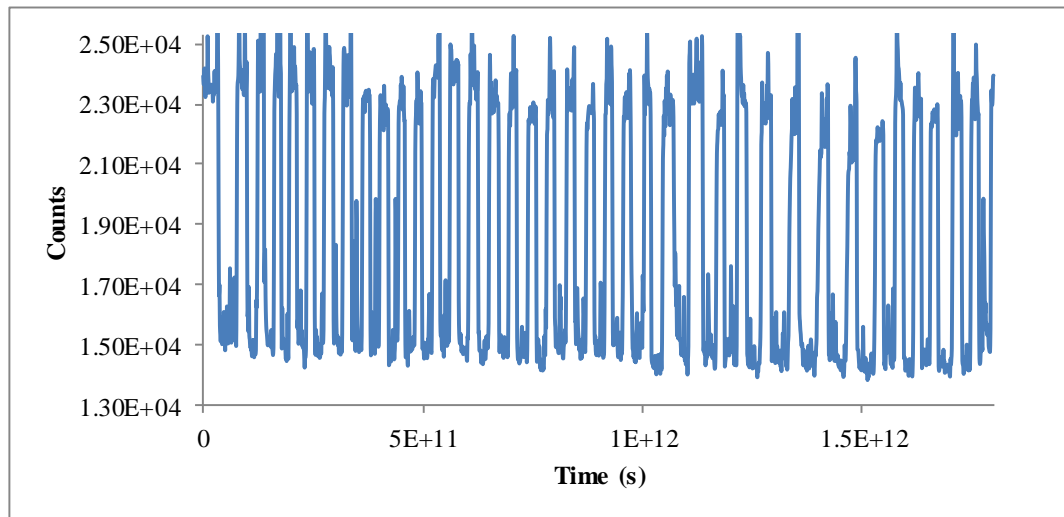


Figure 3.75 Kinetic results of the AgNPs including thin film of the CS91 dye in silicon matrix in the presence of VOCs.

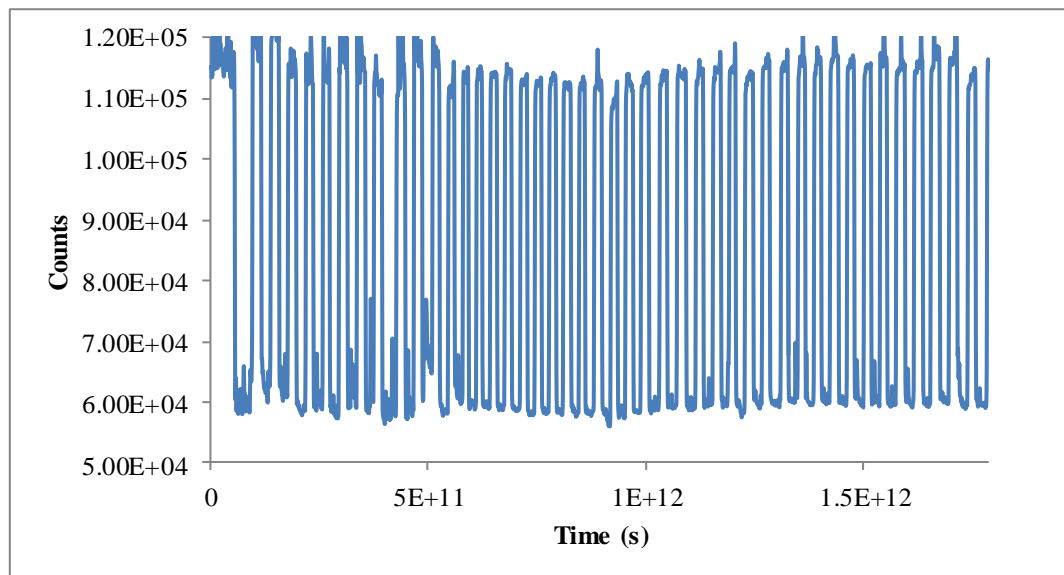


Figure 3.76 Kinetic results of the nanofiber of the CS91 dye in silicon matrix in the presence of VOCs.

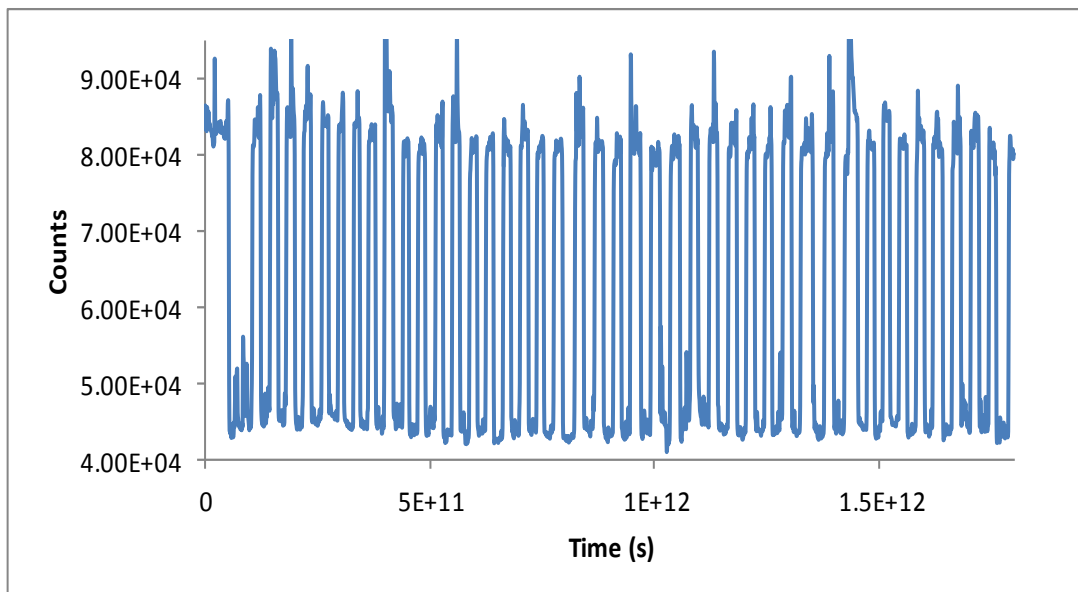


Figure 3.77 Kinetic results of the AgNPs including nanofiber of the CS91 dye in silicon matrix in the presence of VOCs.

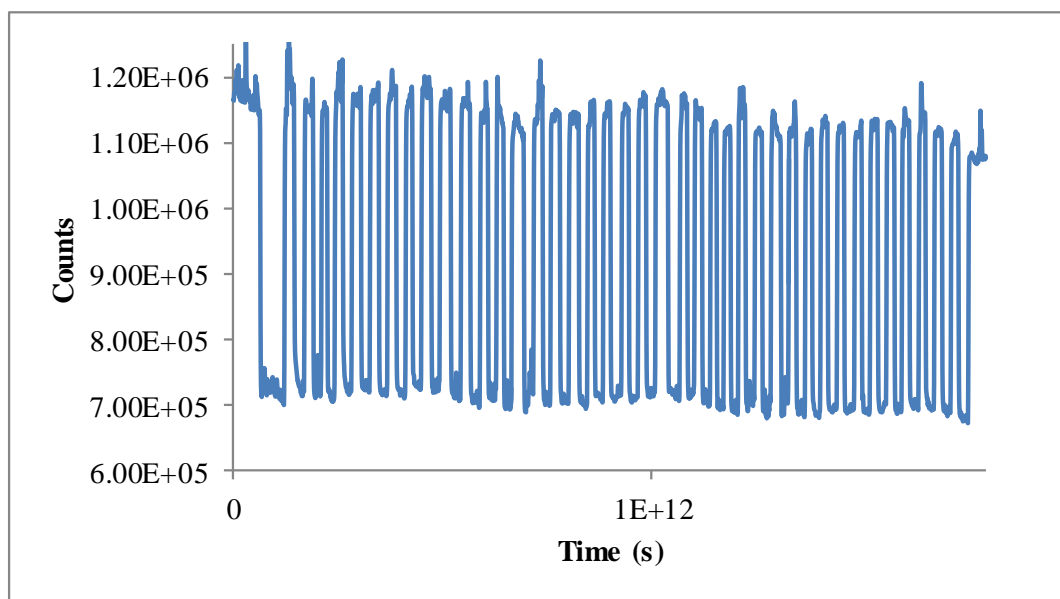


Figure 3.78 Kinetic results of the thin film of the CS93 dye in poly(TMSP) matrix in the presence of VOCs.

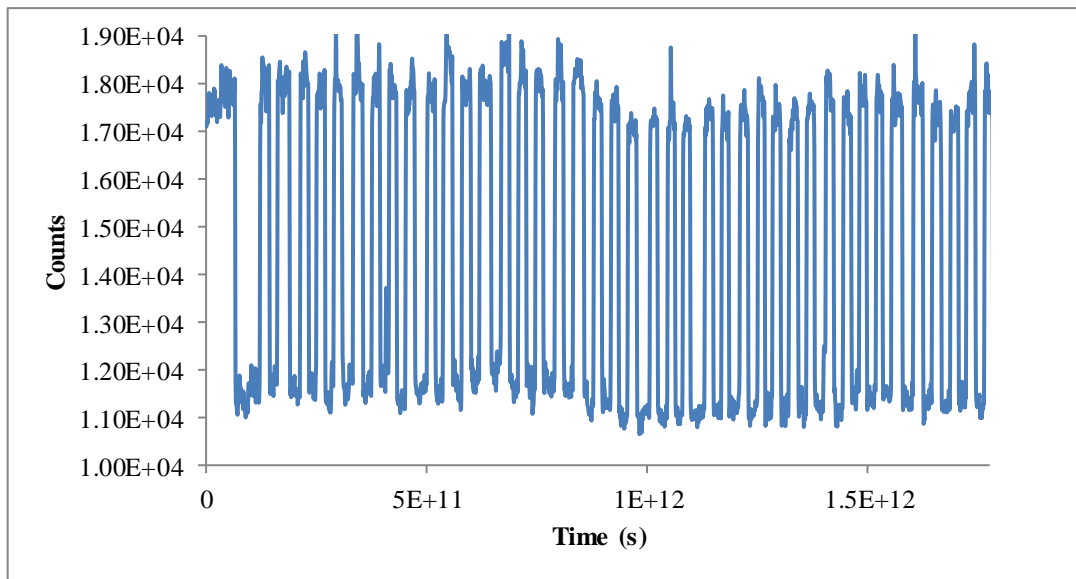


Figure 3.79 Kinetic results of the AgNPs including thin film of the CS93 dye in poly(TMSP) matrix in the presence of VOCs.

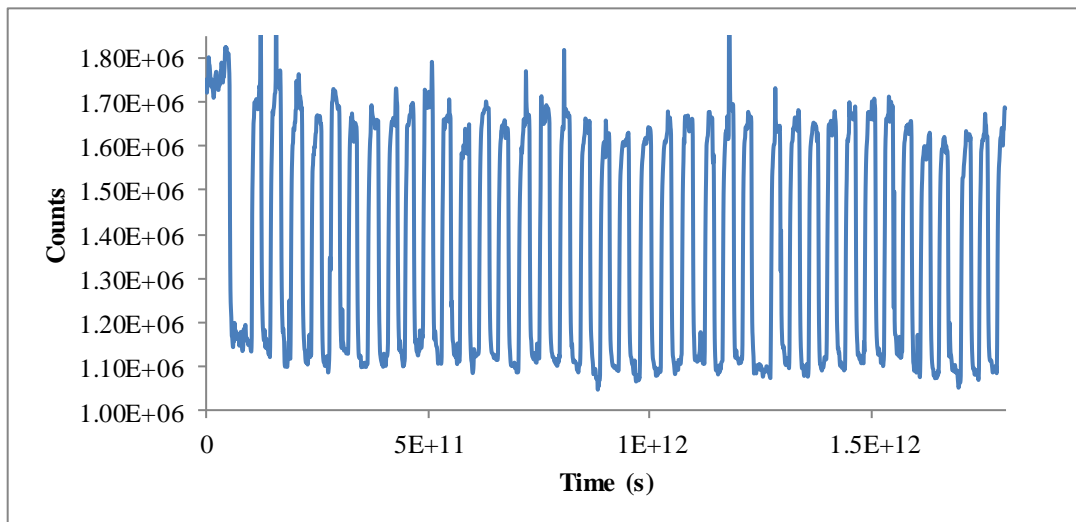


Figure 3.80 Kinetic results of the nanofiber of the CS93 dye in poly(TMSP) matrix in the presence of VOCs.

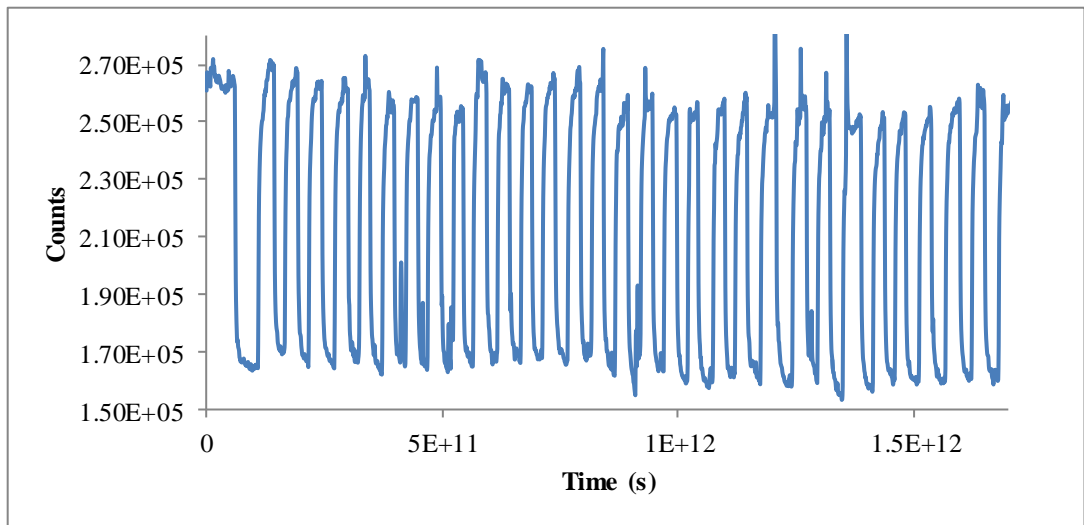


Figure 3.81 Kinetic results of the AgNPs including nanofiber of the CS93 dye in poly(TMSP) matrix in the presence of VOCs.

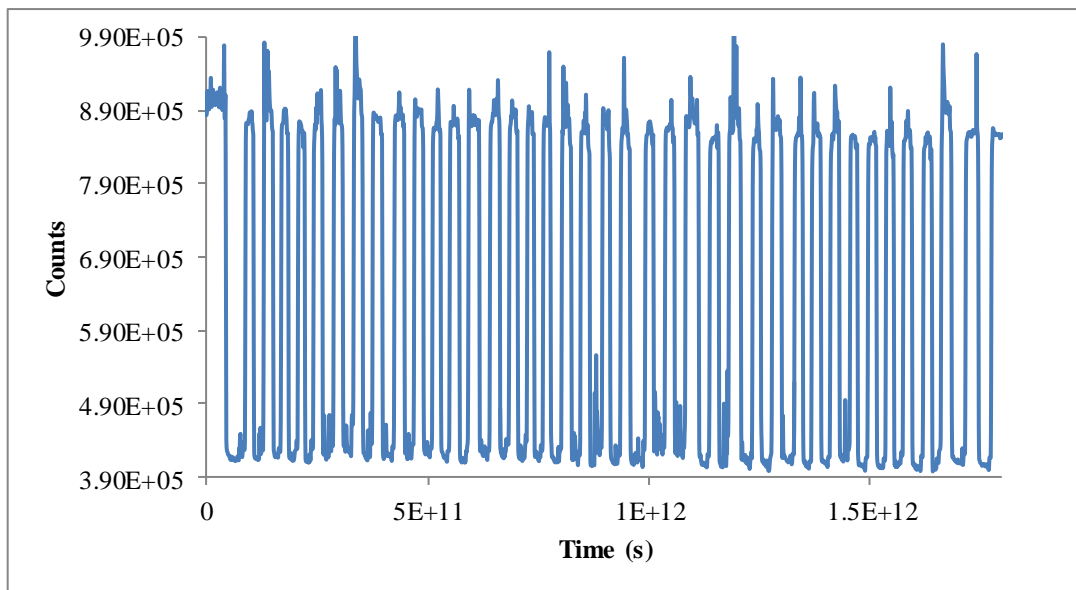


Figure 3.82 Kinetic results of the thin film of the CS93 dye in silicon matrix in the presence of VOCs.

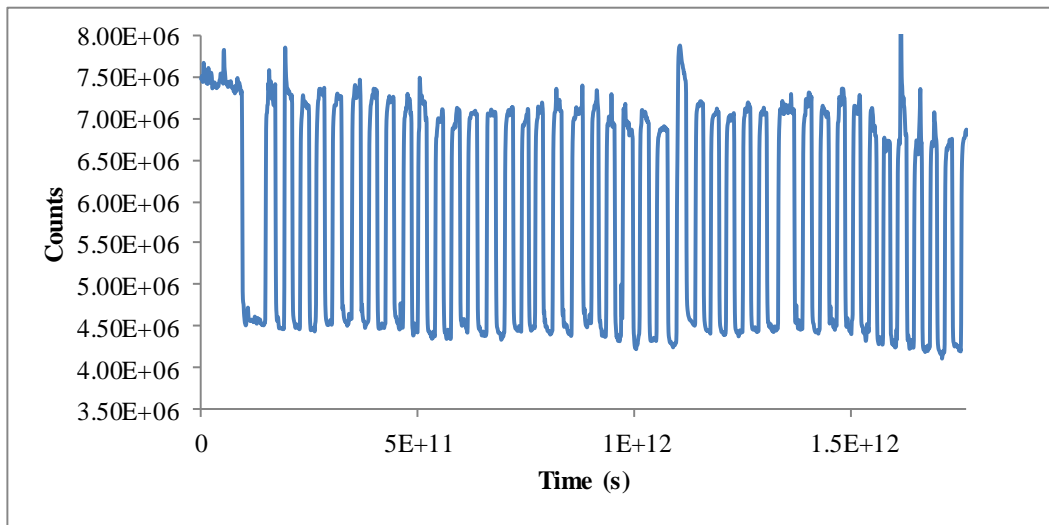


Figure 3.83 Kinetic results of the AgNPs including thin film of the CS93 dye in silicon matrix in the presence of VOCs.

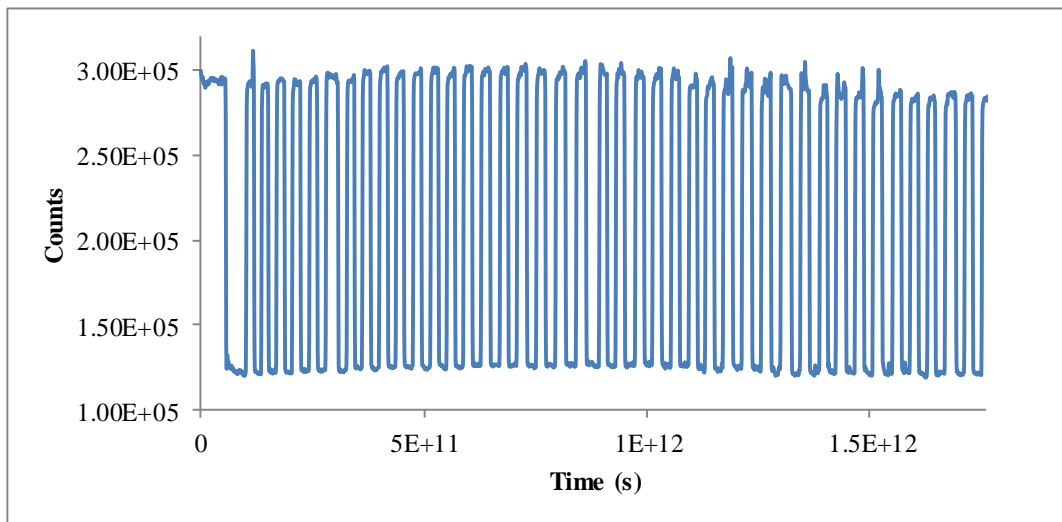


Figure 3.84 Kinetic results of the nanofiber of the CS93 dye in silicon matrix in the presence of VOCs.

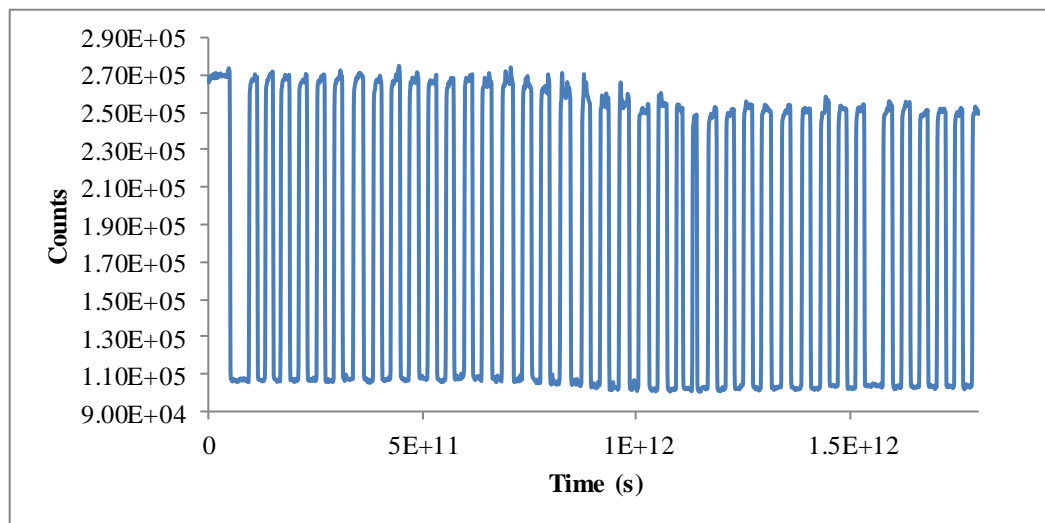


Figure 3.85 Kinetic results of the AgNPs including nanofiber of the CS93 dye in silicon matrix in the presence of VOCs.

Data acquired under contaminated conditions for the composites shown in Figure 3.84 and 3.85 exhibited the best results. Responses of the sensing agents shown in figure 3.72, 3.76, 3.77 and 3.82 were also satisfactory. The poly(TMSP) embedded CS91 dye exhibited large drift when exposed to alternating atmospheres of oxygen and nitrogen under vapors of volatile organics (see Figure 3.70 and 3.71).

3.6 Results for Dissolved Oxygen

In order to test the impact of dissolved oxygen (dO_2) on the sensitivity of fluorescence signal of the CS91 and CS93 in response to the concentration of dissolved oxygen, the flat bottomed flask is immersed in a water bath on a stirrer. The temperature of the water bath was adjusted to 30 °C, 20 °C, 10 °C and finally to 5 °C. At each temperature, the water was saturated with 100% O_2 . dO_2 concentrations of the solutions were calculated as 12.8, 11.3, 9.1 and 7.5 $mg.L^{-1}$, for the given temperatures (see Table 3.7). The fluorescence spectra were recorded changing the solutions having different concentrations of oxygen between 7.5-12.8 ppm. The spectra were recorded for all of the test moieties for CS91 and CS93. Figures 3.86-3.99 show the steady state response of the sensing agents towards dissolved oxygen.

Table 3.7 Studied temperatures of the water bath for dissolved oxygen studies.

Temperature of the water bath(°C)	5	10	20	30
dO₂ concentrations (mg.L⁻¹)	12.8	11.3	9.1	7.5

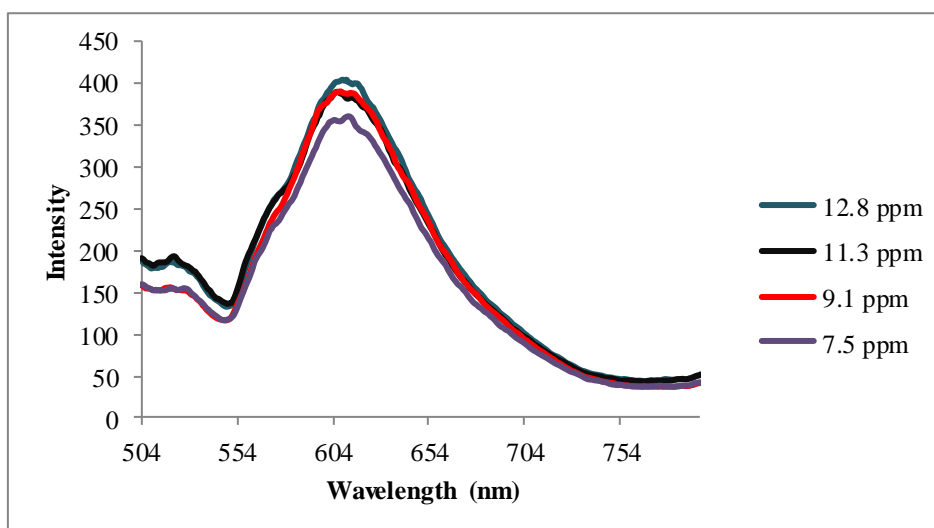


Figure 3.86 Response of CS91 to dissolved oxygen. The dye is embedded in poly(TMSP) and is in thin film form.

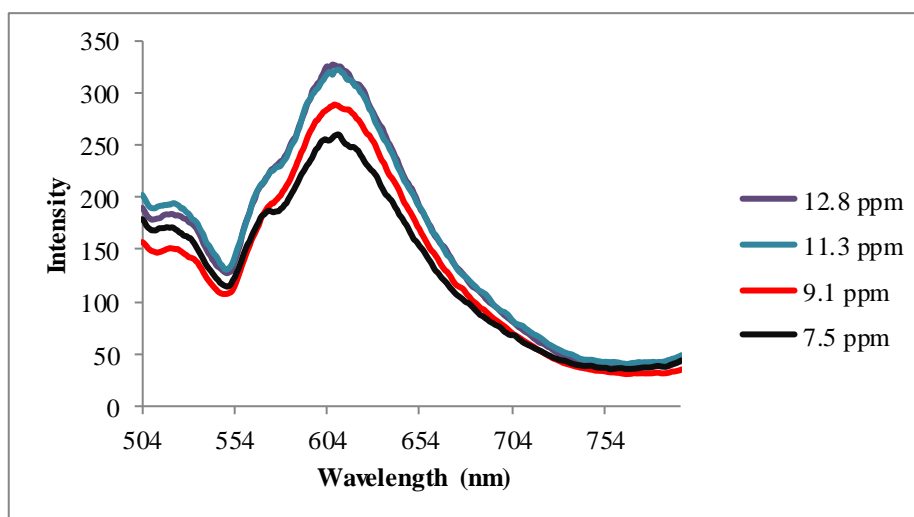


Figure 3.87 Response of CS91 to dissolved oxygen. The dye is embedded in AgNPs including poly(TMSP) and is in thin film form.

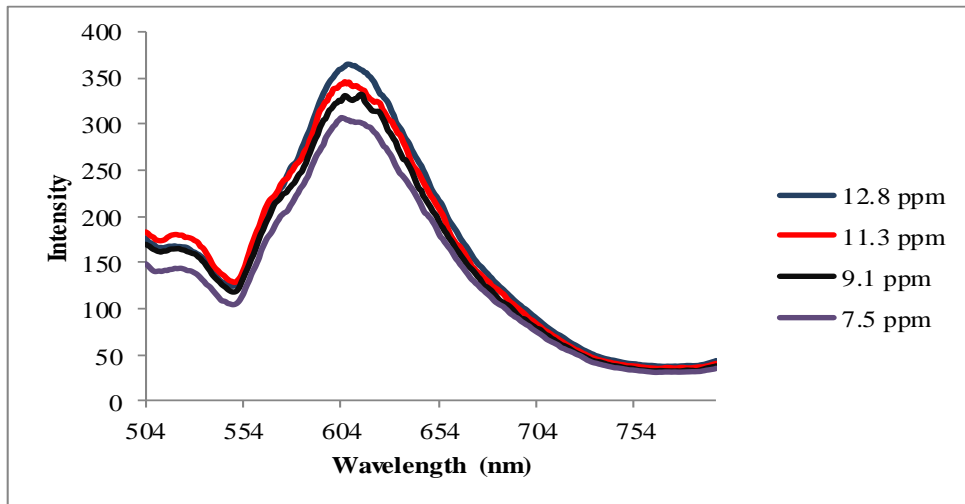


Figure 3.88 Response of CS91 to dissolved oxygen. The dye is embedded in poly(TMSP) and is in nanofiber form.

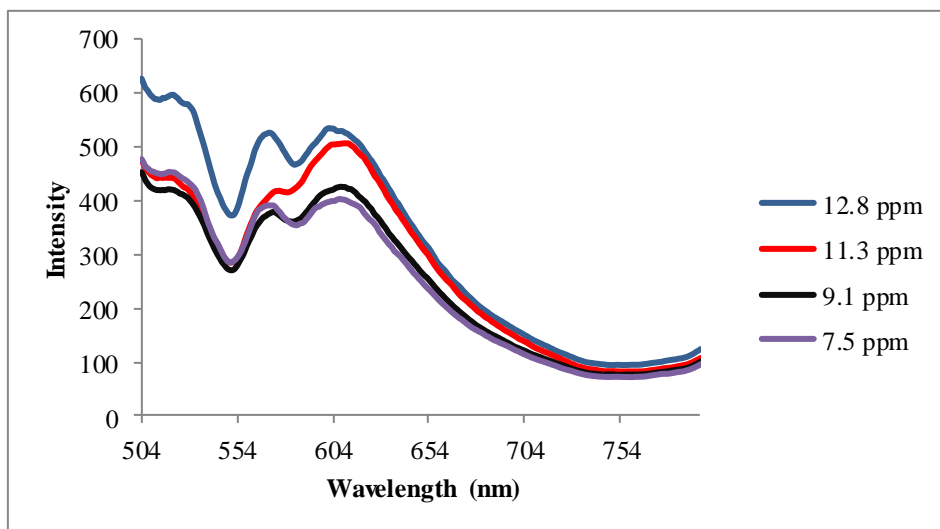


Figure 3.89 Response of CS91 to dissolved oxygen. The dye is embedded in AgNPs including poly(TMSP) and is in nanofiber form.

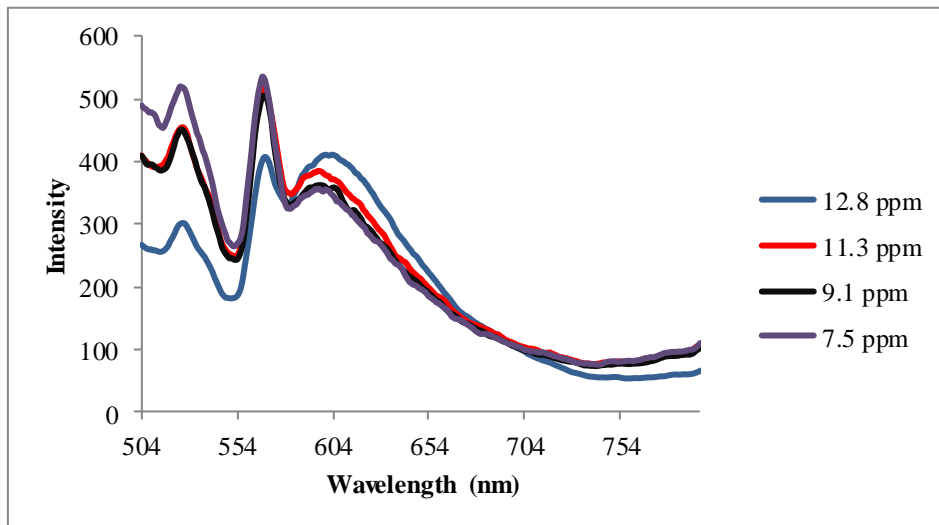


Figure 3.90 Response of CS91 to dissolved oxygen. The dye is embedded in silicon and is in nanofiber form.

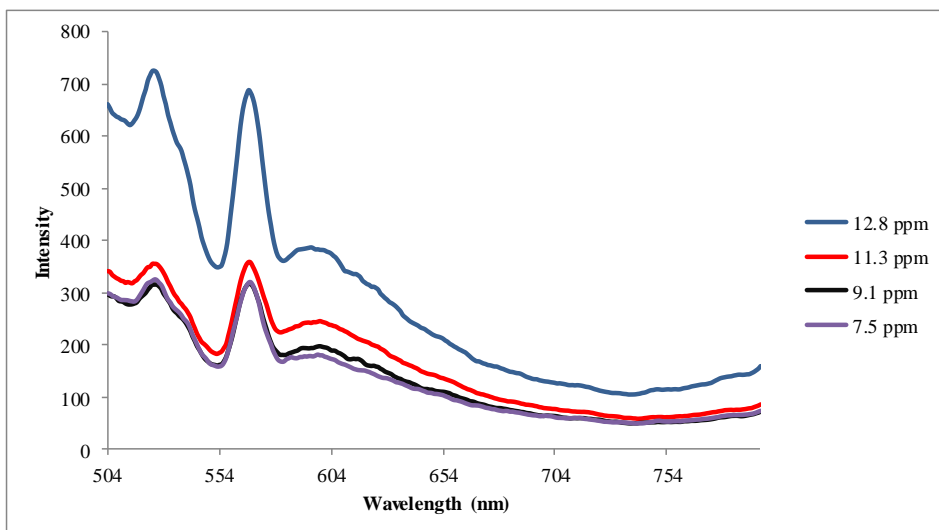


Figure 3.91 Response of CS91 to dissolved oxygen. The dye is embedded in AgNPs including silicon and is in nanofiber form.

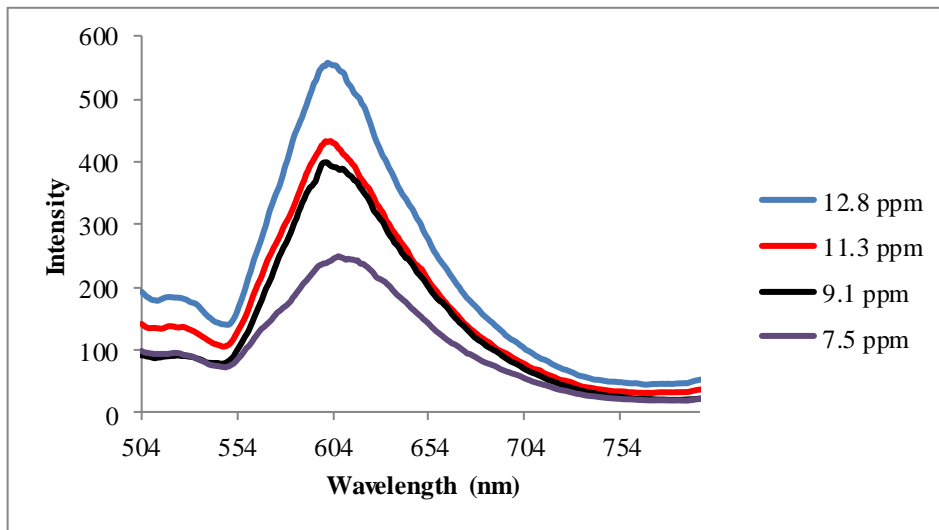


Figure 3.92 Response of CS93 to dissolved oxygen. The dye is embedded in poly(TMSP) and is in thin film form.

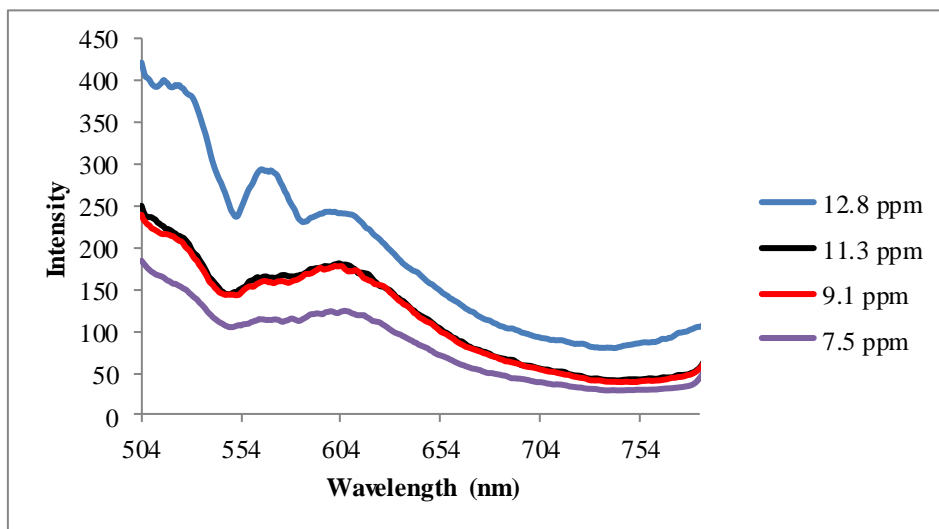


Figure 3.93 Response of CS93 to dissolved oxygen. The dye is embedded in AgNPs including poly(TMSP) and is in thin film form.

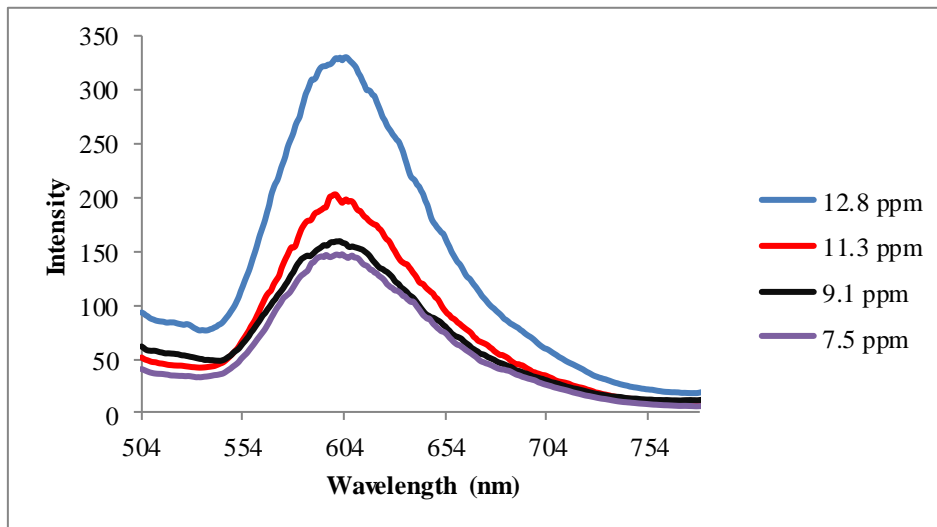


Figure 3.94 Response of CS93 to dissolved oxygen. The dye is embedded in silicon and is in thin film form.

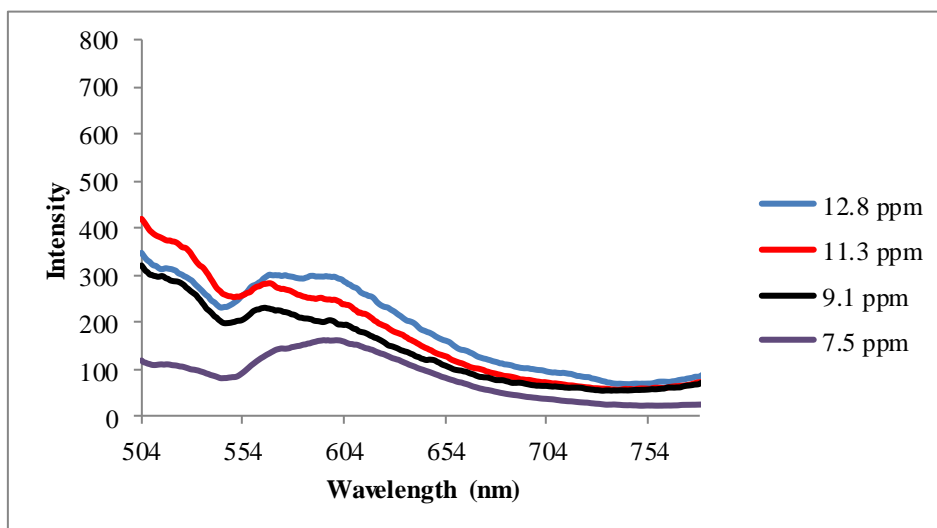


Figure 3.95 Response of CS93 to dissolved oxygen. The dye is embedded in AgNPs including silicon and is in thin film form.

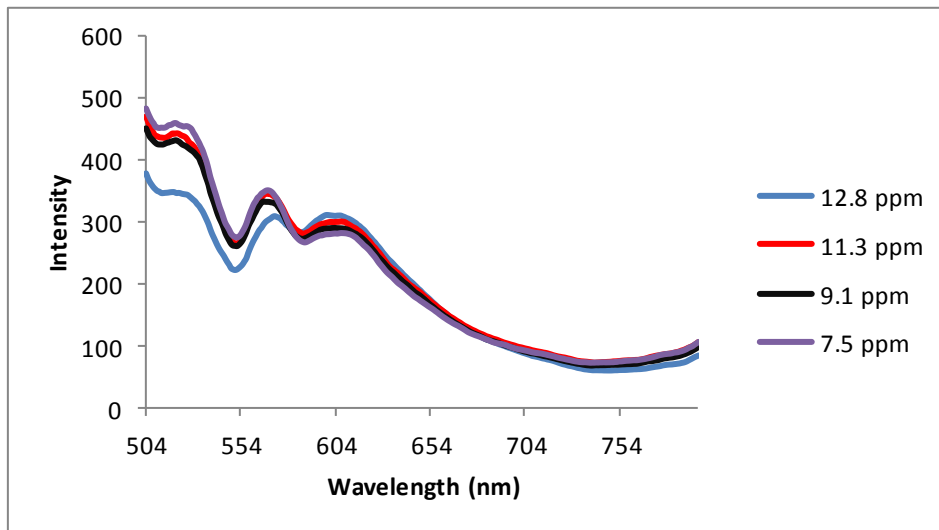


Figure 3.96 Response of CS93 to dissolved oxygen. The dye is embedded in poly(TMSP) and is in thin nanofiber form.

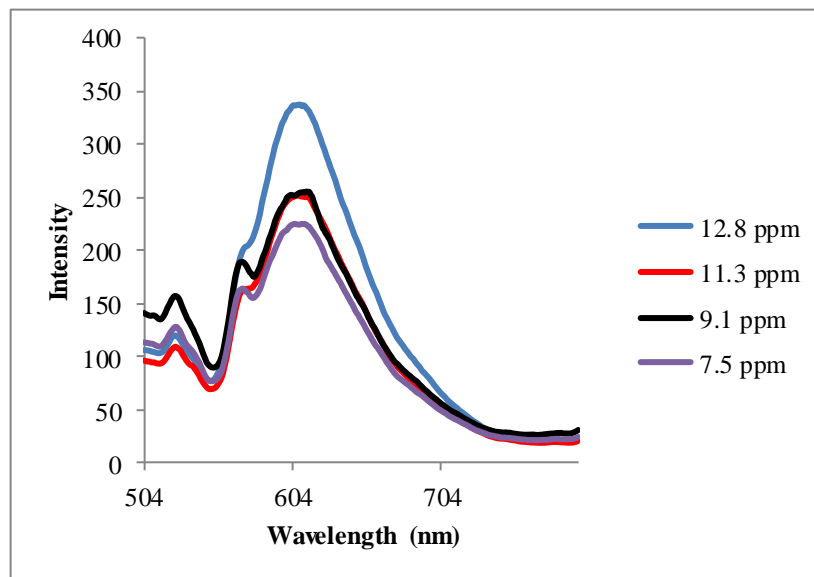


Figure 3.97 Response of CS93 to dissolved oxygen. The dye is embedded in AgNPs including poly(TMSP) and is in thin nanofiber form.

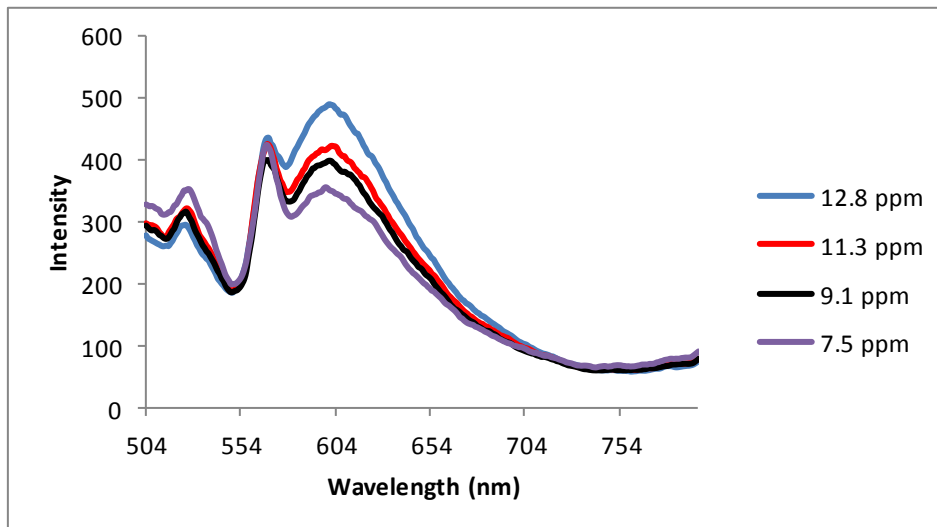


Figure 3.98 Response of CS93 to dissolved oxygen. The dye is embedded in silicon and is in thin nanofiber form.

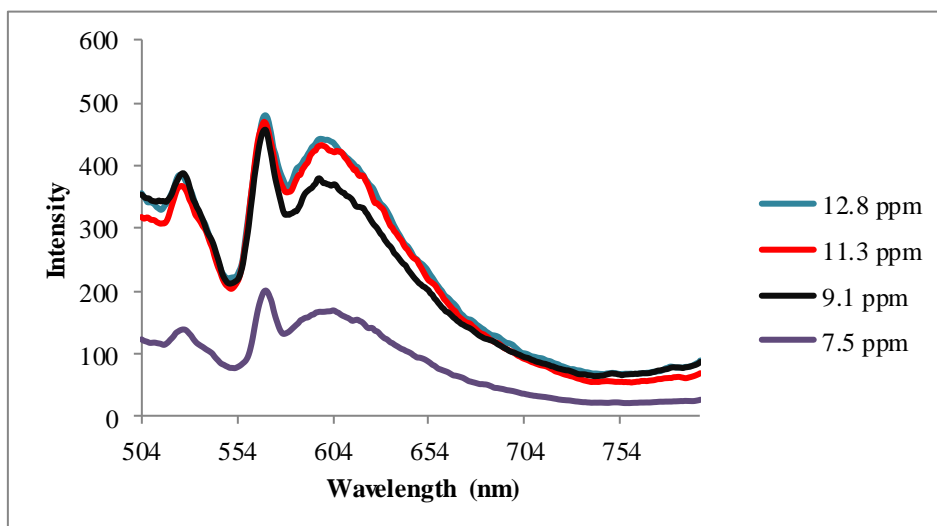


Figure 3.99 Response of CS93 to dissolved oxygen. The dye is embedded in AgNPs including silicon and is in thin nanofiber form.

The related calibration graphs were derived for all of the exploited moieties. In all cases the CS91 and CS93 responded to dO_2 without any leaching after 10 measurements. Figure 3.86- 3.101 reveals representative dO_2 response of the CS91 and CS93 in poly(TMSP) and silicon, respectively. Almost all of the composites exhibited good slopes (see Table 3.8), which is an indicator of high sensitivity, and satisfactory linearity within the measured concentration range. Among them the thin

film form of silver containing CS93 in silicon exhibited the highest sensitivity ($m=9.133$) to the dissolved oxygen (see Figure 3.105).

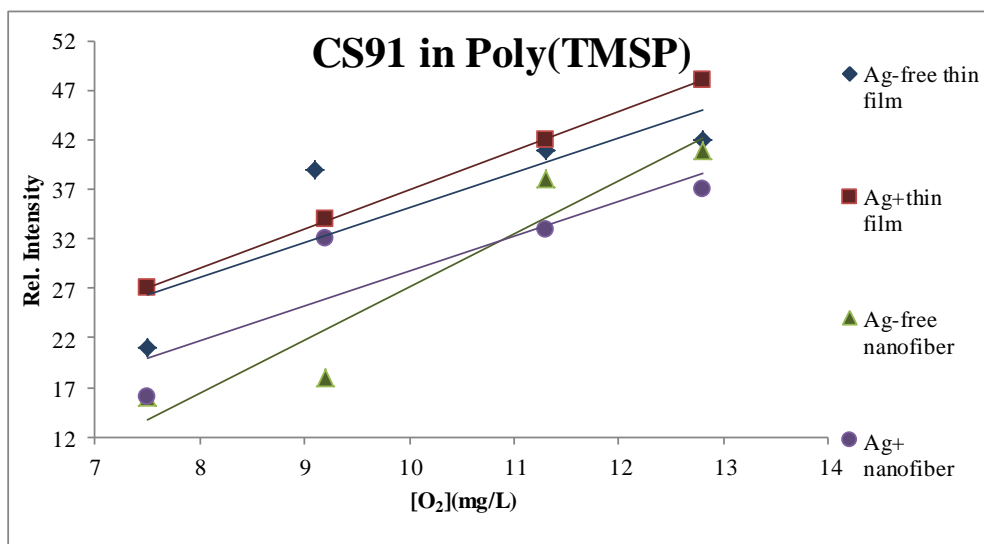


Figure 3.100 Gathered Stern-Volmer plots of nanofibers and thin films of CS91 dye in polyTMSP matrix for oxygen dissolved studies.

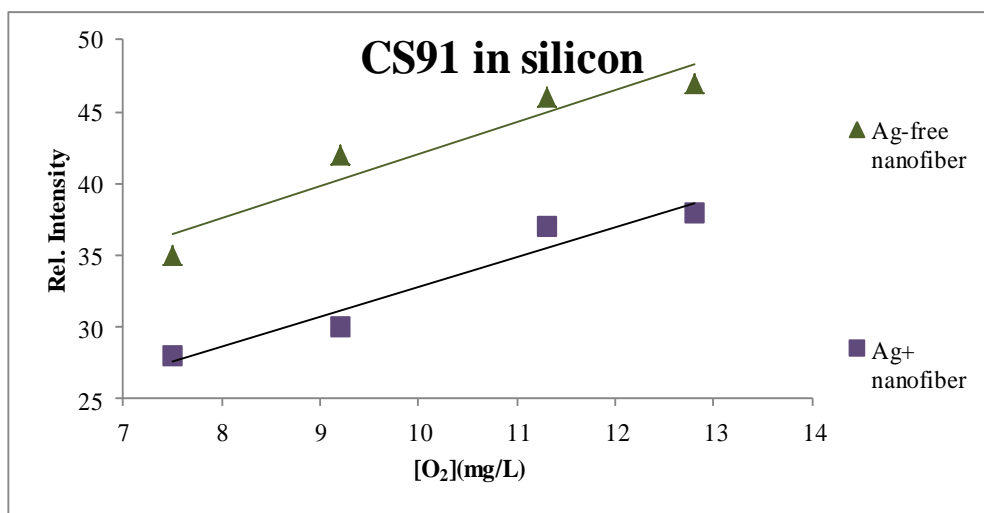


Figure 3.101 Gathered Stern-Volmer plots of nanofibers and thin films of CS91 dye in silicon matrix for oxygen dissolved studies.

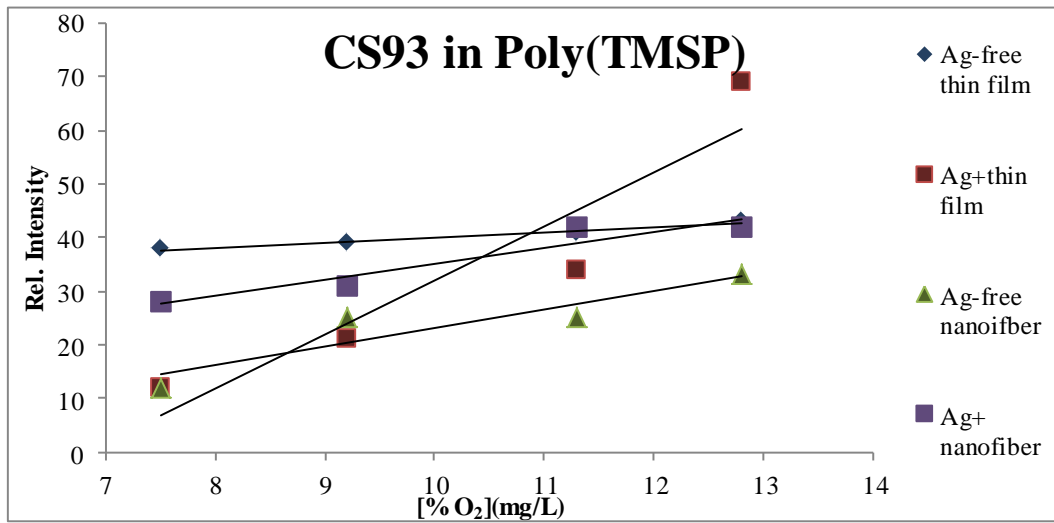


Figure 3.102 Gathered Stern-Volmer plots of nanofibers and thin films of CS93 dye in poly(TMSP) matrix for oxygen dissolved studies.

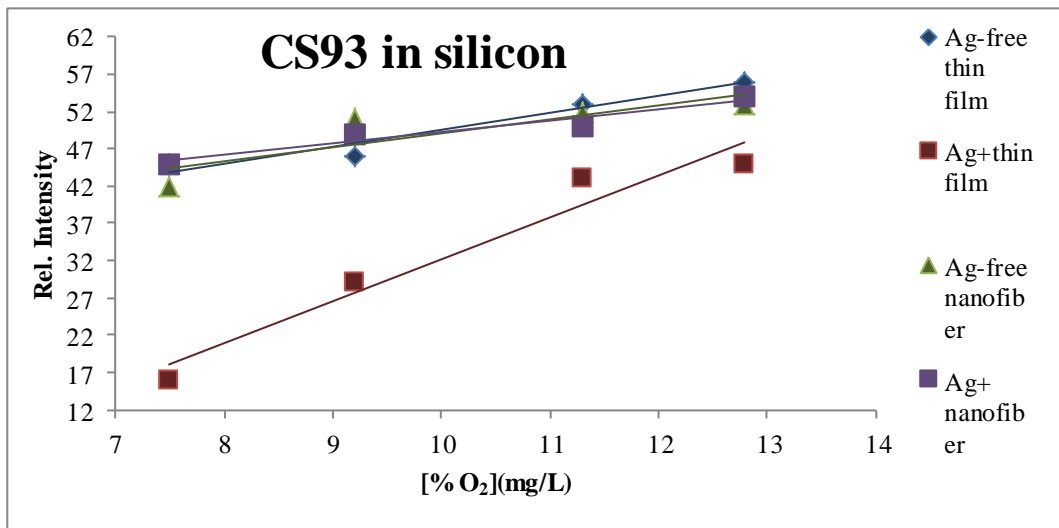


Figure 3.103 Gathered Stern-Volmer plots of nanofibers and thin films of CS93 dye in silicon matrix for oxygen dissolved studies.

Table 3.8 The Stern Volmer plots for dissolved oxygen studies, oxygen induced relative signal changes, related regression coefficients and K_{sv} values extracted from the slopes of the plots.

Dye	Matrix	Thin film/ nanofiber	Nano silver (mg)	Stern-Volmer plots (clean air)	$K_{sv}[\text{O}_2\%]^{-1}$
CS91	poly(TMSP)	TF	-	$y=3.5388x-0.2572$	3.388
CS91	poly(TMSP)	NF	-	$y=5.3629x-26.451$	5.3629
CS91	poly(TMSP)	TF	+	$y=3.9422x-2.4603$	3.422
CS91	poly(TMSP)	NF	+	$y=3.524x-6.446$	3.524
CS93	poly(TMSP)	TF	-	$y=3.0012x+5.1375$	3.0012
CS93	poly(TMSP)	NF	-	$y=3.4379x-68.502$	3.4379
CS93	poly(TMSP)	TF	+	$y=10.049x-68.502$	10.049
CS93	poly(TMSP)	NF	+	$y=0.941x+30.652$	0.941
CS91	silicon	NF	-	$y=2.2352x+19.729$	2.2352
CS91	silicon	NF	+	$y=2.0849x+11.984$	2.0849
CS93	silicon	TF	-	$y=2.2386x+27.166$	2.2386
CS93	silicon	NF	-	$y=1.8819x+30.304$	1.8819
CS93	silicon	TF	+	$y=5.6642x-24.525$	5.6642
CS93	silicon	NF	+	$y=1.5214x+33.88$	1.5214

3.7 Selectivity Studies and Interference Effects

In order to examine the cross sensitivities of the CS91 and CS93 dye to other cations, the sensing agents were treated with 10^{-5} M concentrations of Ag^+ , Al^{3+} , Ba^{2+} , Ca^{2+} , Co^{2+} , Cr^{2+} , Cu^{2+} , Fe^{2+} , Fe^{3+} , Hg^+ , Hg^{2+} , K^+ , Mg^{2+} , Mn^{2+} , Na^{2+} , Ni^{2+} , Pb^{2+} , Sn^{2+} and Zn^{2+} cations in acetic acid/acetate buffer solutions at pH 4.0. Figure 3.106 and 3.107 reveal that both the CS91 and CS93 dyes exhibit cross sensitivity to Hg (II) ions. Also CS91 has sensitivity to Fe (III) ion. However, the cross sensitivities of the dyes to the major cations of water like Ca^{2+} , K^+ , Mg^{2+} , and Na^{2+} are considerably less than that of the sensitivity towards dissolved oxygen.

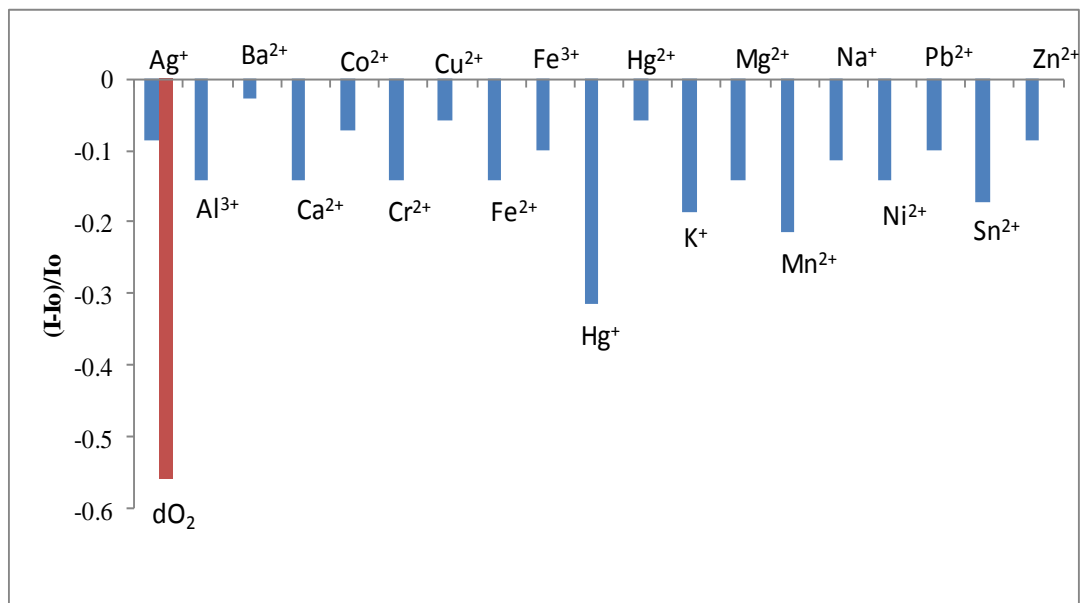


Figure 3.104 Response of CS93 dye in THF to 10^{-5} M of different metal cations in acetic acid/acetate buffer solutions at pH 4.0.

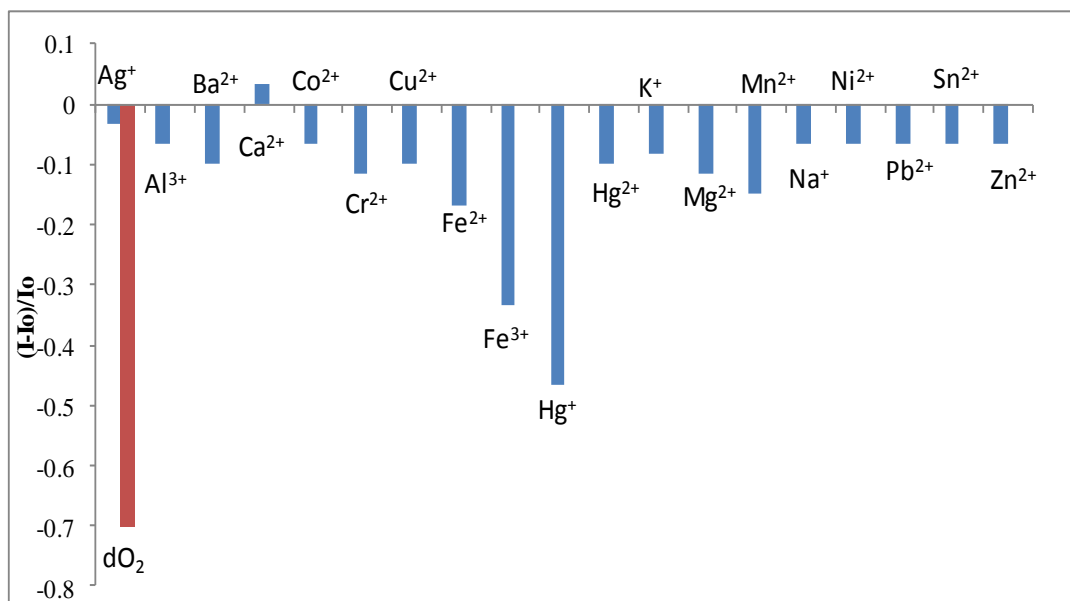


Figure 3.105 Response of CS91 dye in THF to 10^{-5} M of different metal cations in acetic acid/acetate buffer solutions at pH 4.0.

CHAPTER FOUR

CONCLUSION

In workplaces, especially in refineries, volatile petroleum solvents are usually in form of mixtures of VOCs; alkanes, cyclic alkanes, alkenes (olefins) and the aromatics. In such atmospheres correct and continuous monitoring of oxygen levels is quite important. On the other hand, ruthenium dyes have been extensively used in the detection of oxygen. However, most of the water soluble ruthenium dyes may not be compatible with polymeric matrices in terms of encapsulation and may suffer from leaching in aqueous media. They mainly employed for gas sensing purposes. While chemically bonding the dye to the matrix can eliminate leaching, the sensing ability of the dye may diminish.

The silicon based matrices are probably the most extensively used matrices in the design of oxygen sensors due to the excellent diffusibility and spectral transparency. In order to provide the best host/dye compatibility we used the amphiphilic ruthenium derivatives CS 91 and 93 in silicon based matrices for the first time. Therefore, in the offered designs the poly(TMSP) and silicon doped ruthenium derivatives (CS91 and CS93) along with AgNPs have been efficiently used in measurement of both gaseous and dissolved oxygen. The CS91 and CS93 exhibited the highest signals in silicon matrix, in the presence of AgNPs, and when they were in form of nanofibers. The alkyl branched dyes were not subject to leaching even under flow systems, organic volatiles and harsh conditions. Both of the exploited dyes exhibited similar emission based spectral response to oxygen. The exploited dyes were highly stable, can be excited with a blue LED and show excellent compatibility with other solid state optics like cheap optical fibers due to the high Stoke's Shift values extending to 180 nm.

Most of the oxygen sensing studies suffer from nonlinear calibration plots within the measured oxygen concentrations, instabilities of the signal intensities, or from leaching in wet moieties (Roche, et al., 2010; Wu, Song, Li, & Liu, 2010; Zhang, Lei, Mai, & Liua, 2011). The CS91 and CS93 exhibited good Stern Volmer constants

and more linear calibration graphics with respect to other studies (see Table 3.1). The higher Stern-Volmer constants can be concluded as the higher sensitivity to the oxygen.

Sensing characteristics of the offered design have been tested and calibrated in the presence of vapors of benzene, toluene, ethylbenzene, hexane and xylene, which simulate refinery related work places. The studied concentrations of VOCs were much higher than the exposure limits that are given by OSHA and ACGIH (see the Table 1.1). The responses of the dyes to oxygen did not change dramatically with respect to the signals attained under clean air. Therefore the oxygen sensing composites can be used even under high concentrations of VOCs to measure the oxygen concentrations accurately. The exploited dyes of CS91 and CS93 in embedded form can also be utilized to detect dissolved oxygen in the concentration range between 7.5-12.8 ppm. The cross sensitivity of the dyes towards major cations of water is negligible. The offered composite can be employed for both, gas phase and dissolved O₂ measurements even in refinery conditions for the accurate measurement of oxygen.

REFERENCES

- Borisov, S. M., Mayr, T., Mistlberger, G., Waich, K., Koren, K., Chojnacki, P., et al. (2009). Precipitation as a simple and versatile method for preparation of optical nanochemosensors. *Talanta*, 79 (5), 1322-1330.
- Cattrall, R. W. (1997). *Chemical sensors*. New York: Oxford University Press Inc.
- Chatni, M. R., Maier, D. E., & Porterfield, D. M. (2009). Evaluation of microparticle materials for enhancing the performance of fluorescence lifetime based optrodes. *Sensors and Actuators B: Chemical*, 141 (2), 471-477.
- Chu, C. S., & Chuang, C. Y. (2015). Optical fiber sensor for dual sensing of dissolved oxygen and Cu²⁺ ions based on PdTFPP/CdSe embedded in sol-gel matrix. *Sensors and Actuators B: Chemical*, 209, 94-99.
- Chu, C. S., & Lo, Y. L. (2010). Optical fiber dissolved oxygen sensor based on Pt (II) complex and core-shell silica nanoparticles incorporated with sol-gel matrix. *Sensors and Actuators B: Chemical*, 151 (1), 83-89.
- Cohen, S.D., Digby, S.A., & Miller, J. A. (1997). *Understanding fiber optic cables and connectors*. Retrieved October 15, 2012, from <http://archives.sensorsmag.com/articles/0898/un0898/>.
- Cywinski, P. J., Moro, A. J., Stanca, S. E., Biskup, C., & Mohr, G. J. (2009). Ratiometric porphyrin-based layers and nanoparticles for measuring oxygen in biosamples. *Sensors and Actuators B: Chemical*, 135 (2), 472-477.
- Elosua, C., de Acha, N., Hernaez, M., Matias, I. R., & Arregui, F. J. (2015). Layer-by-Layer assembly of a water-insoluble platinum complex for optical fiber oxygen sensors. *Sensors and Actuators B: Chemical*, 207, 683-689.
- Estella, J., Wencel, D., Moore, J. P., Sourdain, M., & McDonagh, C. (2010). Fabrication and performance evaluation of highly sensitive hybrid sol-gel-derived oxygen sensor films based on a fluorinated precursor. *Analytica Chimica Acta*, 666 (1), 83-90.

- Fercher, A., Borisov, S. M., Zhdanov, A. V., Klimant, I., & Papkovsky, D. B. (2011). Intracellular O₂ sensing probe based on cell-penetrating phosphorescent nanoparticles. *Acs Nano*, 5 (7), 5499-5508.
- Fluorescence fundamentals*, (2015). Retrieved June 5, 2015, from <https://www.lifetechnologies.com/tr/en/home/references/molecular-probes-the-handbook/introduction-to-fluorescence-techniques.html#head1>
- FLS920 Series*. (2011). Retrieved July, 18, 2014, from Edinburgh Photonics: Web Sites: <http://www.edinburghphotonics.com/files/file/brochures/FLS920-Brochure.pdf>
- Fujiwara, Y., & Amao, Y. (2003). Optical oxygen sensor based on controlling the excimer formation of pyrene-1-butylic acid chemisorption layer onto nano-porous anodic oxidized aluminium plate by myristic acid. *Sensors and Actuators B: Chemical*, 89 (1), 58-61.
- Gulino, A., Bazzano, S., Condorelli, G. G., Giuffrida, S., Mineo, P., Satriano, C., et al. (2005). Engineered Silica Surfaces with an Assembled C₆₀ Fullerene Monolayer. *Chemistry of materials*, 17 (5), 1079-1084.
- Gulino, A., Giuffrida, S., Mineo, P., Purrazzo, M., Scamporrino, E., Ventimiglia, et al. (2006). Photoluminescence of a covalent assembled porphyrin-based monolayer: optical behavior in the presence of O₂. *The Journal of Physical Chemistry B*, 110 (33), 16781-16786.
- Hirao, T., & Fukuhara, S. (1998). An organic catalytic system for dehydrogenative oxidation. *The Journal of Organic Chemistry*, 63 (21), 7534-7535.
- Hulanicki, A., Glab, S., & Ingman, F. (1991). Chemical sensors: definitions and classification. *Pure and Applied Chemistry*, 63 (9), 1247-1250.
- Ishiji, T., & Kaneko, M. (1995). Photoluminescence of pyrenebutyric acid incorporated into silicone film as a technique in luminescent oxygen sensing. *Analyst*, 120 (6), 1633-1638.

- Jorge, P. A. S., Maule, C., Silva, A. J., Benrashid, R., Santos, J. L., & Farahi, F. (2008). Dual sensing of oxygen and temperature using quantum dots and a ruthenium complex. *Analytica Chimica Acta*, 606 (2), 223-229.
- Kalabokas, P. D., Hatzianestis, J., Bartzis, J. G., & Papagiannakopoulos, P. (2001). Atmospheric concentrations of saturated and aromatic hydrocarbons around a Greek oil refinery. *Atmospheric Environment*, 35 (14), 2545-2555.
- Lakowicz, J. R. (1993). *Principles of fluorescence spectroscopy*. Plenum Press: New York and London.
- Modulated LED source for film microscopy*, (n.d.). Retrieved June 10, 2015, from https://www.thorlabs.com/NewGroupPage9_PF.cfm?Guide=10&Category_ID=220&ObjectGroup_ID=3459
- Oner, I., Sahin, C., & Varlikli, C. (2012). Electroluminescence from two new ruthenium (II) complexes as phosphorescent dopant: Positive effect of swallow-tail bipyridyl ligand. *Dyes and Pigments*, 95 (1), 23-32.
- Ozturk, O., Oter, O., Yildirim, S., Subasi, E., Ertekin, K., Celik, E., et al. (2014). Tuning oxygen sensitivity of ruthenium complex exploiting silver nanoparticles. *Journal of Luminescence*, 155, 191-197.
- Parker, C. (1968). *Photoluminescence of solutions (1st ed.)*. Amsterdam: Elsevier.
- Schmidt, W. (1994). *Optische Spektroskopie*. VCH: Weinheim.
- Petrochemical VOCs analysis*, (2015). Retrieved April 16, 2015, from <http://www.sigmaaldrich.com/analytical-chromatography/air-monitoring/applications/petrochemical/volatile-organic-compounds.html>
- Roche, P. J., Cheung, M. C. K., Yung, K. Y., Kirk, A. G., Chodavarpu, V. P., & Bright, F. V. (2010). Application of gold quenching of luminescence to improve oxygen sensing using a ruthenium (4, 7-diphenyl-1, 10-phenanthroline)₃ Cl₂: TEOS thin film. *Sensors and Actuators B: Chemical*, 147 (2), 581-586.

- Sacksteder, L., Demas, J. N., & DeGraff, B. A. (1993). Design of oxygen sensors based on quenching of luminescent metal complexes: effect of ligand size on heterogeneity. *Analytical Chemistry*, 65 (23), 3480-3483.
- Singh, R. K., Ramteke, D. S., Juneja, H. D., & Pandya, G. H. (2013). Ambient air quality monitoring in terms of volatile organic compounds (VOCs) occupational health exposure at petroleum refinery. *International Journal of Environmental Protection*, 3 (7), 22.
- Solomon, S. D., Bahadory, M., Jeyarajasingam, A. V., Rutkowsky, S. A., & Boritz, C. (2007). Synthesis and study of silver nanoparticles. *Journal of Chemical Education*, 84 (2), 322.
- Stokes shift*, (2015). Retrieved June 05, 2015, from http://en.wikipedia.org/wiki/Stokes_shift
- Terpetschnig, E., & Jameson, D. M. (n.d.). Retrieved June 10, 2015, from http://www.iss.com/resources/research/technical_notes/K2CH_FLT.html
- Time resolved fluorescence lifetime measurements*. (2014). Retrieved July, 18, 2014, from Horiba Scientific: http://www.horiba.com/fileadmin/uploads/Scientific/Documents/Fluorescence/Tech_Note1_-_Lifetime_measurements.pdf
- Toro, M. M. S., Fernandez-Sanchez, J. F., Baranoff, E., Nazeeruddin, M. K., Graetzel, M., & Fernandez-Gutierrez, A. (2010). Novel luminescent Ir (III) dyes for developing highly sensitive oxygen sensing films. *Talanta*, 82 (2), 620-626.
- University of Wisconsin - Safety Department*, (n.d.). Retrieved June 08, 2015, from <http://www.ehs.wisc.edu/chem/OccupationalExposureLimits.pdf>
- Valeur, B., & Berberan-Santos, M. N. (2012). *Molecular fluorescence: Principles and applications*. John Wiley & Sons.
- Valeur, B., & Leray, I. (2000, August Tuesday). Design principles of fluorescent molecular sensors for cation recognition. *Coordination Chemistry Reviews*, 205 (1), 3-40.

- Wang, X. D., & Wolfbeis, O. S. (2012). Fiber-optic chemical sensors and biosensors (2008–2012). *Analytical Chemistry*, 85 (2), 487-508.
- Wang, B., Liu, Y., Li, B., Yue, S., & Li, W. (2008). Optical oxygen sensing materials based on trinuclear starburst ruthenium (II) complexes assembled in mesoporous silica. *Journal of Luminescence*, 128 (3), 341-347.
- Wang, X. H., Peng, H. S., Ding, H., You, F. T., Huang, S. H., Teng, F., et al. (2012). Biocompatible fluorescent core-shell nanoparticles for ratiometric oxygen sensing. *Journal of Materials Chemistry*, 22 (31), 16066-16071.
- Wang, X. H., Peng, H. S., Chang, Z., Hou, L. L., You, F. T., Teng, F., et al. (2012). Synthesis of ratiometric fluorescent nanoparticles for sensing oxygen. *Microchimica Acta*, 178 (1-2), 147-152.
- Williams, A.T.R., Winfield, S.A., & Miller, J.N. (1983). Relative fluorescence quantum yields using a computer-controlled luminescence spectrometer. *Analyst*, 108, 1067–1071. Retrieved December 08, 2012, from Web of Science database.
- Wolfbeis, O. S. (Ed.). (1991). *Fiber optic chemical Sensors* (Vol. 1 and 2). Boca Raton, Fla: CRC Press.
- Wu, W., Wu, W., Ji, S., Guo, H., Song, P., Han, K., et al. (2010). Tuning the emission properties of cyclometalated platinum (II) complexes by intramolecular electron-sink/arylethynylated ligands and its application for enhanced luminescent oxygen sensing. *Journal of Materials Chemistry*, 20 (43), 9775-9786.
- Wu, X., Song, L., Li, B., & Liu, Y. (2010). Synthesis, characterization, and oxygen sensing properties of Ru (II) complex covalently grafted to mesoporous MCM-41. *Journal of Luminescence*, 130 (3), 374-379.
- Xu, W., Kneas, K. A., Demas, J. N., & DeGraff, B. A. (1996). Oxygen sensors based on luminescence quenching of metal complexes: osmium complexes suitable for laser diode excitation. *Analytical Chemistry*, 68 (15), 2605-2609.

Zhang, H., Lei, B., Mai, W., & Liu, Y. (2011). Oxygen-sensing materials based on ruthenium (II) complex covalently assembled mesoporous MSU-3 silica. *Sensors and Actuators B: Chemical*, 160 (1), 677-683.

Zhang, H., Li, B., Lei, B., & Li, W. (2008). Oxygen-sensing materials based on $[\text{Ru}(\text{bpy})_3]^{2+}$ covalently grafted MSU-3 mesoporous molecular sieves. *Journal of Luminescence*, 128 (8), 1331-1338.